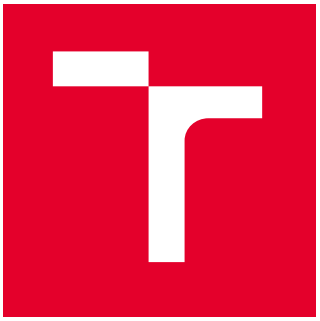

BRNO UNIVERSITY OF TECHNOLOGY

VYSOKÉ UČENÍ TECHNICKÉ V BRNĚ

FACULTY OF MECHANICAL ENGINEERING

FAKULTA STROJNÍHO INŽENÝRSTVÍ

INSTITUTE OF MANUFACTURING TECHNOLOGY

ÚSTAV STROJÍRENSKÉ TECHNOLOGIE

EFFECT OF STRAIN RATE ON THE MECHANICAL PROPERTIES OF MATERIALS

VLIV RYCHLOSTI DEFORMACE NA MECHANICKÉ VLASTNOSTI MATERIÁLŮ

MASTER'S THESIS

DIPLOMOVÁ PRÁCE

AUTHOR — **Bc. Matej Gajdošík**

AUTOR PRÁCE

SUPERVISOR — **Ing. Miroslav Jopek, Ph.D.**

VEDOUCÍ PRÁCE

BRNO 2024

BRNO UNIVERSITY OF TECHNOLOGY
FACULTY OF MECHANICAL ENGINEERING

Assignment Master's Thesis

Institut:	Institute of Manufacturing Technology
Student:	**Bc. Matej Gajdošík**
Degree programm:	Manufacturing Technology
Branch:	Manufacturing Technology
Supervisor:	**Ing. Miroslav Jopek, Ph.D.**
Academic year:	2023/24

As provided for by the Act No. 111/98 Coll. on higher education institutions and the BUT Study and Examination Regulations, the director of the Institute hereby assigns the following topic of Master's Thesis:

Effect of strain rate on the mechanical properties of materials

Brief Description:

Testing of the selected material type at high strain rates on the developed testing apparatus for a symmetric TAT impact test.

Master's Thesis goals:

The work will involve an analysis of the current state and evaluation of issues related to material testing at high strain rates. The objective is to develop a testing apparatus for a symmetric TAT impact test. Based on numerical simulation of aerodynamics, ballistic conditions, and contact conditions in the barrel of the testing apparatus, a device will be designed to ensure the centric impact of two test samples in the impact chamber. The newly developed apparatus will be designed, practically tested, and followed by the evaluation of the experiment for a specific type of material.

Recommended bibliography:

MEYERS, Marc André. Dynamic Behavior of Materials. Marc. A. Mayers. 1 edice. New York : John Wiley & Sons, Inc., 1994. 668 s. A Wiley Interscience Publication. ISBN 0-471-58262-X.

GILLIS, Peter a GROSS, Ted. Effect of Strain Rate on Flow Properties. Metals handbook, 9 edition, volume 8 – Mechanical Testing. American Society for Metals, Ohio, 1985.

NOWACKI, Wojciech a KLEPACZKO Janusz. New Experimental Methods in Material Dynamics and Impact. In Trends in Mechanics of Materials. volume 3, 2003.

JOPEK, Miroslav. Modelování mechanického chování ocelí za vyšších rychlostí deformace, PhD thesis, Vysoké učení technické v Brně, Fakulta strojního inženýrství, Brno, 2003. ISBN 80-214-2437-0.

KUNČICKÁ, Lenka; JOPEK, Miroslav; KOCICH, Radim a DVOŘÁK, Karel. Determining Johnson-Cook Constitutive Equation for Low-Carbon Steel via Taylor Anvil Test. Materials, 2021, vol. 14, no. 17, s. 1-15. ISSN 1996-1944.

Deadline for submission Master's Thesis is given by the Schedule of the Academic year 2023/24

In Brno,

L. S.

Ing. Jan Zouhar, Ph.D. Director of the Institute	doc. Ing. Jiří Hlinka, Ph.D. FME dean

ABSTRACT

Taylor Anvil Test method is used for the investigation of material properties under dynamic loading conditions. The thesis presents a complete process of development, assembly, and testing of a new testing apparatus aimed at achieving a symmetric impact of two material samples in motion. The device is tested in two configurations, results of both are described. Material tests of spruce wood were conducted and compared to results obtained from the classic Taylor canon. Substantial differences are observed and described. Conducted simulations of symmetric impact utilizing the spruce material model have not proven to represent practical experiments, hinting at required changes to the model.

Keywords

Taylor Anvil Test, symmetric, test apparatus, spruce, wood

ABSTRAKT

Metóda Taylorovho testu je využívaná na skúmanie vlastností materiálu za podmienok dynamického zaťažovania. Práca predstavuje kompletný proces vývoja, montáže a testovania nového testovacieho zariadenia zameraného na dosiahnutie symetrického nárazu dvoch vzoriek materiálu v pohybe. Zariadenie je testované v dvoch konfiguráciách, pričom sú opísané výsledky oboch. Boli vykonané materiálové testy smrekového dreva, ktoré boli následne porovnané s výsledkami získanými z klasického Taylorovho kanóna. Boli zistené a opísané podstatné rozdiely. Ukázalo sa, že vykonané simulácie symetrického nárazu s využitím modelu smrekového materiálu nezodpovedajú praktickým experimentom, čo naznačuje potrebné zmeny modelu.

Kľúčové slová

Taylorova skúška, symetrická, skušobné zariadenie, smrek, drevo

ROZŠÍRENÝ ABSTRAKT

Trendom posledných rokov v rôznych odvetviach výrobného priemyslu je zvyšovanie objemu výroby a jej zrýchlovanie, s čím súvisí použitie vhodných materiálov. Pochopenie ich mechanických vlastností, najmä pri rôznych rýchlostiach deformácie, je kľúčové pri predpovedaní ich správania, z čoho vyplýva aj optimalizácia ich použitia. S vývojom automatomatových výrobných zariadení, používaných napríklad pri výrobe spojovacích súčastí je kadencia výroby v stovkách výrobkov za minútu.

Materiál zaťažovaný pri dynamických podmienkach, teda za zvýšených rýchlostí deformácie, sa správa odlišne od materiálu zaťažovaného pri kvazistatických podmienkach. Medzi hlavné zmeny patrí zvýšenie sily potrebnej k pretvoreniu materiálu, a teda k zvýšeniu medze sklzu. Zatiaľ čo v oblasti rýchlostí deformácie do 10^3 za sekundu je nárast sily relatívne lineárny, po prekročení hranice dochádza k jej výraznému zvýšeniu. Tento efekt je spojený s dynamickou medzou sklzu, ktorú je možné pozorovať najmä pri dynamickom namáhaní. Vysvetlení jej vzniku je viacero, možno však hovoriť o akomsi "usadení" intersticiálnych atómov v priestoroch dislokácií, ktoré sú hlavným činiteľom pri rozvoji deformácie. Ak však dôjde k usadeniu, intersticiálne atómy vytvárajú na hraniciach dislokácií väzby, uvoľnenie ktorých požaduje zvýšenú silu, čím následne vznikne prudký nárast medze sklzu, ktorá poklesne z dôvodu nedostatku času potrebného na vytvorenie nových väzieb. Pri vyššej rýchlosti deformácie dochádza taktiež k lokálnemu zvýšeniu teploty materiálu, ktoré je spôsobené vnútorným pohybom častíc, vďaka čomu sa pri extrémnych podmienkach materiál začína správať ako tekutý. V neposlednom rade je potrebné spomenúť zmeny mikrotvrdosti a štruktúry. Dochádza k zvýšeniu tvrdosti a zjemneniu zrnitej štruktúry materiálu.

Problematike správania materiálu pri dynamických podmienkach sa v minulých storočiach venovalo mnoho výskumných tímov a vedcov. John Hopkinson v roku 1872 prezentoval prácu zameranú na pozorovanie správania materiálu v podobe drôtu, na ktorý bolo zavesené závažie. Pre dosiahnutie dynamických podmienok bolo ďalej implementované padajúce teleso o danej váhe, ktoré po dopadnutí na zavesené závažie vyvolávalo v materiáli impulzné zaťaženie. Bolo vyhodnocované miesto pretrhnutia drôtu v závislosti na váhach jednotlivých telies. Túto metódu neskôr rozvíjal, na čo naviazal jeho syn a následne Kolsky. Tento typ testu je preto dnes známy pod názvami Kolskyho tyč, či Hopkinsonova merná tyč. Rôzne zariadenia využívajúce tento princíp dokážu namáhať materiál v tlaku, v ťahu a v šmyku. Špeciálnou vlastnosťou tejto metódy je vytvorenie jednoosej napätosti v materiáli, čo má za následok deformáciu vzorky bez vzniku súdočkovania, ktoré je možné pozorovať pri kvazistatických kompresných skúškach.

Geoffrey Ingram Taylor v roku 1946 prezentoval metódu dynamického zaťažovania valcových vzoriek. Jeho prístup spočíval vo vystrelení takejto vzorky na pevnú prekážku. Výsledkom testov bol materiál deformovaný vysokou rýchlosťou deformácie. Taylor zároveň predstavil model výpočtu, ktorý mal slúžiť pre jednoduché a rýchle vyhodnotenie skúšky, založené len na známych materiálových vlastnostiach a rozmeroch skúšobnej vzorky pred a po teste. Tento model prezentoval s niekoľkými predpokladmi, ktoré vzhľadom na výpočtové schopnosti a meracie zariadenia potrebné na vyhodnotenie v danej dobe boli akceptované. Postupom času sa však táto metóda vyvíjala v kontexte dostupných technológii a jej isté nedostatky boli dopĺňané obmenami spôsobu testovania.

Medzi tieto nedostatky patrí napríklad problém testovania materiálu pri zvýšenej teplote. Aj keď je takýto test možný pri klasickom spôsobe, udržanie zvolenej teploty počas testu je obťažné. Jednak nastáva problém pri ohreve vzorky, ktorá ak je ohrievaná mimo testovacieho zariadenia, chladne počas prenosu. Druhým problémom je, že teplota vzorky prirodzene ďalej klesá pri výstrele. Z tohto dôvodu bolo v roku 1982 Gustom vyvinuté reverzné usporiadanie tejto skúšky, kedy je na stacionárnu vzorku vystrelený pohybujúci sa pevný projektil.

Vďaka tomu môže byť dosiahnutá teplota jednoducho monitorovaná a udržiavaná počas celého priebehu testu.

S vývojom vysokorýchlostných kamier sa takéto usporiadanie taktiež osvedčilo vďaka možnosti bezpečného sledovania nárazu pevného projektilu na vzorku a jednoznačného zaostrenia obrazu pre následné vyhodnotenie pomocou obrazovej analýzy.

Ďalším z problémov klasickej Taylorovej skúšky je vznik trecích síl na rozhraní plôch dopadovej prekážky a vzorky. Tento fakt bol známy aj Taylorovi, ktorý ho popísal pomocou priebehu vlákien materiálu v blízkosti dopadového čela. Tu je možné pozorovať očakávané odklonenie od osi v smere deformácie, avšak v blízkosti dopadového čela vlákna menia smer a zahýbajú sa naspäť do osi vzorky. Tento fenomén sťažuje jednoznačný opis správania materiálu a jeho riešenie je možné symetrickým usporiadaním testu. V tomto prípade je pevný projektil, alebo prekážka, nahradená druhou vzorkou rovnakých rozmerov a materiálu. Ak je dosiahnutý sústredný dopad vzoriek, ich čelné plochy sa deformujú súčasne, tým pádom nevzniká žiadne trenie. Takéto usporiadanie bolo predstavené Erlichom a spolupracovníkmi v roku 1982. Upevnenie stacionárnej vzorky je v tomto prípade možné niekoľkými spôsobmi. Niektoré výskumné skupiny využívaju teflónové strediace krúžky, prípadne teflónový náboj, do ktorého je vzorka upevnená. Ďalším spôsobom je uchytenie pomocou pružinou predpätých káblov so špeciálnou povrchovou úpravou, ktorá znižuje trenie vznikajúce medzi nimi a povrchom vzorky. Vzhľadom k stacionárnej polohe jednej zo vzoriek je tiež možné využitie vysokorýchlostných kamier.

V súčasnej dobe je v Laboratóriu vysokých rýchlostí deformácie na Fakulte strojního inženýrství VUT dostupné zariadenie pre Taylorov test v klasickom usporiadaní, teda s vystrelením vzorky. Na základe vyhodnocovaného materiálu je možné použitie pevnej prekážky ako dopadovej oblasti, ale taktiež tyče z vysokopevnostnej ocele Maraging, ku ktorej sú pripevnené tenzometre merajúce jej odozvu na dopad vzorky. Na základe elastickej deformácie tyče a ďalších zmeraných veličín je následne možné vyhodnotenie testu pre daný materiál. Zariadenie využíva na urýchlenie vzorky stlačený vzduch, ktorý je do palebnej komory privedený zo vzduchovej nádrže pripojenej ku kompresoru. Rýchlosť vzorky je zaznamenávaná zariadením pracujúcim na princípe svetelnej brány, kde je podľa rozdielu času pretnutia dvoch svetelných lúčov a ich vzájomnej vzdialenosti získaná výsledná dopadová rýchlosť. Vzorky sú do dopadovej komory dopravované v nosičoch, ktoré sú vyrobené technológiou 3D tlače. V minulosti boli používané vypenené polystyrénové nosiče, ktorých výroba však bola časovo nákladná a prípadná zmena geometrie vzorky bola ťažko implementovateľná. Rýchlosť dopadu dosiahnuteľná na tomto zariadení je do 300 $m \cdot s^{-1}$.

Na princípe tohto zariadenia malo byť podľa cieľov práce vyvinuté nové zariadenie. Toto zariadenie malo dosiahnuť symetrický a centrický dopad dvoch proti sebe letiacich vzoriek. K stavbe zariadenia mali byť využité komerčne dostupné materiály.

Súčasťou prvého návrhu zariadenia bola aj voľba hlavných materiálov. Celé zariadenie je usadené na hliníkovom profile s rozmermi 60 mm x 120 mm o dĺžke 4,7 m. Tento profil je postavený na podpornom ráme z hliníkových profilov. Pre streľbu vzoriek boli využité vodovodné trubky s vonkajším priemerom 25 mm. Táto voľba sa odvíjala od geometrie nosiča vzorky, jeho vonkajší priemer 16,5 mm vyhovoval vnútornému priemeru trubky 17,6 m.

Úvodnou časťou zostrojenia zariadenia bolo vytvorenie podporného rámu. Na jeho stavbu boli použité prebytočné hliníkové profily, ktoré boli dostupné v laboratóriu. Na základe výpočtu prehybu nosného profilu bol stanovený potrebný počet podporných bodov a ich rozloženie po dĺžke profilu. Vo výsledku boli zvolené 4 podporné body, dva na koncoch a dva v blízkosti stredu profilu, vzdialené 0,7 metra od seba. Na ich pevné spojenie boli použité najskôr plastové dielce z 3D tlače, ktoré však neboli dostatočne pevné a preto boli následne nahradené oceľovými uholníkmi. Vzhľadom na nerovnosť podlahy v laboratóriu boli na spodky profilov

pridané výškovo nastaviteľné nožičky pozostávajúce zo skrutiek upevnených v profile a plastových nožičiek, v ktorých sedia hlavy skrutiek. Rám pozostáva z dvoch segmentov na oboch stranách, ktoré sú v strednej časti spojené tenšími hliníkovými profilmi umožňujúcimi jednoduchý prístup k potrebným častiam zariadenia.

Následne boli navrhnuté držiaky pre vodovodné trubky, ktoré boli taktiež vyrobené pomocou 3D tlače. Skladajú sa z 3 častí, a to podložky, spodného a vrchného dielu držiaku. Spodný diel a podložka sú pevne pripevnené k nosnému profilu, vrchný diel je uťahovaný pomocou dlhšej skrutky a matice zachytenej pod spodným dielom. Z dôvodu bezpečia personálu laboratória bolo navrhnuté dopadisko, v ktorom ústia obe trubky. Jedná sa o box zvarený zo 6 dielov vyrezaných z oceľovej platne hrúbky 10 mm za pomoci plazmy, pričom jednotlivé diely obsahujú otvory pre uchytenie k nosnému rámu a taktiež otvory pre odvod vzduchu. Ten je do systému dodávaný zo samostatného kompresora so 100 litrovou nádržou. Vzhľadom na veľkosť nádrže bol do zariadenia implementovaný elektricky ovládateľný ventil, ktorý je prepojený s časovačom. Časovač je možné nastaviť do rôznych módov a ovládať časové úseky.

Pre vloženie vzoriek do zariadenia bol použitý t-kus, do ktorého je spodným prípojom vháňaný vzduch. Z dôvodu rôznych vnútorných priemerov v pripojeniach t-kusu a priechodky trubky bolo ručné vkladanie vzorky náročné. Z tohto dôvodu bol vyvinutý jednoduchý prípravok. Skladá sa z viacerých častí, pričom všetky boli vytlačené za pomoci 3D tlače. Zložený prípravok funguje tak, že po vložení vzorky s nosičom do vnútorného otvoru je celý zasunutý do t-kusu, kde následne dosadá na poslednú hranu priechodky, ďalej je vzorka v nosiči z prípravku vytlačená až do predurčenej vzdialenosti v trubke.

Pre prvé testy zariadenia boli zvolené hliníkové vzorky dostupné v laboratóriu. Po natlakovaní kompresoru boli vzorky vložené do trubiek. Časovač bol nastavený do impulzného módu, pri ktorom je možné nastavenie doby, po uplynutí ktorej sa uzavrie okruh na 0,5 sekundy, počas čoho je ventil otvorený. Celkovo boli otestované 4 páry vzoriek.

S výsledkami prvých testov boli pozorované isté nedostatky zariadenia. Jednalo sa o tlakové straty v systéme, ktoré spôsobovali neuspokojivé deformácie vzoriek, z pôvodného priemeru 5 mm na 5,05 mm. Ďalším problémom bola centricita dopadu. Pri pozorovaní dopadových čiel bolo jasne vidieť posun stredov vzoriek, ktorý bol odhadnutý na rozmedzie 1,2 mm až 1,3 mm. V neposlednom rade boli zistené aj štrukturálne nedostatky, ktoré sa prejavili popraskaním držiakov. Ich porušenie bolo spôsobené orientáciou tlače, ktorá spôsobila ich náchylnosť k praskaniu v prípade silového pôsobenia v smere kolmom na orientáciu.

Na základe prvých výsledkov bolo zariadenie prestavané. Hlavným cieľom bolo zníženie straty tlaku v systéme a z toho plynúce zvýšenie výslednej deformácie. Z toho dôvodu bol pridaný druhý ventil rovnakého typu, pričom oba sú pripojené na rovnaký časovač. Ventily boli presunuté na spodnú stranu nosného profilu a posunuté čo najbližšie k začiatku hlavne. Držiaky boli taktiež predizajnované, v novej konfigurácii uchytávajú len jednu trubku. Pozornosť bola venovaná aj zmene orientácie tlače, ktorá zvýšila ich pevnosť. V novej podobe držiaky na pevné uchytenie trubky spoliehajú na mechanizmus, ktorý vďaka svojej elastickej deformácii vyvoláva dostatočný tlak. Pre zlepšenie centricity dopadu bola ďalej implementovaná centrovacia tuba, ktorá má dostatok otvorov pre odvod vzduchu a nasádza sa na hlavne v dopadovej komore. Pridaný bol aj novo vyvinutý mechanizmus na meranie rýchlosti, ktorý sa však pri rýchlostiach prevyšujúcich 45 $m \cdot s^{-1}$ neosvedčil.

Zariadenie bolo po úplnom zostavení opätovne otestované s rovnakými hliníkovými vzorkami. Výsledky ukázali výrazné zlepšenie deformácie, z 5 mm na 5,43 mm, ako aj centricity dopadu, ktorá sa pohybovala v rozmedzí 0,1 milimetra.

Na materiálové testy bolo zvolené smrekové drevo. Táto voľba bola ovplyvnená dostupnosťou výsledkov testovania pomocou klasického taylorovho kanónu a s tým súvisiacich materiálových modelov.

Polotovar na výrobu vzoriek pochádzal zo stromov nórskeho smreku veku 25 až 30 rokov. Následné polovýrobky v podobe štvorcových hranolov boli skladované v uzavretom prostredí pri teplote 2°C. Takýto spôsob skladovania bol zvolený, aby sa predišlo strate prirodzenej vlhkosti dreva.

Na výrobu vzoriek boli najskôr osústružené dva hranoly na priemer 10 mm, z ktorých bolo následne pomocou píly narezaných 14 kusov o dĺžke 20 milimetrov. Vzorky boli ďalej označené a ich rozmery a váha zmerané. Pre väčšiu veľkosť vzoriek boli prispôsobené nosiče, avšak pre nepravidelný priemer boli niektoré vzorky obalené pásom papiera pre docielenie tesného uchytenia v nosiči.

Vzhľadom na nefunkčné meranie rýchlosti bol počas experimentov zaznamenávaný tlak, pri ktorom boli vzorky vystrelené. Pomocou tlaku bola odhadnutá ich rýchlosť v závislosti na nameraných rýchlostiach pri klasickom taylorovom kanóne.

Výsledky materiálových testov ukázali nečakané výsledky. Pri prvých vzorkách vystrelených pri vyšších hodnotách tlaku došlo k ich "zlúčeniu" do istej hĺbky, ktorá bola vyhodnotená na základe pôvodných dĺžok. Takto spojené vzorky nebolo možné ručne oddeliť. Taktiež bolo pozorované očakávané poškodenie vzoriek v pozdĺžnom smere.

Zaujímavejšie výsledky boli pozorovateľné na vzorkách vystrelených pri nižších hodnotách tlaku. V týchto prípadoch došlo k nehomogénnemu poškodeniu drevitej štruktúry, kde sa javilo jasné zatlačenie včasného, mäkšieho dreva, v smere osi, pričom neskoršie drevo zostalo takmer bez porušenia. Vznikala členitá štruktúra najlepšie pozorovateľná na vzorke, pri príprave ktorej došlo k poškodeniu. Vďaka predchádzajúcemu porušeniu bolo možné jednoduchšie pozorovanie zatlačenia včasných oblastí dreva v smere do materiálu.

Pre porovnanie bol vystrelený posledný pár vzoriek dreva, ktoré neboli špeciálne skladované, a teda ich odhadovaný pomer vnútornej vlhkosti sa pohyboval v rozmedzí 10 % až 15 %. Tieto vzorky boli vystrelené pri vyšších rýchlostiach, avšak nedošlo k ich spojeniu ako v prípade vzoriek s vyššou vlhkosťou. V tomto prípade bola vzniknutá štruktúra ešte evidentnejšia a zatlačenie mäkšieho dreva výraznejšie. Čelo tejto vzorky bolo pozorované pod svetelným mikroskopom.

Po získaní výsledkov boli na základe materiálových modelov z predchádzajúcich štúdií vyhotovené simulácie nárazu pomocou simulačného softwaru Ansys v študentskej verzii 2024 R1. Na simuláciu boli zvolené rýchlosti párov vzoriek 1 a 5. Simulácie však neukázali zhodu s pozorovanými výsledkami. Dôvodom tohto problému je nehomogénna štruktúra dreva, teda pre zhodné výsledky by bolo potrebné vytvorenie komplexnejších modelov zložených z viacerých vrstiev.

Na základe výsledkov bolo zariadenie vyhodnotené ako použiteľné pre budúce výskumy v oblastiach materiálových skúšok. Vďaka inovatívnemu prístupu eliminuje niektoré známe problémy klasického taylorovho testu. Ďalšou výhodou je možnosť testovania vzájomného pôsobenia organických materiálov.

BIBLIOGRAPHIC CITATION

GAJDOŠÍK, Matej. *Vliv rychlosti deformace na mechanické vlastnosti materiálů* [online]. Brno, 2024. Dostupné z: https://www.vut.cz/studenti/zav-prace/detail/154101. Diplomová práce. Vysoké učení technické v Brně, Fakulta strojního inženýrství, Ústav strojírenské technologie. Vedoucí práce Miroslav Jopek.

AFFIRMATION

I hereby declare that I have prepared my Master's thesis on the topic Effect of strain rate on the mechanical properties of materials independently, utilizing the literature and materials listed, in accordance with consultations under the supervision of the thesis supervisor.

place, date

Bc. Matej Gajdošík

ACKNOWLEDGMENT

I would like to thank Ing. Miroslav Jopek, PhD. for his valuable comments and advice, for his supervision of my thesis, and for creating a pleasant environment where cooperation is valued. Next, I would like to thank Mr. Vojtěch Řiháček for his help with electronics, to Ing. Radek Řídký and Ing. Jan Řiháček, PhD. for their help and tips regarding simulations. My gratitude also extends to all my friends and classmates, who landed a helping hand in various stages. Last but not least I would like to thank my family for the continuous support of my studies and to my closest one for all the encouragement.

TABLE OF CONTENTS

INTRODUCTION

The focus of the production industry in recent years has been the enhancement and optimization to increase productivity and manufacturing speeds, leading to an increase in the strain rate imposed on the formed material. This causes an increase in demand for testing equipment capable of replicating forming conditions of actual production, for a better understanding of the material's behavior. [1; 2]

This trend does not extend only to the production industry, many other types of industries require knowledge regarding the effects of strain rate on a material. For example, the automotive industry uses such data to better predict crashes, in aviation the effect of the environment on the material throughout the flight is substantial, and the military and arms industry also takes interest in research of materials undergoing high rates of strain. [3; 4; 5]

One of the best examples of high strain rate deformation in use is the production of small fastening and connecting materials, examples of which can be seen in Fig. 1, that are made using high-rate automatic sequential machines with production rates of 300 – 600 pieces per minute, which causes the material to reach strain rates of up to 10^3 s^{-1}. Furthermore, modern machines are capable of high-speed forming at both room temperature and the heated state of the material. [2; 6]

Fig. 1 Examples of parts from a high-rate automatic sequential machine [7; 8].

1 INTRODUCTION TO THE SOLVED PROBLEM

This thesis aims to investigate the effect of strain rate on material behavior and its mechanical properties. For this purpose, the theoretical section will be dedicated to material testing under selected conditions and a chosen technique will be discussed in more detail. Another goal is to develop and assemble a functional device for the dynamic testing of material, which will be based on the principles of a device already in use. After completion a selected material will be tested, assessing capabilities, advantages and disadvantages, and overall usability of the proposed design. Upon successful tests of the material, the results will be evaluated.

The importance of knowing how a material behaves during dynamic load is evident from Fig. 2, which shows a division of forming processes based on the forming speed. Most of these processes take place under dynamic conditions, where material behavior differs from quasistatic expectations. This difference can cause defects and other unsatisfactory phenomenons of products. [9; 10]

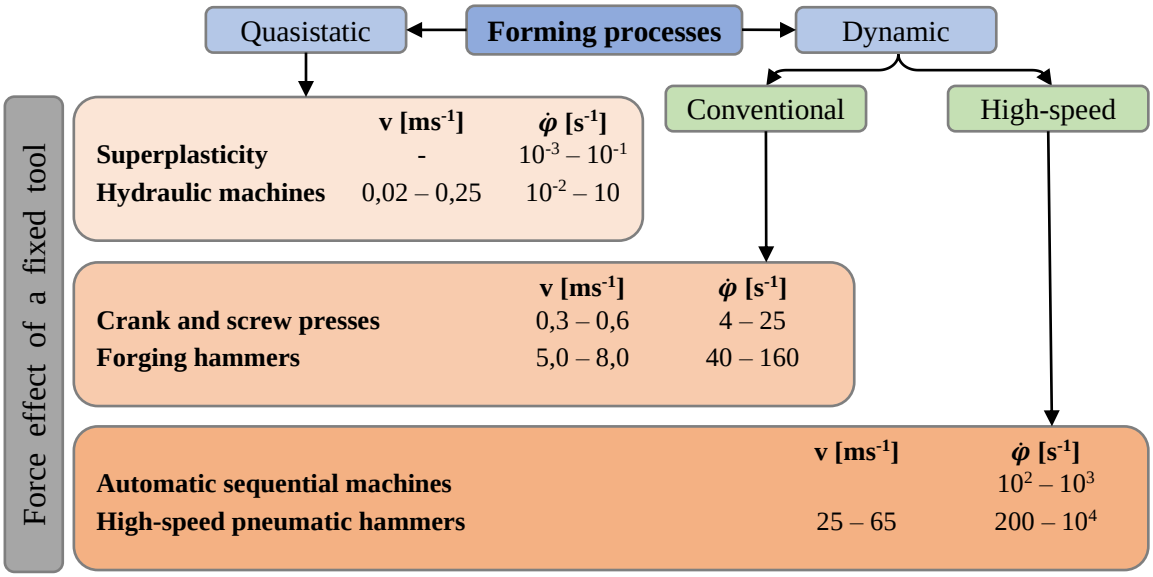

Fig. 2 Division of forming processes [1].

Knowledge of dynamic material behavior is essential when a numerical simulation of a selected process is required, which in light of production industry trends of recent years is employed in the development process more often than not. The cause is a great increase in the effectiveness of manufacturing by providing useful information on possible problems. For a simulation to be successful and comparable to real-life situations, correct input parameters and factors influencing the calculation are necessary. These include material characteristics, speed of the process, friction, temperature, and boundary conditions. Under dynamic conditions, more parameters need to be included as they bear a sizable influence on the material, such as structural changes, strain rate, and strain wave dissemination. Without proper inputs, the results of the simulation are inequitable of the process, resulting in unsatisfactory dimensional accuracy, functionality, or failures within a production line. [9; 10]

Furthermore, this argument can be supported when investigating flow conditions of basic forming technologies depicted in Fig. 3. Processes of upsetting and direct extrusion are described regarding tool travel, speed, and strain rate of the material. The travel of the tool for both examples is equal to 2 mm. What needs to be noted, is the difference between the speed of forming tool and strain rate when comparing these technologies. While for upsetting, the strain rate reaches 20 s^{-1} in the axial direction, for extrusion the values fluctuate depending

on the angle of reduction from around 300 s^{-1} for a reduction angle od 30° to more than 800 s^{-1} when the reduction angle is 60°. Note that the extrusion values are considered for material in the area of reduction, as that is the focal point of deformation. [11]

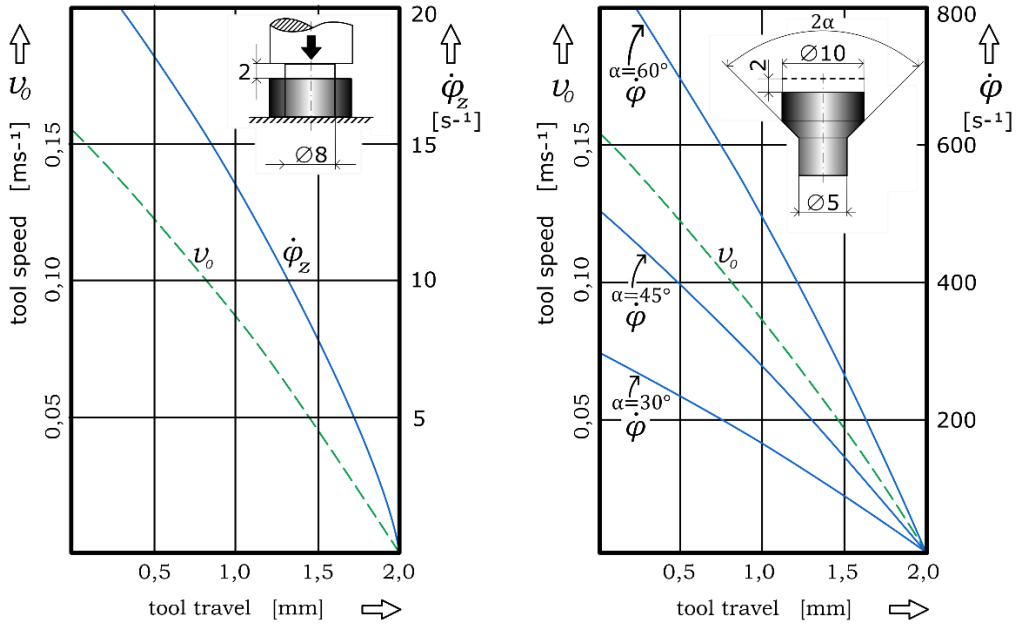

Fig. 3 Strain rate conditions of upsetting and direct extrusion [11].

1.1 Effects of dynamic behavior

Plastic deformation of material occurring at higher strain rates is influenced by many factors, including temperature, microstructure, and anisotropy, thus the yield strain is a function of those influences. This can be stated as $\sigma = f(\varphi, \dot{\varphi}, M, T, A)$. The strain rate describes the amount of deformation that occurred in an amount of time. [12; 13]

The influence of strain rate on the material is evident from Fig. 4, where a dependence of strain rate on the yield stress of low-carbon steel at various temperatures is shown. While at the speeds in the range of up to 10^3 s^{-1} the increase is almost linear, after an increase in speeds the yield stress value rises exponentially, especially at room temperatures. [13]

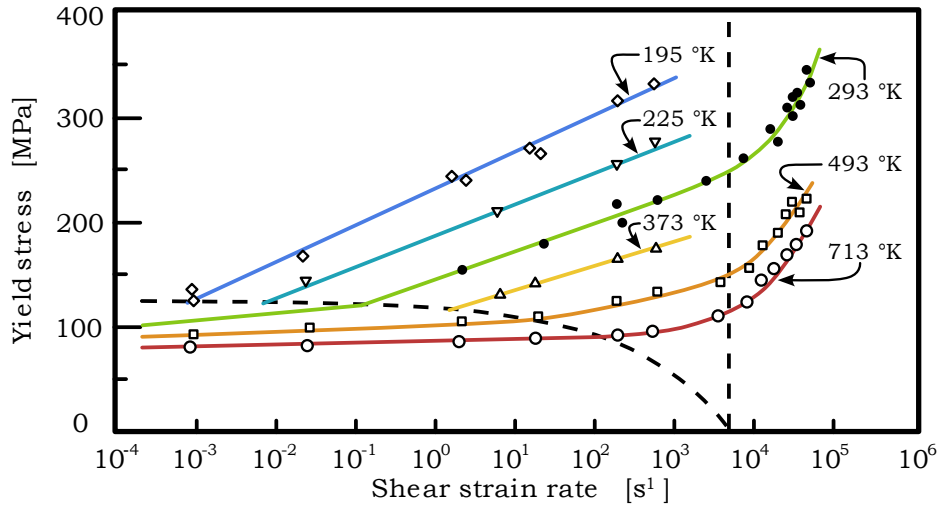

Fig. 4 Effect of strain rate on yield stress [13].

Another phenomenon occurring at dynamic plastic deformation is a so-called unstable yield point, Lüders bands, or dynamic strain aging. The manifestation of this can be seen in Fig. 5, where a stress-strain curve is outlined for dynamic and quasistatic processes. The curve of the dynamic process has a notable sharp increase in the yield point, with a sudden decrease thereafter. Following this, the curve has an expected shape. [12; 14]

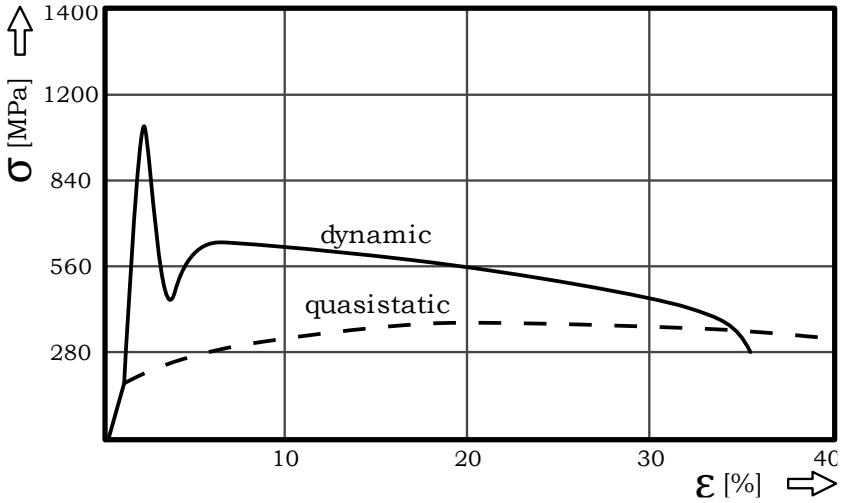

Fig. 5 Dynamic and quasistatic stress-strain curve [15].

The explanation of this effect is complex, with many possible reasons, however, it can be attributed to interstitial atoms within the material and their diffusion movement. They, as all matter, move to a place where their energy is at the lowest, which in metals are the areas of dislocations. Over time, the atoms here form a "bond" with the edges of dislocation that increases the necessary stress to release the dislocation – allowing its movement and thus plastic deformation. This creates a momentary increase in the value of strain, but as the deformation progresses, there is not enough time to form future "bonds", thus the strain value decreases. The process is more evident in Fig. 6. [15; 16; 17]

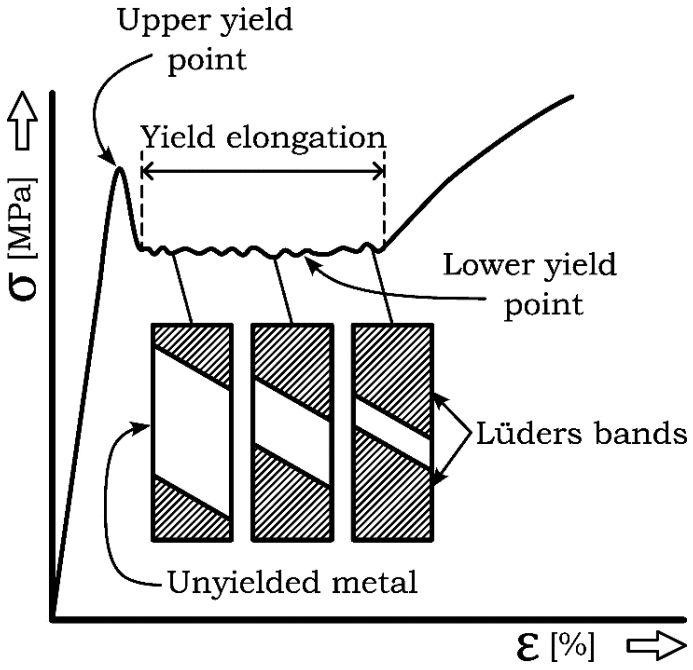

Fig. 6 Yield point phenomenon [18].

The effect of temperature, at which a forming process takes place can be described by Fig. 7, which shows results of tests performed at the Brno University of Technology. The tested material is 3D-printed steel G3Si1, which was tested at different temperatures and strains, but only selected results are depicted. The experiment performed at room temperature shows a sizable increase in flow stress in comparison to quasistatic testing, while as the temperature of the material was increased, an opposite effect can be observed. [19]

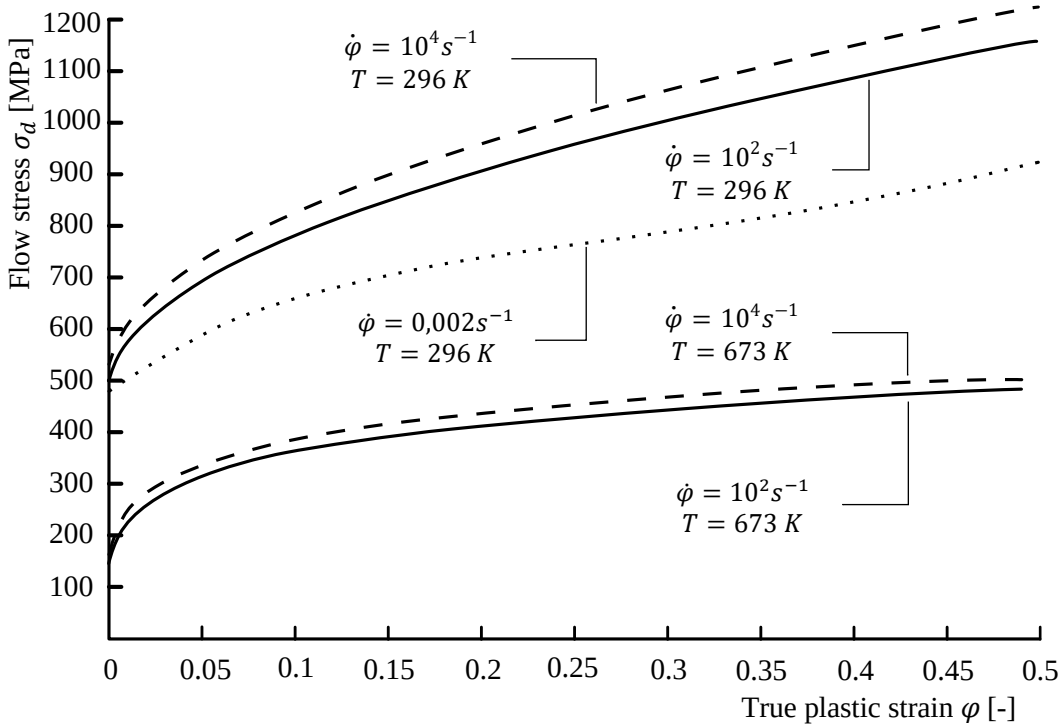

Fig. 7 Results of testing G3Si1 steel [19].

The information above stated clearly shows the importance of material testing at all different conditions of loading, from strain rate to temperature. For this reason, the theoretical part of this thesis is dedicated to material testing at dynamic conditions.

2 MATERIAL TESTS

As the thesis aims to investigate material behavior under the effect of strain rate, material tests are an inseparable part. Similar to forming processes covered in the previous part, various experiment methods can be also divided based on strain rate. Tab. 1 shows a division of compression testing, including dynamic characteristics and devices used. [13; 20]

Tab. 1 Compression test methods overview [13; 20].

Distribution by strain rate	**Range of strain rate** $\dot{\varphi}[s^{-1}]$	**Test methods**	**Devices**	**Dynamic characteristics**
Low rate	$\langle 10^{-5}\ ;\ 1\rangle$	quasistatic tests	standard equipment	constant strain and strain rate
Medium rate	$\langle 1\ ;\ 10^{3}\rangle$	fast loading	drop tower cam plastometers	mechanical response of the sample and the machine frame
High rate	$\langle 10^{3}\ ;\ 10^{5}\rangle$	dynamic loading	Hopkinson test Taylor test	propagation of plastic waves
Very high rate	$> 10^{5}$	impulse loading	explosion tests	shock waves

For a commonplace production industry material behavior under very high strain is not especially needed, coverage of the low, medium, and high-rate testing is sufficient for most of the forming processes involved.

Current equipment in the Laboratory of high-speed deformations of Brno University of Technology allows for testing of material at strain rates occurring during forming processes from quasistatic, circa 10^{-3} s^{-1} to high speed, circa 10^{4} s^{-1}, however, the aim is to increase the possible achievable strain rate of high strain test, as well as addressing further factors influencing measurements. This would provide an opportunity to test more advanced materials that are being developed, as well as simulate forming processes that make use of such high strain rates. [15]

In the next sections of this thesis, high-rate testing methods will be discussed. As one of the goals is a testing device development, more attention will be dedicated to the construction of individual designs and the way stresses are applied, measurements, and outcomes.

2.1 Hopkinson test

The original work published by John Hopkinson in 1872 marks a starting point for the development of this testing method for high strain rate deformation. The original work presented an experimental setup aimed at the investigation of iron wire rupture, which was impacted by a moving mass. The configuration of this setup was in a vertical position with the wire hanging from a rigid structure and a hanging mass attached at its end. The aim was to determine the location of wire rupture, either at the top end or at the bottom end, near hanging mass, depending on the weight of a moving mass for different diameters of the wire. [21]

Further investigation of this method conducted by Davies and Kolsky led to improvements in this method, change of orientation, and the mechanism of load induction. The experimental setup of Kolsky is shown in Fig. 8. where the specimen is under compression load. Over the years, devices utilizing similar principles have been developed. [22; 23; 24]

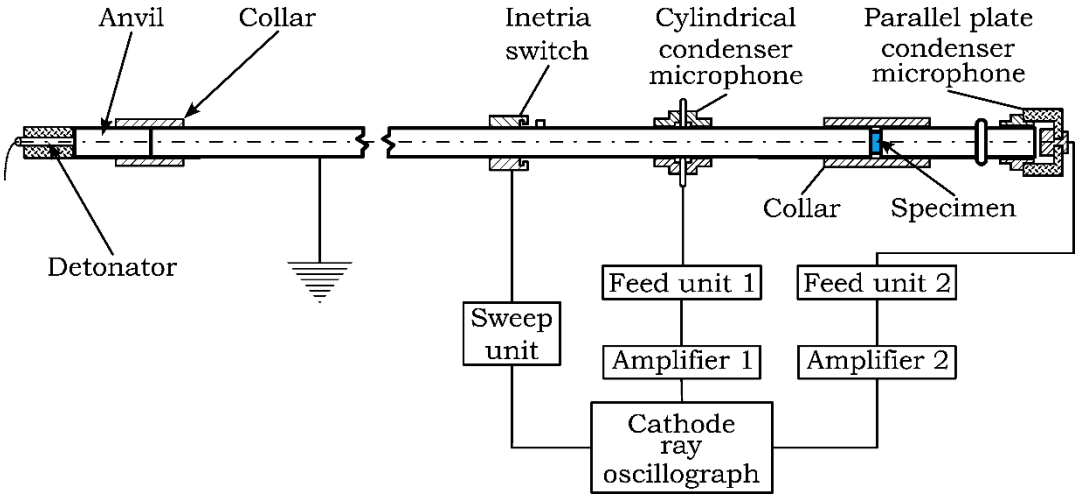

Fig. 8 Arrangement of Kolsky bar test [24].

Outside of pressure loading of material, known as the Split Hopkinson Pressure Bar test - SHPB, different types of configurations of this test are known and used, including tension, torsion, and shear, some of them shown in Fig. 26. Testing of material under increased temperature is also possible. [25; 26]

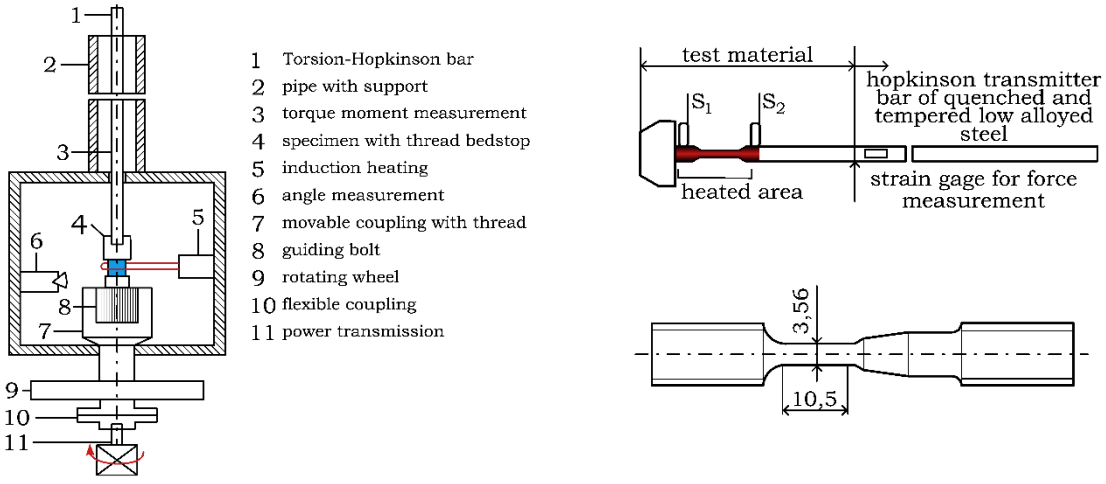

a) heated torsion b) heated tension

Fig. 9 Different configurations of the Hopkinson test [26].

The equipment in the laboratory of high-speed deformations is in pressure test configuration, see schematic in Fig. 10. The device consists of a specimen aligned between an input bar and an output bar with a fast-moving impactor of set dimensions providing the forming force in an impulse. The impactor is accelerated by compressed air, and its speed is measured by a speed gate. As it hits the input bar, its kinetic energy converts to potential energy and creates an elastic pressure wave – incident wave, that spreads throughout the material at the speed of sound and interacts with the sample, resulting in the creation of reflected and transmitted waves. The reflected wave is tensile, and it propagates in the input bar in the opposite direction to the

incident wave, while the transmitted wave spreads through the output bar. The strain history is measured by capacitive sensors installed on both the input and output bars at the required distance from the specimen. Measured values of elastic deformation of the bars are shown on an oscilloscope, from which data can be stored on a PC. [27; 28; 29; 30; 31]

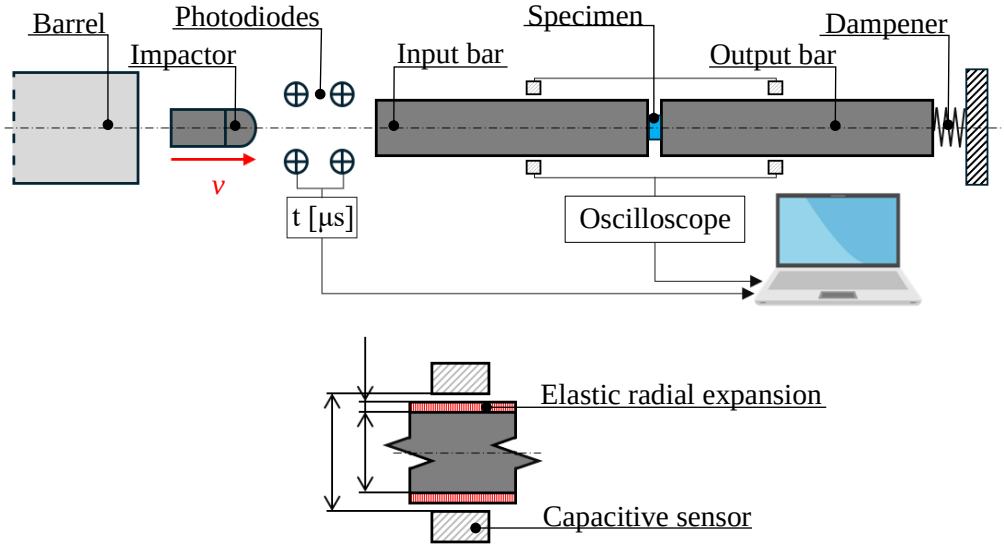

Fig. 10 Split Hopkinson Pressure Bar test scheme [32].

A unique feature of the Hopkinson test is the creation of uniaxial stress. This phenomenon is linked to the propagation of the stress waves, see Fig. 26a. As the incident wave reaches the first interface, part of it is transmitted into the sample, and as this transmitted wave reaches the second interface, it is again partly reflected back. This repeats many times, as the length of the incident wave is equal to the length of the impactor, creating an equilibrium within the sample. The result of this behavior can be seen through the specimen change (Fig. 26b). [22; 28; 30]

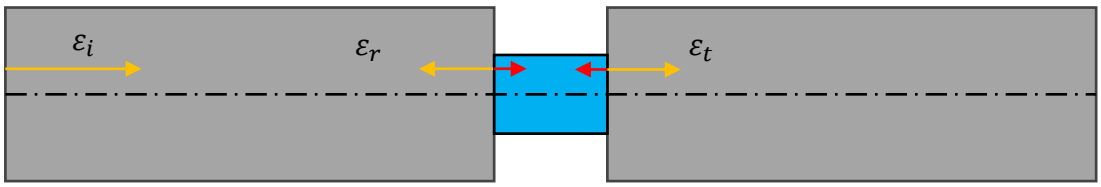

a) wave propagation

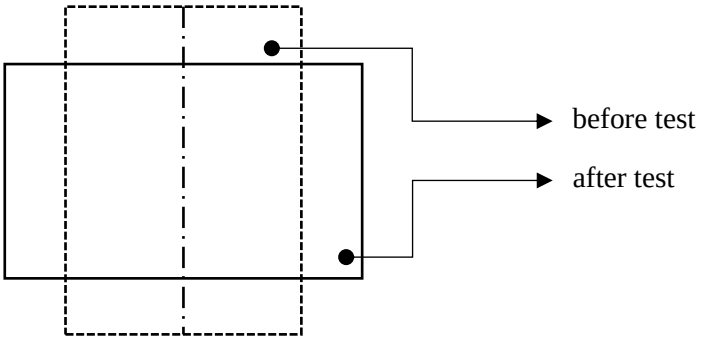

b) specimen dimensional change

Fig. 11 Effect of uniaxial stress [22].

2.2 Taylor Anvil Test

This test method is one of the simplest ways of evaluating the dynamic behavior of tested material. The principle lays is the acceleration of a specimen and its consequent impact on a rigid surface, which causes its deformation, as can be seen in Fig. 12. While the impact speeds may be in the range of hundreds of meters per second, strain rates induced to the material reach values of around 10^4 s^{-1}. Instantaneously upon collision, the exerted compressive force generates elastic and plastic waves that start to propagate throughout the specimen. The elastic wave, which propagates through the material at the speed of sound, rebounds from the specimen's free end and comes back as a tensile wave. [14; 33; 34; 35; 36; 36; 37]

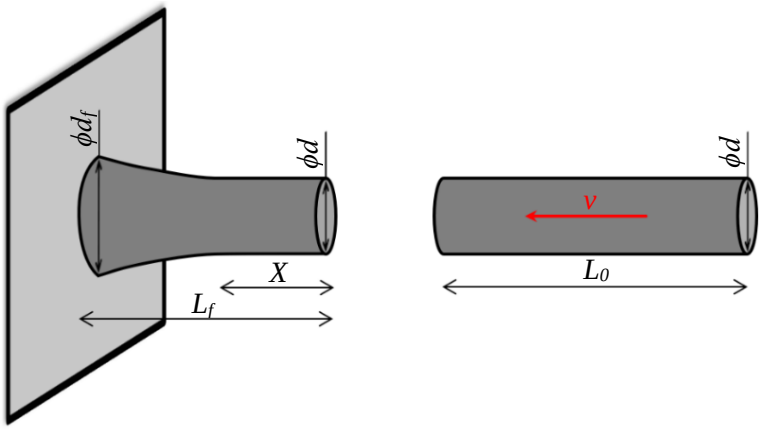

Fig. 12 Specimen during TAT [34].

This method, first presented by Geoffrey Ingram Taylor in the year of 1946, was an important step in the investigation of the mechanical properties of materials at high rates. The first proposal was based on firing of a circular specimen against a rigid anvil, which was set up as a ballistic pendulum. In later years, this was replaced by a static anvil. Taylor tested many different materials and presented results. Fig. 13 shows a rendering of deformed copper cylinders after testing depending on impact speed, approximated from figures published by Taylor. [33; 34; 35]

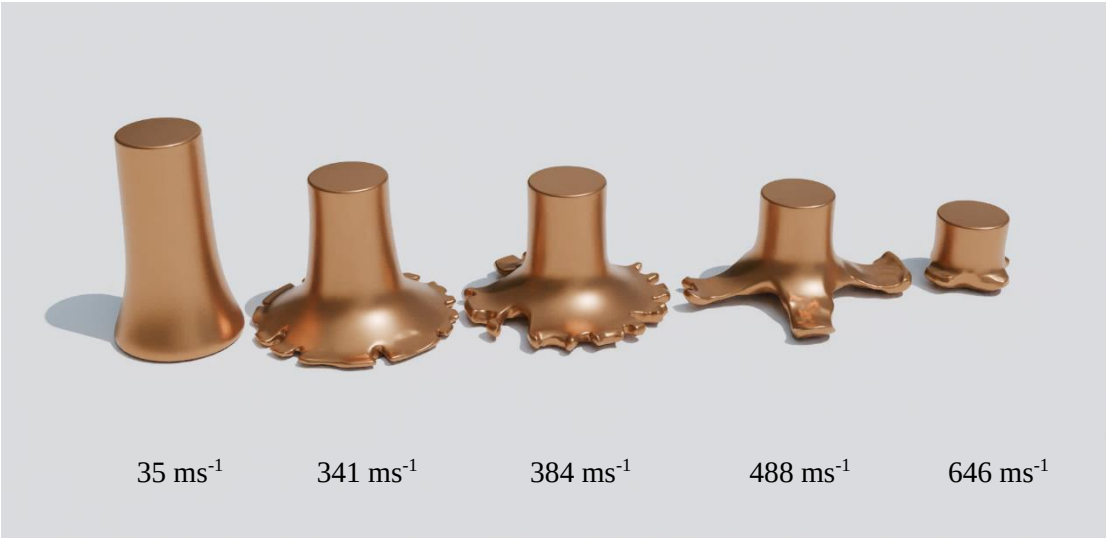

Fig. 13 Steel cylinders after a test [35].

2.2.1 Current laboratory equipment

The laboratory of high-speed deformations is currently in disposal of a TAT testing device, a schematic depiction of which is shown in Fig. 14. The assembly consists of an air compressor connected to an air tank, providing propulsion of the specimen during a test. The specimen is inserted through a loading chamber into the barrel, and as the pressured air is released, it is accelerated out of the barrel. Its speed is measured by a set of photodiodes situated before the barrel muzzle.

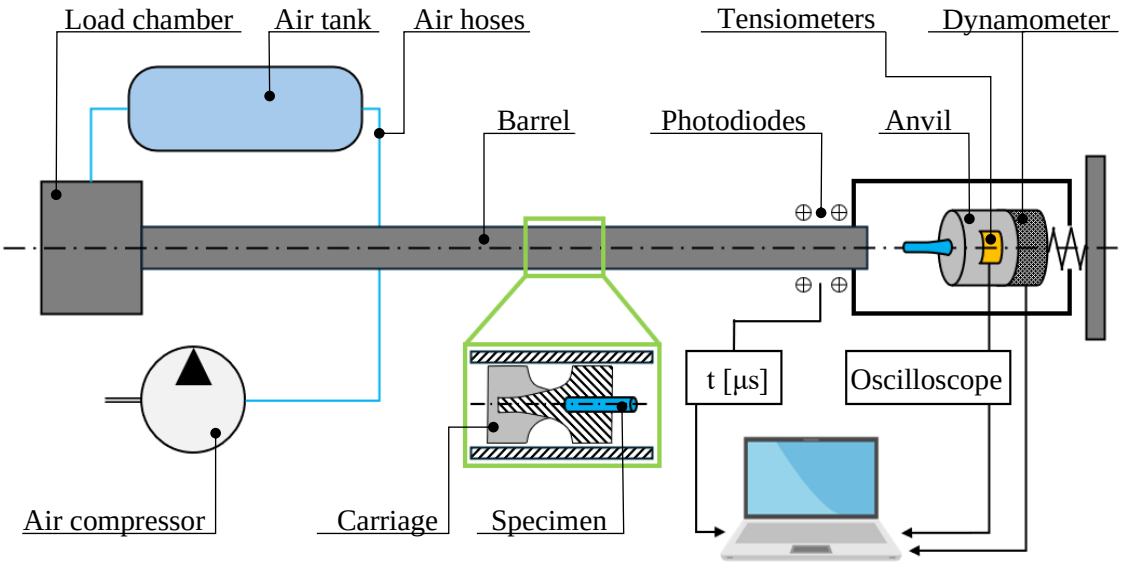

Fig. 14 Taylor Anvil Test device scheme [36].

The starting dimensions of a specimen are determined and measured before the test. The size needs to be moderated to make it light enough to ensure as high as possible impact speed, simultaneously guaranteeing that the plastic deformation is recognizable for further evaluation. The material needs to have the same structure and heat treatment as it would have had in the production line, thus no thermal influences can be introduced during the preparation process. If the samples need to be turned to the necessary dimensions, the depth of cut needs to be kept at a minimum with constant cooling throughout the process. As only the face is meant to be in contact with the rigid surface, it is the only place where allowances are required, mostly for grinding, which is done in a way that ensures that the face of the specimen is perpendicular to its axis and further operation of lapping may be utilized. After preparation, the dimensions and weight of the specimen are measured by an appropriately accurate measuring device, such as a micrometer and gram scale. Fig. 15 shows a drawing for specimen preparation with dimensions and geometrical constraints, that are used in the laboratory. [15; 37]

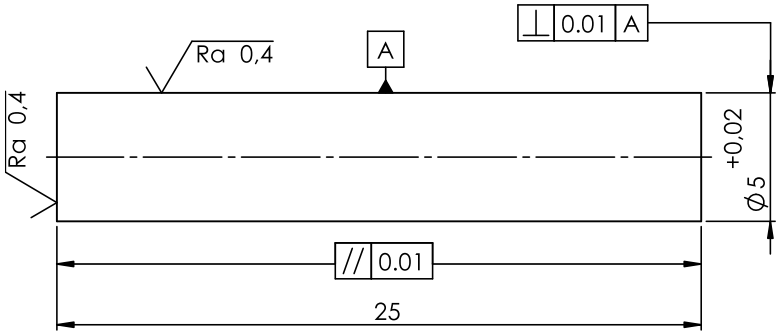

Fig. 15 Drawing of a test specimen [15].

The carriage used to deliver the specimen into the impact chamber has changed in 2022. While previously a polystyrene carriage was used, which was difficult and time-consuming to manufacture, a newly proposed design of the carriage utilizes 3D printing technology. This provided a more versatile and a lot faster way of manufacturing, with an easier way of implementing changes to the design, not requiring changes of polystyrene mold. The specimen is inserted into the carriage, which travels up to the impact surface, where it breaks apart upon impact, thus not interfering with the plastic deformation of the material. [38]

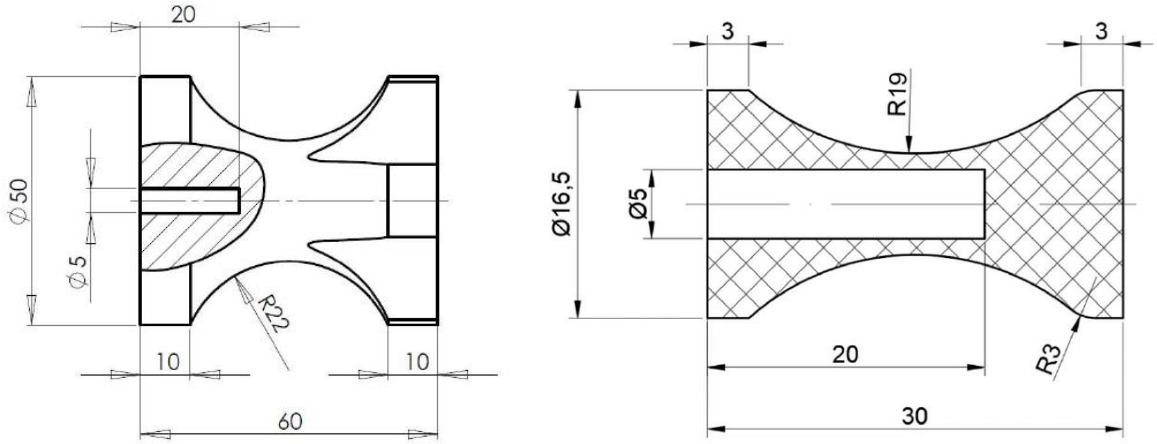

a) polystyrene carriage b) 3D printed carriage

Fig. 16 Types of carriage [38].

In the impact chamber, different types of impact surfaces can be placed. Currently available are the following:

- high-strength steel rod,
- rigid plate,
- direct impact on the Kistler dynamometer.

All of the mentioned impact surface configurations are shown in Fig. 17. The high-strength steel rod provides the ability to measure the dynamic response of material upon impact using strain gauges, however, a calibration of the rod is necessary for correct result readout. The plate provides a stable, rigid surface of impact, but the evaluation is limited. Direct impact onto a dynamometer is a source of ideal impact measurement but creates a risk of damaging costly equipment, therefore used rarely. [15; 32]

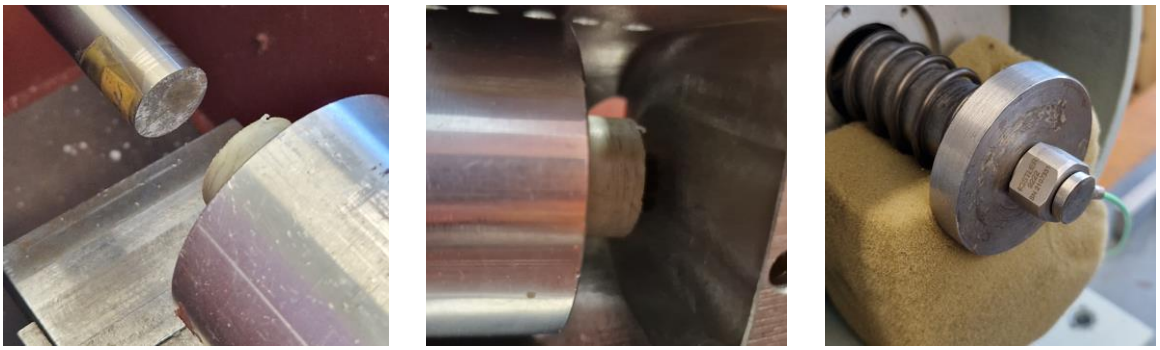

a) steel rod b) rigid plate c) dynamometer

Fig. 17 Configurations of impact surfaces.

2.2.2 Issues of TAT

There are some known issues associated with the Taylor test. One of these was described by Taylor himself in his works and is a part of all forming processes – friction. This effect occurs at the interface of impact during specimen deformation. In Fig. 26 a cross-section of a deformed steel specimen is presented from the original works of Taylor, in this case with inverted colors to better show the microstructural lines. These splay out of the axis of symmetry at the impacted face as expected, however, they bend inwards close to the specimen-anvil interface, showcasing the effect of friction that occurred. This problem was acknowledged and did not pose an issue at the time of this method development. [15; 34; 35; 36]

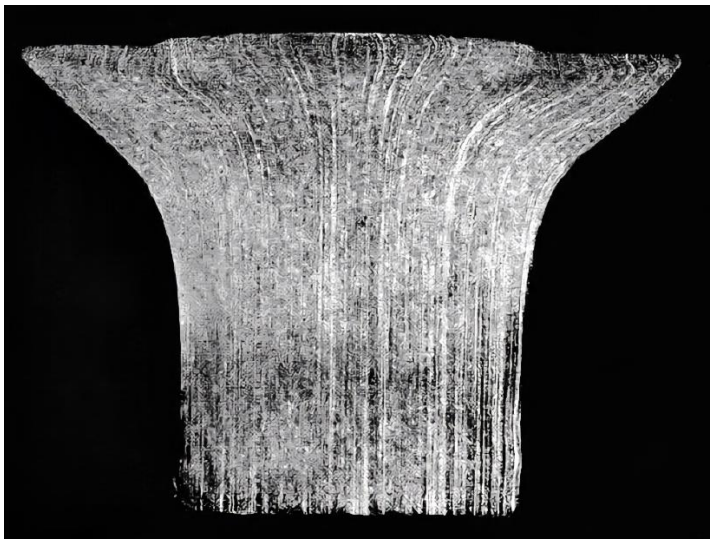

Fig. 18 Cross-section of a deformed specimen [36].

The next issue created on the interface lies within the definition of this method. As no material is ideally rigid, elastic deformation of the impacted surface can be observed. In the case of measurement using strain gauges, this effect is expected and used for validation. Fig. 26 shows a recording of TAT, where a pressure wave caused by an impact turns into a tensile wave upon reflection on the free end. Deformation of the sample may be affected by the propagation of elastic waves, similar to the principle of SHPB, thus interfering with results. [15; 32; 37]

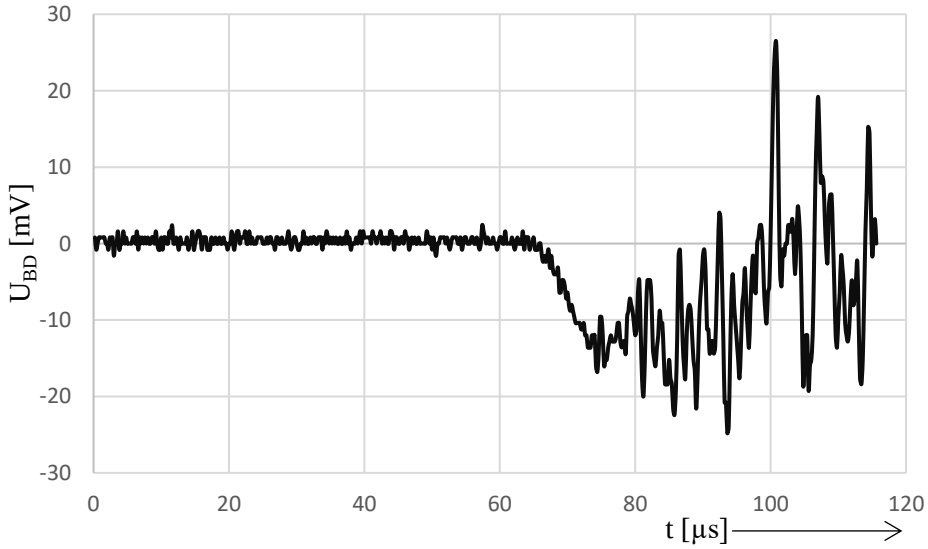

Fig. 19 Typical record of pulse waves [15].

Another way of tracking the plastic deformation of the specimen is to use a high-speed imaging camera. This can be difficult to achieve in the typical configuration of the test because a well-focused recording is required for further digital image investigation. [39]

Because of these issues, different configurations of the Taylor Anvil Test have been developed, which will be covered in the next chapters of this thesis.

2.3 Reverse Taylor Test

In the typical TAT configuration, testing of a material at elevated temperatures creates a challenge in maintaining a uniform temperature of preheated specimen throughout the test. To circumvent this issue, a reverse setup (Fig. 20) can be used, first proposed by Gust in 1982. The setup was designed to test the dynamic behavior at higher than room temperatures, utilizing an alumina anvil backed by an aluminum sabot impacting a heated tantalum sample. [40; 41]

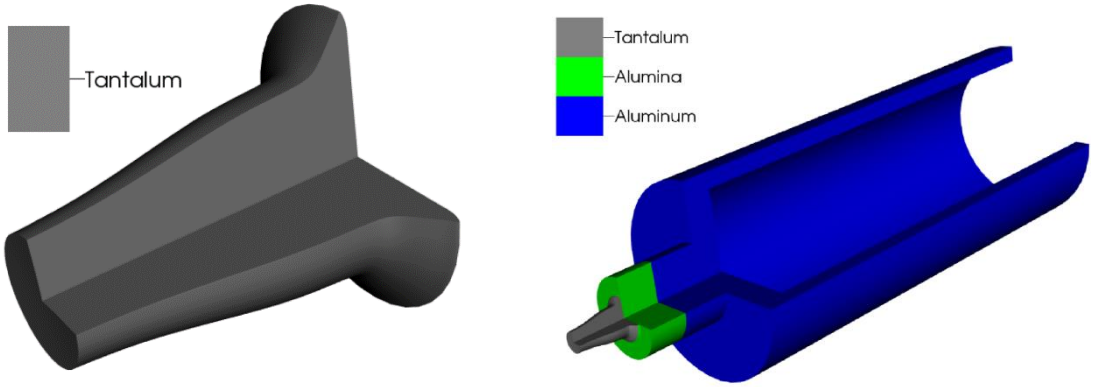

a) deformed specimen b) flyer configuration

Fig. 20 Reverse Taylor [41].

This type of configuration also allowed for high-speed camera recordings, as the specimen is stationary, allowing a proper focusing of the image. Such a setup can be seen in Fig. 21, where the specimen is held in place by a support disc, while the anvil, made out of rigid steel, is pushed through the barrel by an aluminum sabot via compressed air. The scheme also shows the high-speed camera recording range, which starts upon anvil impact on the crush pins that protrude a set distance over the specimen. A recovery tank is implemented to prevent further deformation of the specimen, while also allowing the piece to be recovered after the test. [42]

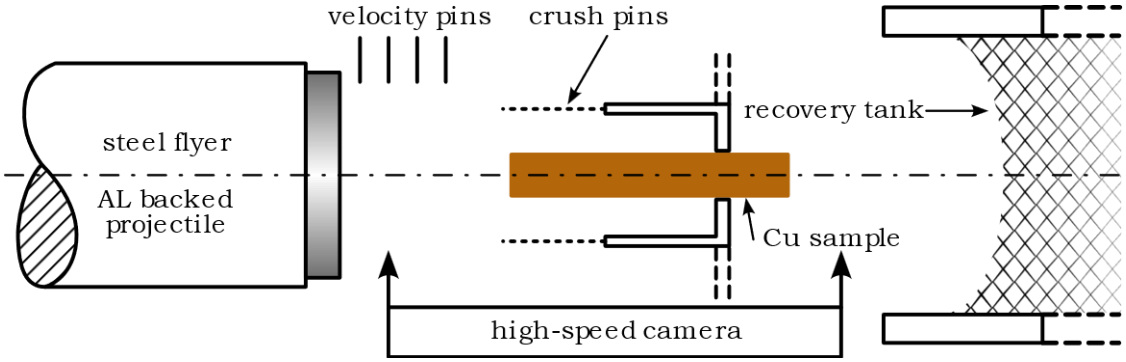

Fig. 21 Scheme of a reversed anvil test [42].

This principle is also beneficial in the case of penetration research of hard targets, such as reinforced concrete or plate metal, where stress sensors cannot be installed due to the characteristics of the test, while a high-speed camera provides sufficient information. [39]

A setup combining heating of material and high-speed recording is shown in Fig. 22. Here, the material is placed in a vacuum chamber with a furnace utilizing radiation heating elements. The specimen is held in place by a set of four wires, two near each end, keeping it in the correct orientation during the testing and also providing a way of temperature measurement. Light gates are used to determine the speed of the flying anvil before impact, while an optical velocimeter measures the speed of the rear face of the specimen. [43; 44]

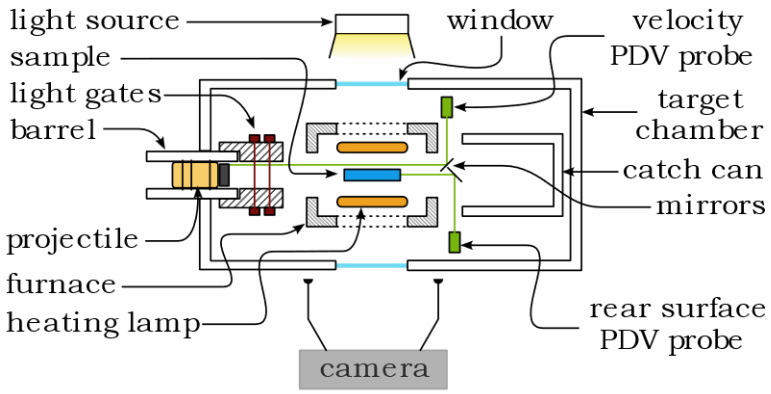

Fig. 22 Experimental set-up of heated reverse Taylor Test [43].

The results of the described test relied on the observation of high-speed photography recordings, see Fig. 23, and due to the close proximity of measuring equipment, no soft-catch recovery tank was implemented. This resulted in a noteworthy post-impact deformation of samples, rendering obtained data from scans and metrological investigation to be given a minimal focus. [43]

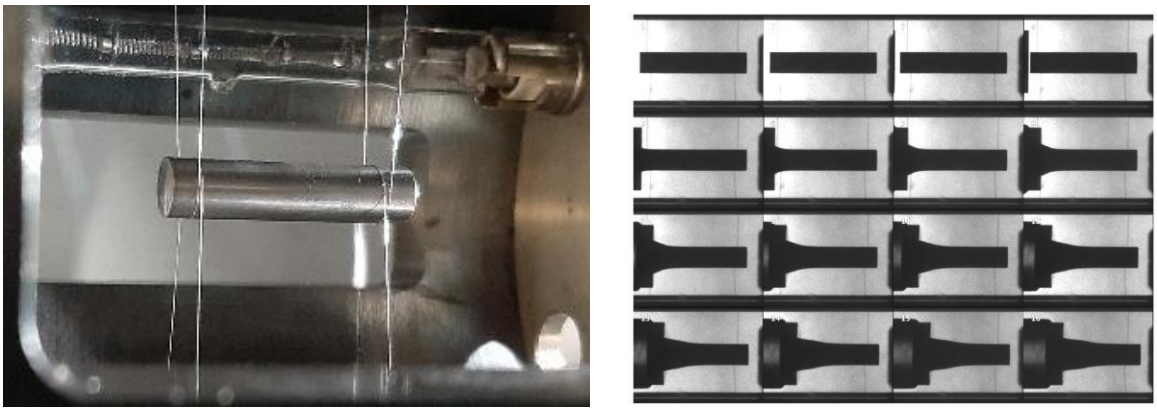

a) specimen setup b) 176 m/s, 807K

Fig. 23 Specimen and recorded results [43].

2.4 Symmetric Taylor Test

To counter the element of friction on the interface of impact, a symmetric Taylor test configuration, also known as Rod-on-Rod impact, is a viable option. Such a setup was first reported by Erlich and co-workers in 1982, where the rigid impacted body is replaced with another specimen of the same dimensions and material. [45; 46]

The test setup of Erlich involved a 6061-T6 aluminum rod with faces machined to be parallel to the axis. One of the rods was mounted at the muzzle of a helium gun, which accelerated the second rod fixated in an aluminum projectile. Soft-catch recovery tank filled with energy-absorbing material was used to retrieve samples after a test. A framing camera was used to record the impact, with 4 μs intervals between each image. [45]

More modern configurations of the test use different approaches to hold the impacted specimen in place and axially aligned. An example of such a setup is shown in Fig. 24, where a centering tube is used at the barrel nozzle. The first specimen is accelerated in a barrel by a helium gun, while the other is secured in a Teflon centering ring. To prevent unwanted movement before impact, it is also glued in place. For a safe retrieval of samples after the test a fabric-filled container is incorporated at a distance of two meters from the barrel, allowing both samples to separate during flight to prevent secondary damages. To record the plastic deformation development a high-speed camera is used and the specimens are backlit to produce images capturing the shape of both. [47]

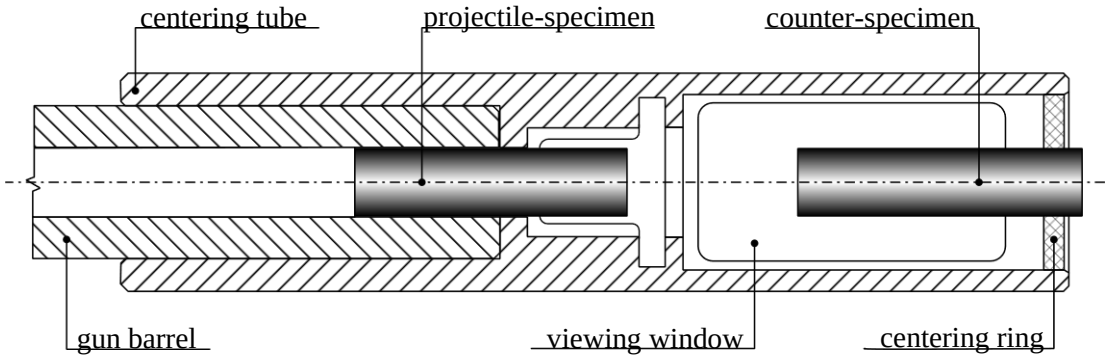

Fig. 24 Scheme of symmetric test setup [47].

An argument can be made, that implementation of a Teflon-centering ring may influence the outcomes, but the results have shown, that no damage to the rod surface was discovered. Furthermore, procedures utilizing Teflon have been developed and tested, with two types depending on material strength. Ring supports were used for material strength ranging from 400 – 800 MPa, while sabots designed to deform alongside specimens were used during symmetric testing of material with strengths greater than 800 MPa. [47; 48; 49]

A novel approach to symmetric testing was proposed by researchers at the University of Cambridge, where no sabots or centering rings are used. The apparatus aims to eliminate boundary condition changes caused by sabots by enabling sliding movement of the impacted sample, as shown in Fig. 25. Development of this device was affected by requirements, such as sufficient rigidity to hold the weight of the specimen and resist any movement caused by the airblast of the gun, while also deposing as little mechanical constraints as possible. A high-speed camera was used to monitor the impact and resulting deformation development, which was also taken into consideration during development. [50]

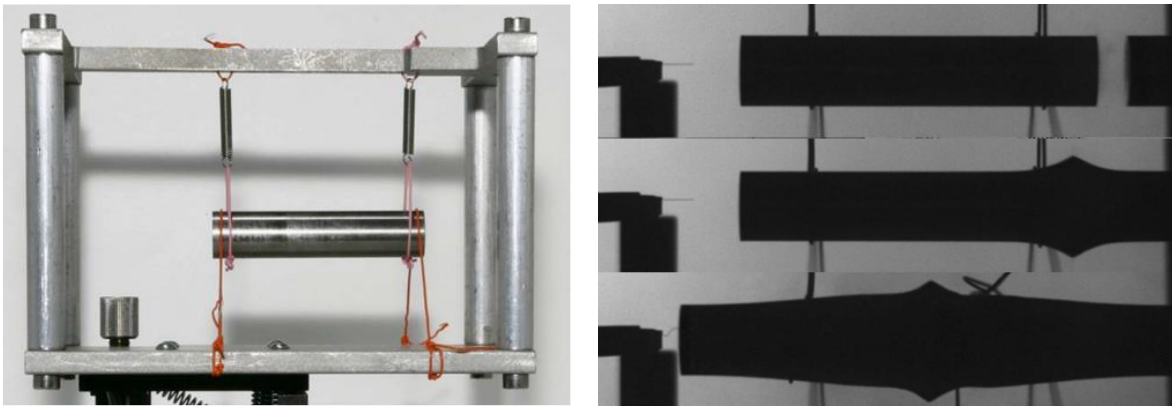

a) holding mechanism b) test results

Fig. 25 Wire cradle apparatus with test results [50].

The specimen is held in place by a set of spring-tensioned wires, which are coated by PTFE to lower their friction. To sufficiently align the sample, the whole mechanism is mounted on a set of adjustment stages allowing for movement in the X, Z, and pitch-yaw axis. To minimize the risk of misalignment during testing due to air blasts, the experiments were performed in a vacuum of around 40 mbar. The speed of the impacting rod was measured using a set of laser light gates, with one positioned near the impact face to also act as a trigger for the camera and other measuring devices, such as Photon Doppler Velocimetry to record the movement of the rear face of the impacted sample. A soft-catch tank was also incorporated, consisting of two layers, firstly about 40 cm of polystyrene balls followed by a layer of cloth at comparable depth. This prevented any unwanted secondary deformation of samples after an impact. [50]

Using a Digital image correlation – DIC, the process of deformation can be observed. A study conducted by Jannoti utilized a symmetric setup of TAT and specialized testing equipment to obtain time-resolved progress of the deformation. The tested material was copper at an impact velocity of 328 $m \cdot s^{-1}$. From the results shown in Fig. 26, it can be seen that the maximal strain rate is right at the impact face, while the maximum compressive strain just below the face was reported at 39%. [51]

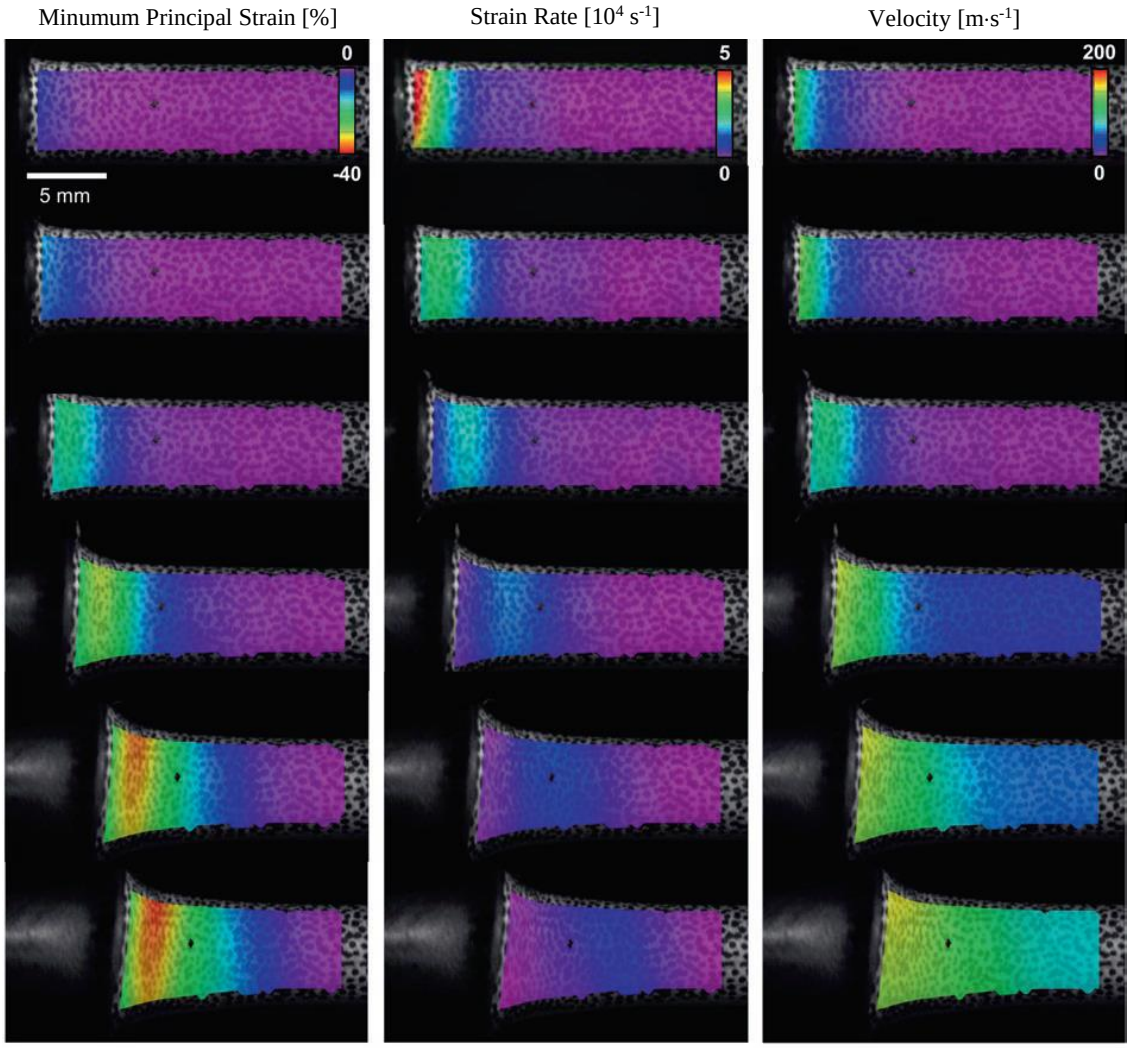

Fig. 26 DIC results of symmetric TAT [51].

2.5 Evaluation of the Taylor Test

Yield stress is an important property essential to understanding material behavior while outside forces are applied. Stress-strain curve, which is unique for any individual material, is used to graphically describe the yield behavior of said material, showing under what amount of stress the material behaves elastically, while the beginning point of plastic deformation development corresponds to a certain value, which is known as yield stress. This is dependent on the strain rate, increasing as the rate increases, therefore different values are recognized. Yield stress at low strains, which is derived from the quasistatic compression test, and the yield stress of material at higher strains. [34; 52; 53; 54]

At dynamic conditions of loading, the following factors influence the value of yield stress:

- Strain hardening – this material property is a byproduct of plastic deformation at lower temperatures. As the material is deformed, dislocations move and originate within the crystalline lattice, but the atoms themselves cannot rearrange due to low temperatures. This causes pinning and entanglement of dislocations, prohibiting their movement and thus stopping the plastic deformation. The material benefits from this by becoming harder and stronger without needing any other processes to occur. However, it hinders the material's formability and creates a need for higher loads of force to be applied to continue the plastic deformation. [53; 55; 56]
- Thermal softening – while a material undergoing a quasistatic deformation, a process that is generally considered isothermal, is capable of achieving an equilibrium of temperatures of itself and any medium surrounding it due to the extended period of deformation, material that undergoes TAT is subjected to extremely short times when it is being deformed. Such high rates cause an adiabatic increase in temperature, causing thermal softening, which can be observed as a decrease in the material's resistance to deformation. The increase in temperature can be seen in Fig. 27, most noticeable at the deformed end of the specimen. [57; 58; 41]

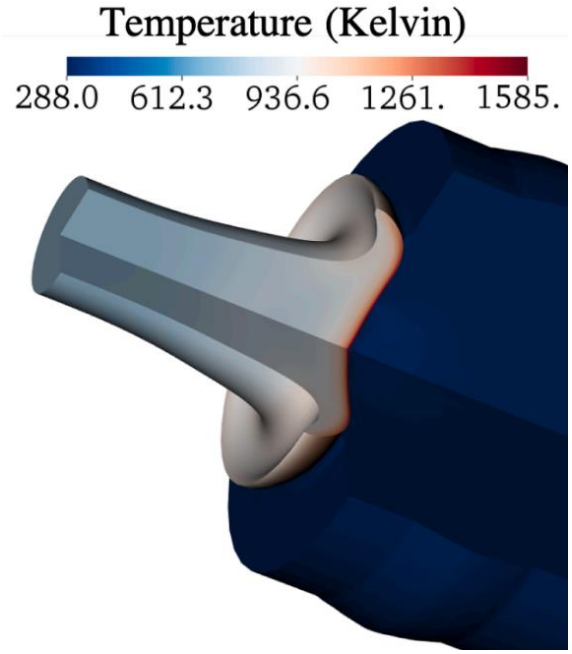

Fig. 27 Temperature increase during impact [41].

2.5.1 Yield stress - Taylor

Alongside offering his innovative test method, Taylor also proposed an analysis of yield stress estimation, which is based purely on dimensional measurements of the specimen pre and post-test, see Fig. 28. This analysis was possible with a few assumptions [33; 34; 59]:

- yield stress is the same throughout the specimen and does not change during impact,
- velocity of the elastic wave is much higher than the speed of impact and plastic front,
- the plastic front moves at a constant speed – material does not strain harden,
- deceleration of the rear of the specimen is constant.

Based on the assumptions, a general formula can be derived for dynamic yield stress evaluation, containing only the dimensions of the original and deformed specimen [33; 59]:

$$\sigma_{dy} = \frac{L - X}{2 \cdot (L - L_f) \cdot ln\left(\frac{L}{X}\right)} \cdot \rho v_0^2 \tag{2.1}$$

where: L – initial length of specimen [mm],
L_f – overall length of specimen after a test [mm],
X – length of undeformed portion [mm],
ρ – density of material [kg·m^{-3}],
v_0 – impact velocity [m·s^{-1}].

This formula is reliably applicable to tests, where impact velocities and consecutive deformations are significant. However, a correction proposed by Hutchings and O'Brien is imperative to be used when evaluating experiments, where a fraction L/L_1 nears the value of 1, pointing to slower impact velocities [61]:

$$\sigma_{dy} = 2 \cdot \sigma'_{dy} \cdot \left[\frac{1}{\left(1 - \frac{X}{L}\right)} - \frac{1}{ln\left(\frac{L}{X}\right)}\right] \tag{2.2}$$

where: σ'_{dy} – yield stress evaluated by (2.1) [Pa].

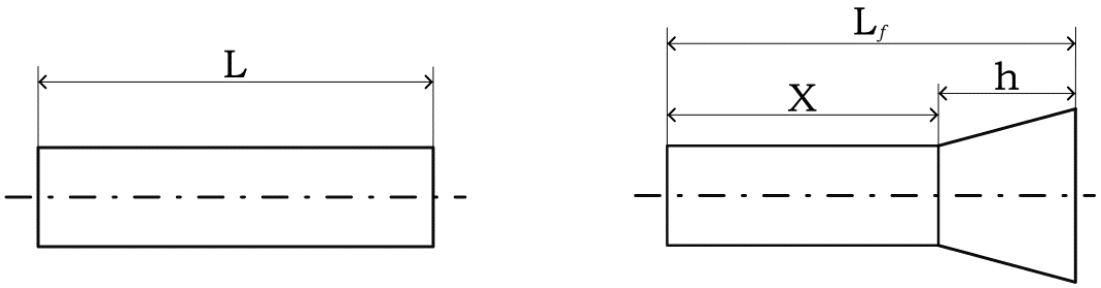

Fig. 28 Specimen scheme for yield stress evaluation by Taylor.

2.5.2 Yield stress – Wilkins and Guinan

Wilkins and Guinan conducted experiments intent on the deceleration of the projectile focusing on the ratio of its initial length **L** to the final length **L_f**, and diameter. The results based on experiments and calculations showed that this ratio was constant for a given impact velocity, meaning that the deceleration of a specimen was independent of its diameter, see Fig. 29. Testing at increased speeds showed deviation from expected results due to temperature increase upon impact. [62]

The rate of a sample length decrease was given by [62]:

$$\frac{dL}{dt} = -v_0 \tag{2.3}$$

where: dL – length change [mm],
dt – time change [s].

The deceleration of length, assuming a rigid body behavior, expressed as [62]:

$$\sigma_y = -\rho \cdot L \frac{dv_0}{dt} \tag{2.4}$$

where: dv_0 – impact speed change [m·s^{-1}].

Combining equations (2.3) and (2.4) gives an expression [62]:

$$\frac{L_f}{L} = exp\left(-\frac{\rho \cdot v_0^2}{2\sigma_y}\right) \tag{2.5}$$

Equation (2.5) states, that the ratio of material initial-to-final length is only influenced by two material properties – yield strength and density.

The yield strength of the material can be therefore expressed as:

$$\sigma_{dy} = (-\rho) \cdot v_0^2 \cdot \frac{1}{2 \cdot ln\left(\frac{L_f}{L}\right)} \tag{2.6}$$

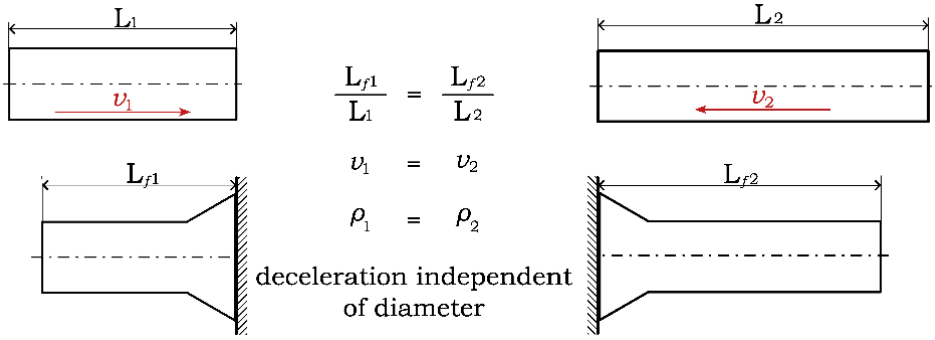

Fig. 29 Wilkins Giunan test principle and results [62].

2.6 Constitutive models

To effectively and correspondingly simulate a forming process, constitutive material models are used. Based on the number of necessary material parameters, that need to be determined experimentally, the simulated behavior of the material is closer to real-life scenarios. These include influences of strain rate or temperature. Among the most known formulas describing the relationship of stress-strain is the Ludwik-Hollomon formula [15; 63]:

$$\sigma_p = K \cdot \varphi^n \tag{2.7}$$

where: σ_p – true stress [MPa],
K – strength coefficient [-],
φ – induced strain [-],
n – strain hardening coefficient [-].

The strain rate sensitivity exponent is dependent on the type of material and homological temperature. It can be determined in two ways [12; 15; 64]:

A. By plotting the stress-strain curves of a selected material (see Fig. 30) at different strain-rates at a set strain. The exponent is then calculated as a fraction:

$$m = \frac{ln(\sigma_2/\sigma_1)}{ln(\dot{\varepsilon}_2/\dot{\varepsilon}_1)} \tag{2.8}$$

where: σ_1, σ_2 – flow stresses [MPa],
$\dot{\varepsilon}_1$, $\dot{\varepsilon}_2$ – strain rates [s^{-1}].

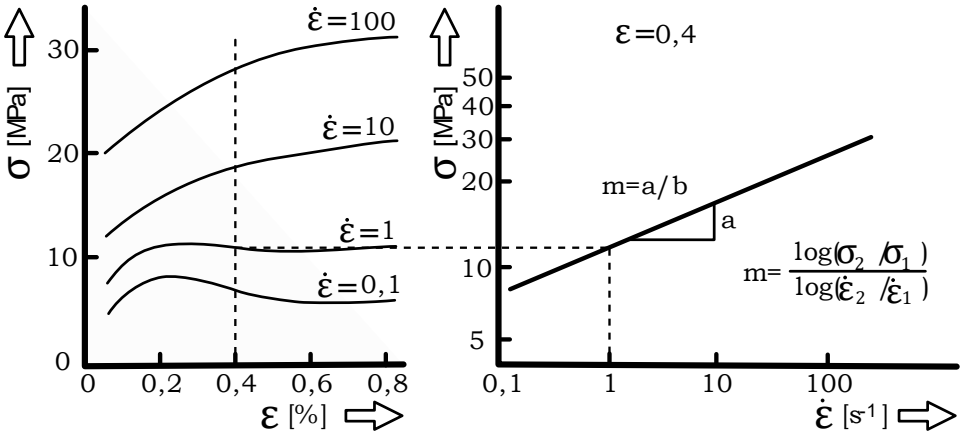

Fig. 30 Strain rate sensitivity determination [12].

B. By performing a strain rate jump test, where during the test a sudden change in strain rate is performed to obtain a characteristic curve. The strain rate can be either increased or decreased, resulting curve shown in Fig. 31. Calculation of the exponent is analogical.

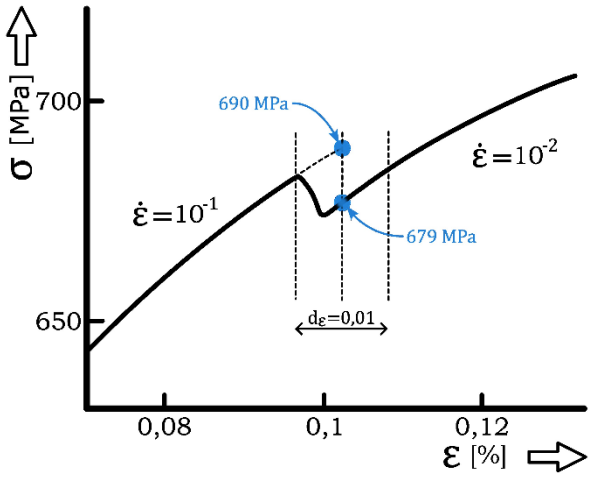

Fig. 31 Strain rate jump test [64].

2.6.1 Zerilli Armstrong model

This constitutive model proposes formulas for behavior description of materials undergoing dynamic loading incorporating changes in microstructure, in particular heat-activated dislocation movements. The model differentiates crystal systems of metals, body centered cubic – BCC, and face centered cubic – FCC. Differences have been observed, where FCC metals are less sensitive to strain rate and temperature than BCC metals. [13; 15; 65; 66; 67]

To evaluate the Zerilli Armstrong formula, the combined thermal portion of the stress parameter needs to be calculated, which is dependent on the dislocation activation area, subjected to their density, and Burgers vector [13; 66; 67]:

$$\sigma^* = \frac{M\Delta G_0}{Sb} e^{-\beta T} \tag{2.9}$$

where: M – Schmidt factor [-],
ΔG_0 – the height of the free energy barrier at 0°K [kJ·mol^{-1}],
S – dislocation activation area [b^2],
b – Burgers vector size [a],
β – deformation and strain-rate dependent parameter [-],
T – absolute temperature [K].

This leads to the evaluation of yield strength depending on the crystal systems. A bigger dependence on temperature and strain rate is known for body centered cubic metals. The equation for yield strength can be written as [13; 66; 67]:

$$\sigma = \sigma_0 + C_1 exp(-C_3 T + C_4 T ln\dot{\varphi}) + C_5 \varphi^n + k d^{-\frac{1}{2}} \tag{2.10}$$

where: σ_0 – static yield strength [MPa],
C_1 – relation of thermal and deformation rate effect constant [MPa],
C_3, C_4 – thermal activation effect constants [K^{-1}],
C_5 – preexponential factor [MPa],
n – work hardening exponent [-],
k – microstructural stress intensity [MPa·mm$^{1/2}$]
d – average grain diameter [mm].

While for face centered cubic metals the equation is [13; 66; 67]:

$$\sigma = \sigma_0 + C_2 \varphi^{\frac{1}{2}} epx(-C_3 T + C_4 T ln\dot{\varphi}) + k d^{-\frac{1}{2}} \tag{2.11}$$

where: C_2 – constant related to grain size [MPa].

The relations, as described by the authors, should be applied at the higher ranges of strain rates, and temperatures not exceeding half of the absolute melting point of the tested metal. For exceeding temperatures, diffusion and dynamic recovery processes within material need to be considered, while at extremely high strain rates a balancing factor of dislocation generation and deformation rate would fundamentally impact the proposed model. [13; 65; 67]

2.6.2 Johnson-Cook model

Is one of the most used material models applicable to a wide range of metals, owning this reputation to its empirical simplicity, while also incorporating the quasistatic behavior of the material, along with strain rate hardening and thermal softening effects. Due to its popularity and wide range of uses, the parameters integrated are known for a wide range of materials. Furthermore, based on this model, further equations have been developed for different types of materials, including ceramics. [13; 65; 66; 69; 70; 71]

The equation presented can be sectioned into three main parts impacting the evaluation of yield strength as follows [13; 65; 66; 69; 70; 71]:

- dependence on deformation,
- dependence on strain rate,
- dependence on temperature.

$$\sigma = (\sigma_0 + B \cdot \varphi^n) \cdot \left(1 + C \cdot ln\frac{\dot{\varphi}}{\dot{\varphi}_0}\right) \cdot \left(1 - T^{*m}\right) \tag{2.12}$$

where: B – work hardening coefficient [MPa],
C – strain rate sensitivity coefficient [-],
$\dot{\varphi}_0$ – reference strain rate [s^{-1}],
this value is user-defined and for simplicity is usually =1 s^{-1},
m – thermal softening coefficient [-],
T^* – homologous temperature constant [-],
the value lies in the range of $\langle 0; 1 \rangle$, defined as:

$$T^* = \frac{T - T_0}{T_m - T_0} \tag{2.13}$$

where: T – absolute temperature [K],
T_0 – room absolute temperature [K],
T_m – melting absolute temperature [K].

Johnson and Cook also present values of constitutive material constants for some materials, selection of some is presented in Tab. 2.

Tab. 2 Constitutive constants for selected materials [71].

Material	**Constitutive constants for (2.12)**				
	σ_0 [MPa]	B [MPa]	n [-]	C [-]	m [-]
OFHC Copper	90	292	0,31	0,025	1,09
1006 Steel	350	275	0,36	0,022	1,00
S-7 Tool Steel	1539	477	0,18	0,012	1,00

Modifications of the Johnson-Cook model further improve the applicability of the presented equation (2.12) providing results with a better correlation of empirically tested material and mathematically evaluated outcomes, some of which include:

- Andrade et al. – suitable for experiments under increased temperatures incorporating dynamic recrystallization and phase change of material in the form of function **H(T)**. The modified expression of the model is: [13; 72]

$$\sigma = (\sigma_0 + B\varphi^n) \cdot \left(1 + C \cdot ln\frac{\dot{\varphi}}{\dot{\varphi}_0}\right) \cdot \left(1 - T^{*m}\right) \cdot H(T) \tag{2.14}$$

where: $H(T)$ – reducer function, defined as:

$$H(T) = \frac{1}{1 - \left[1 - \frac{\sigma_{rec}}{\sigma_{def}}\right] \cdot u(T)} \tag{2.15}$$

where: σ_{rec} – flow stress after recrystallization [MPa],
σ_{def} – flow stress prior to recrystallization [MPa],
$u(T)$ – step function of temperature,

$$u(T) = \begin{cases} 0 & for\ T < T_c \\ 1 & for\ T > T_c \end{cases} \tag{2.16}$$

where: T_c – temperature of critical phenomenon [K].

- Follansbee et al. – which includes a simple modification, aimed at material strength and strain-rate dependence, that better represents the effect of strain rate on the material. While equation (2.12) presents a linear progression, this variation uses exponential progression. [65; 73]

$$\sigma = (\sigma_0 + B\varphi^n) \cdot \left(\frac{\dot{\varphi}}{\dot{\varphi}_0}\right)^C \cdot \left(1 - T^{*m}\right) \tag{2.17}$$

To evaluate the results of this thesis and as a constitutional model for simulation generation, the Johnson-Cook model in its original form (2.12) will be used, due to its simplicity and wide range of applicable scenarios.

2.7 Application of simulation software

For detailed simulations, or the creation of studies for complex assemblies including many different materials, using specialized software for simulation is beneficial. Nowadays, most of the commercially available programs utilize the Finite Element Method, which is based on discretization, in other words, the simplification of a complex continuum into a set – finite number of elements that closely represent the solved problem. [15; 74; 75; 76]

To efficiently and correctly solve a problem, it is important to choose the correct method of time integration, which can be:

- Implicit integration – is ideally used when the influence of boundary conditions is gradual and the impact of strain rate is minimal. This method allows for the analysis of geometry after the increment of stress as a function of strain is established. Global equilibrium is established in each time increment and solving of unknown variables in the time of $\mathbf{t_{n+1}}$ is done through the method of forward differences. This allows for the selection of a greater time step, however, if the step is incorrectly selected, the results of the simulation may be inaccurate. [74; 76; 77]
- Explicit integration – is suitable for problems, where strain rates exceed quasistatic conditions. In this method, values of calculated variables at each point of mesh at a set time increment are used for the calculation of value in the next time increment. Those increments need to be small enough for kinematic conditions, and accelerations, to be nearly constant during an increment. [77; 78]

An overall comparison of methods for time integration is presented in Tab. 3.

Tab. 3 Time integration methods properties [32].

Method of time integration	Explicit	Implicit
Applicable area	Highly dynamic problems with non-linear behavior	Static and quasistatic problems
Software character	Simple code running within internal storage	More complicated, utilizing external storage
Matrix inversion	No	Yes
Equilibrial iterations within the time step	No	Yes
Kinematics	Small rotations	Big rotations
Memory requirements	Small	Bigger

3 DEVELOPMENT AND TESTING

The practical part of the thesis describes and expands individual stages of development of the testing apparatus, as well as subsequent tests performed. First, the initial design and principle of the proposed testing method are described, followed by material choices and the construction of the main parts, and decision-making regarding other necessary accessories required, leading to the initial testing of the prototype. Based on the results, further improvements and their implementation are described. Next, a material is selected to be tested and compared to the conventional Taylor Anvil Test method, while also providing results of the testing and evaluation of required variables on the new apparatus. At last, a comparison of simulation results and real-life results is provided.

3.1 Initial design

The new apparatus is based on the principle of a Taylor Anvil Test device that is already in use, which consists of a single barrel, where the specimen is loaded through a chamber, that is connected to a compressor with an air tank. At the other end, a rigid rod is used as an impact surface, which is connected to measuring devices evaluating the test. The newly developed apparatus is intended to make use of a symmetric impact of the test specimens in an impact chamber. The design is based on the initial plans shown in Fig. 32.

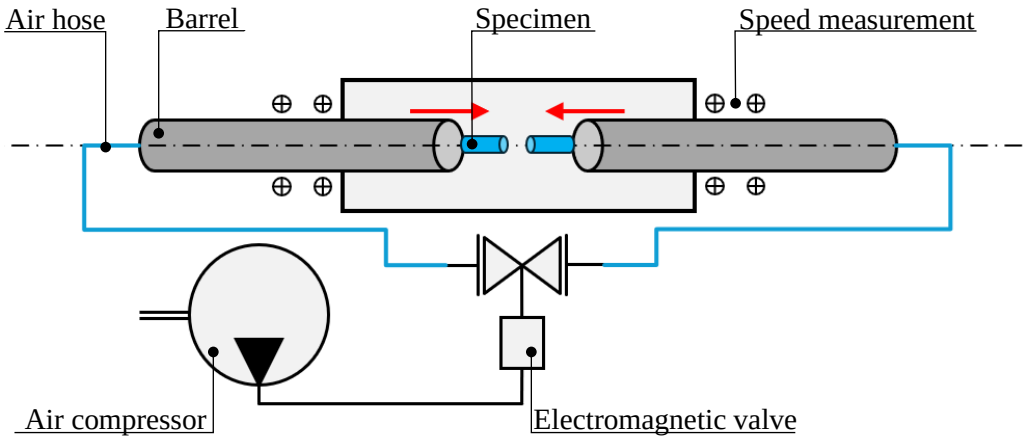

Fig. 32 Initial scheme of testing apparatus.

The apparatus consists of an air compressor with an air tank that provides a way of propulsion in the system. It is connected to an electromagnetic valve. The valve is electronically operated and a timing switch is incorporated into the system to allow for a set time period to be selected to open the valve, as only a fraction of the compressed air from the reservoir needs to be released. The air is distributed via air hoses of the same length, connected to the main two barrels. At the starting ends of these, the specimen will be loaded in before the test, while the other ends will be placed in an enclosed metal impact box, that will be designed to provide sufficient protection during the test and with enough venting holes for the compressed air to dissipate. The impact box will also incorporate an observation opening through which the impact of the specimens can be safely recorded using a high-speed camera. A speed-measuring device will be developed to provide an exact value of the velocity of the specimens during the test and will be affixed to the ends of the barrels. The whole apparatus will be placed on an aluminum extrusion profile, that will serve as the main load-bearing surface, providing a straight surface for the test. A supporting frame will be manufactured for the main extruded profile, utilizing smaller extrusion profiles.

3.2 Manufacturing the apparatus

As per the initial design, most of the testing equipment is placed on an aluminum extrusion profile, which was selected from a catalog of construction profiles of the RK-Rose-Krieger company. The length was limited by the size of the laboratory room where the device would be placed, which was roughly 8 meters long, thus the length of the profile was chosen to be 4,7 meters, which is also within the maximal length offered by the supplier. Tab. 4 describes the selected profile and shows the material properties, as stated by the supplier.

Tab. 4 Material data of selected profile [79].

Size [mm]	60 x 120 x 4700
Material	EN AW 6063 T66
Tensile strength [Nmm^{-2}]	245
0.2% - yield strength [Nmm^{-2}]	200
Modulus of elasticity [Nmm^{-2}]	70 000

For the device to be easily maintainable and usable, the profile needed to be placed on a supporting frame. The number of supports and their placement is based on deflection calculations for the main profile based on the load applied. Deflection can be calculated according to [79]:

$$f = \frac{F \cdot L^3}{E \cdot I \cdot 48 \cdot 10^4} \tag{3.1}$$

where: F – applied load [N],
L – free length [mm],
E – modulus of elasticity [N·mm^{-2}],
I – geometric moment of inertia of the profile [cm^4],
for selected profile $I = 94{,}7\ cm^4$.

The amount of load was set according to the expected estimated weight of the impact chamber. The reasoning behind this decision is that compared to the rest of the equipment, the chamber was expected to weigh the most, while also being placed in the middle of the device. The estimated weight was 10 kilograms. Two options were investigated:

A. Two supports – one placed at each end, see Fig. 33. Deflection for this configuration was evaluated according to (3.1) as:

$$f_A = \frac{98{,}1 \cdot 4700^3}{70000 \cdot 94{,}7 \cdot 48 \cdot 10^4} = 3{,}20\ mm$$

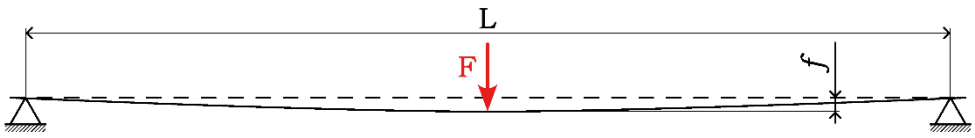

Fig. 33 Schematic depiction of option A.

This option was unsuitable for this case due to the amount of deflection, furthermore, the overall stability of the support frame would be inadequate.

B. Four supports – expanding option A by adding 2 more supports closer to the center of the main profile (see Fig. 34) to improve deflection. Their distance was chosen to be 700 mm apart. The deflection was evaluated by (3.1) to the amount of $f_B = 0{,}01$ mm.

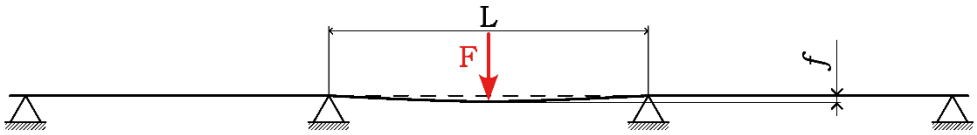

Fig. 34 Schematic depiction of option B.

This option was selected based on the low deflection of the main profile in the center, while also being more stable overall.

Repurposed aluminum profiles of various lengths were chosen to be the material for the support frame. Selected pieces had a square cross-section with a 40 mm side length. They were cut to the required lengths on a band saw RPPK-115UH, see Fig. 35. This band saw is designed to cut commonly used materials, including aluminum, while providing the ability to adjust the cutting speed by a hydraulic piston controlling the falling speed [80].

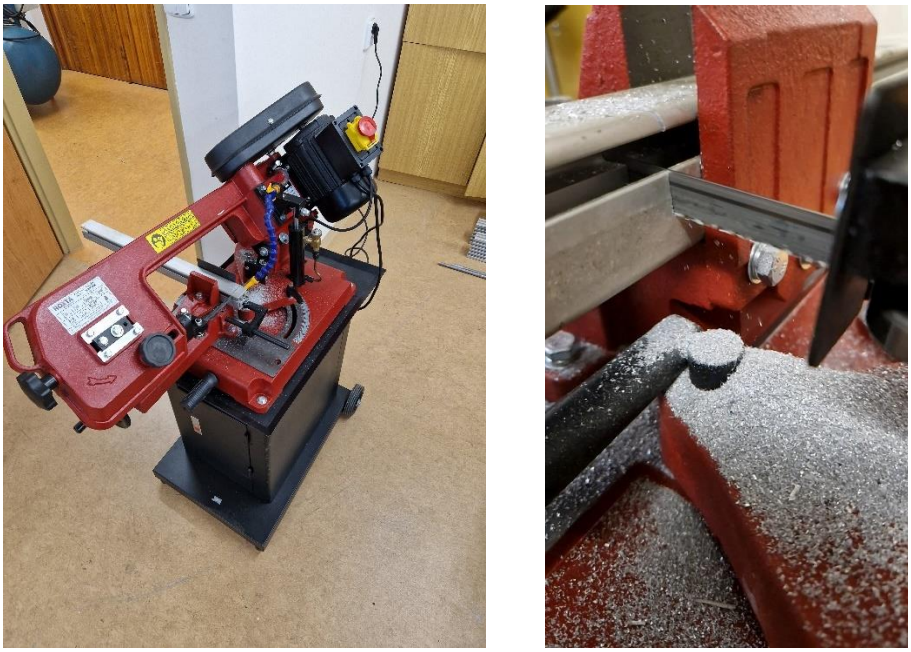

Fig. 35 Cutting aluminum profiles for support frame.

3.2.1 Assembly of the support frame

After the profiles were cut to the required lengths, there was a need to find a way for their interconnection to be structurally sufficient to support the rest of the testing equipment. Assembly fixtures available from the supplier were taken into consideration, however, the amount in stock at the time was insufficient, furthermore, their price for low amounts was inadequate. As a solution, a similar fixture was designed to be made using additive technologies of 3D printing. The shape and the way of presumed assembling is depicted in Fig. 36a, where the designed part is colored green. However, after mounting the fixtures to the profiles, it was discovered that their strength was insufficient. Some of them started to crack upon fastening the bolts, and others broke apart along the layer lines, as can be seen in Fig. 36b.

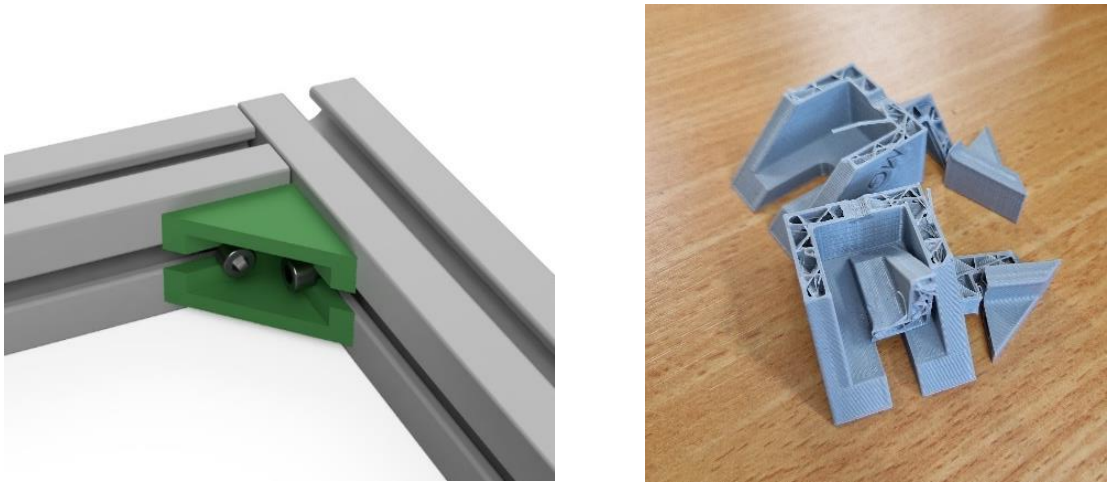

a) presumed assembling b) failed printed fixtures

Fig. 36 Assembly fixtures.

To provide sufficient stability for the supporting frame, another fixture was designed. Additionally, a decision was made to change the manufacturing method to make the parts sturdier, as well as changing the material. The new fixtures, depicted in Fig. 37a, are made out of a 5 mm thick steel sheet blank cut using plasma.

Another issue encountered was an uneven floor in the laboratory. To resolve the problem a simple system of leveling feet was designed, which allowed individual adjustments in height at all points of the support frame touching ground. This also allowed the frame to be leveled in all axes. As shown in Fig. 37b, it consists of an M8x50 screw with a hexagonal head that screws into the central hole of the profiles, while at the other end, a 3D-printed boot protects the floor from scratches.

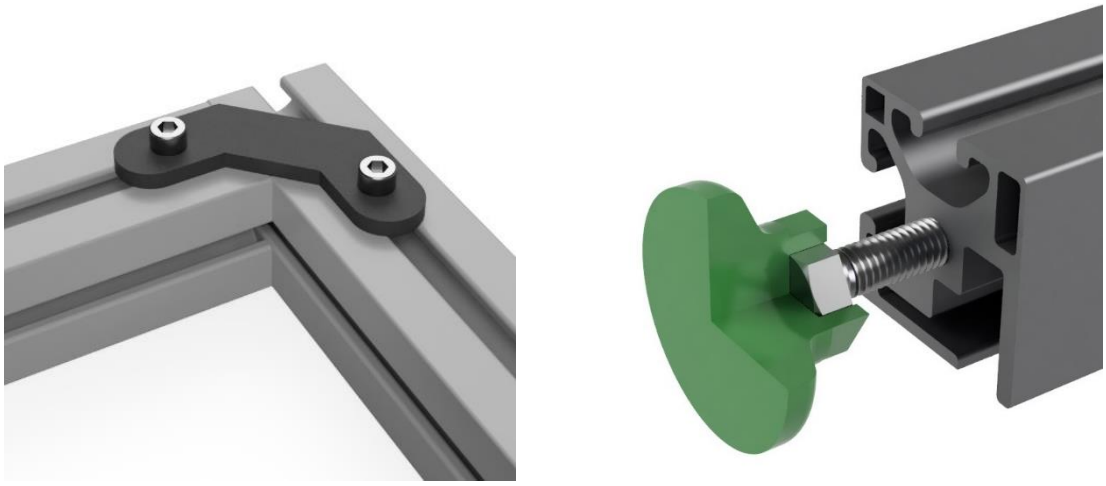

a) steel fixture

b) adjustable feet

Fig. 37 Support frame accessories.

In order to further improve the rigidity of the supports a smaller L-shaped profile was affixed to both ends at a height of 150 mm from the bottom, which prevented any unwanted movement of supports. Furthermore, each two supports were connected by another two square profiles. All connections can be seen in Fig. 38, where the overall shape of one section of the supporting frame is shown, with close-up renderings of all connections mentioned.

Next, the main profile was mounted to the support frame sections. A set of holes was drilled in the upper profiles of the frame for mounting. Implementing additional fixtures for rigidity was

discussed, but after the main profile was mounted, they were deemed unnecessary. Note that Fig. 38 shows only half of the apparatus due to its length and that two main profiles are mounted to the supporting frame. This decision was made during assembly to allow for a second apparatus to be manufactured and placed on the existing frame.

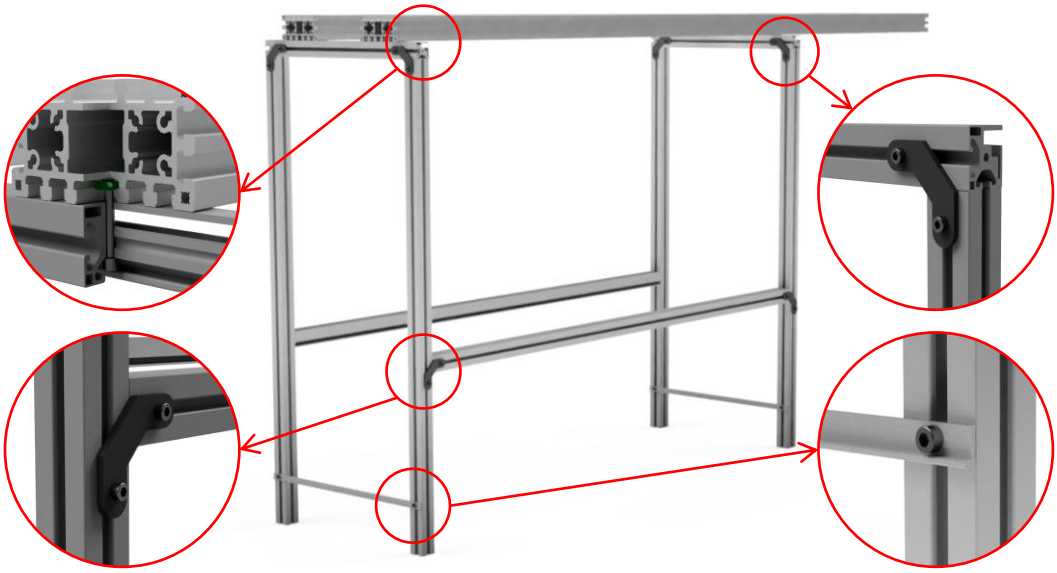

Fig. 38 Assembly of support frame and main profile.

3.2.2 Barrels and holders

For the development of the holders, a material for barrels needed to be selected first. This was based on the specimen carriages that are used by the already-in-use Taylor test. PVC tubing of 25 mm outer diameter was selected due to its ease of use and availability, while also enabling the usage of carriages.

To symmetrically distribute the air in the system, the initial design changed to accommodate a set of two PVC tubes on each end. One pair served for air distribution, the other as firing barrels. The air distribution pair was connected by a “T-joint”, to which air was delivered through a valve. The scheme of this system is shown in Fig. 39.

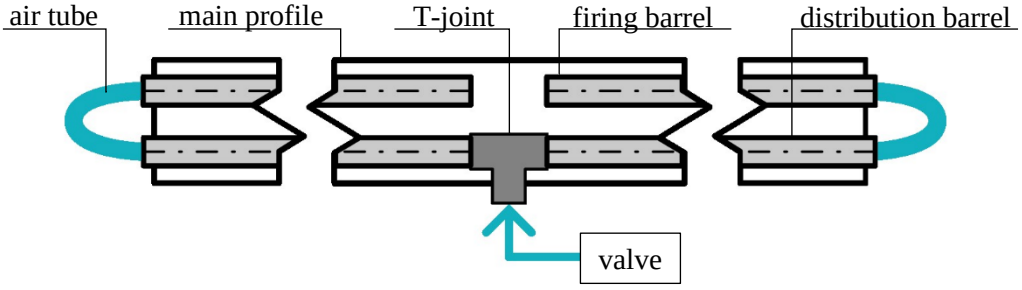

Fig. 39 Improvement of design.

According to the improved design, barrel holders needed to securely hold two PVC tubes with an outer diameter of 25 mm. The designed holders consist of three parts:

- Bottom part – secured to the main profiles slots by M6x30 screws and stones,
- Top part – tightened by M6x35 screw and M6 nut held at the underside of the bottom part, which secures the barrels,
- Spacer – serves for final fine height adjustment of the holders.

The holders were 3D printed using PLA filament. This saved time and enabled design changes to be implemented more easily. A total amount of 10 holders was made, therefore 5 holders were placed on each side of the apparatus with a spacing of 500 mm between. Fig. 40 shows cross-section of the holders and how they are mounted to the main frame.

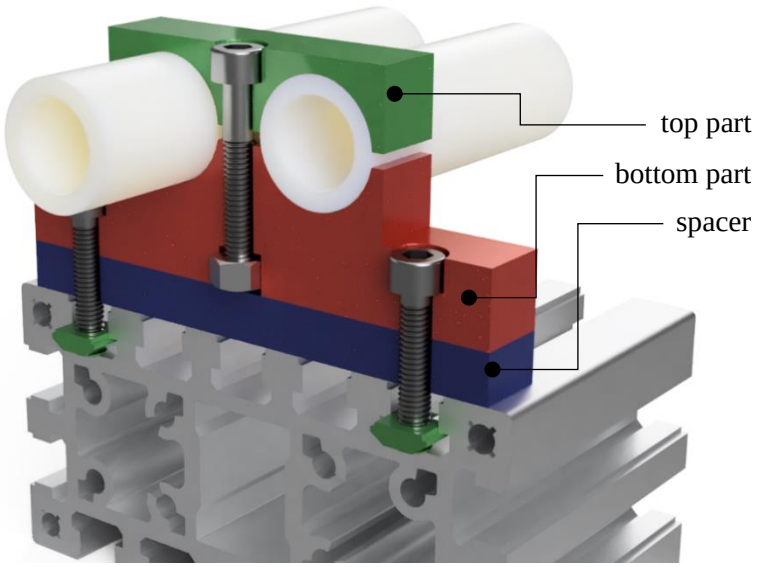

Fig. 40 Barrel holder mounted to the main frame.

Next, the tubes were cut to appropriate lengths using tube cutters. Firing barrels and distribution tubes length was chosen at 2350 mm and 2300 mm respectively. To connect the air distribution tubing together by a "T-joint" and to be able to connect air hoses to the ends of the firing barrels, threaded fittings needed to be added. All the pieces were connected using poly-fusion welding. The welder used is shown in Fig. 41. Welding parameters were selected according to the user manual, their overview is in Tab. 5. In the case of the firing barrels, precise adjustments needed to be made for proper alignment of the fitting and the tube.

Fig. 41 Poly-fusion welder Polys P-4 650W.

Tab. 5 Welding parameters.

Diameter	[mm]	25
Temperature	[°C]	240
Heating time	[s]	7
Depth of melting	[mm]	16
Setting time	[s]	5

3.2.3 Impact chamber and valve

For the protection of personnel during material testing, an impact chamber needed to be implemented into the apparatus. It was designed to provide sufficient cover during firing, with enough ventilation openings. The panels were plasma-cut out of a 10 mm thick steel sheet and afterward welded together into the final form. The top panel was welded to the rest of the box by hinges to allow its opening. Four mounting holes were cut in the bottom panel for mounting. The front panel incorporates an opening, which can be used as a viewport for a high-speed camera. After welding, all surfaces were sand-blasted, as can be seen in Fig. 42. The impact box was mounted into the middle of the main profile.

Fig. 42 Sand-blasted impact box.

To control the airflow from the air compressor, a solenoid valve VZWM-L-M22C-G34-F4 made by Festo was selected, based on fast open/close switching times, stated at 15 and 12 ms respectively by the producer. To control the time during which the valve is open an electrical timing switch Selec 600XU was also incorporated. This switch has multiple time functions and variable period settings, which allows for the selection of open/close time to be as little as 0,1 seconds. Both devices are shown in Fig. 43. Power to this system is delivered by a variable voltage supply set to 24V, which is the nominal operational voltage of the valve. Both devices were connected according to user manuals. [81; 82]

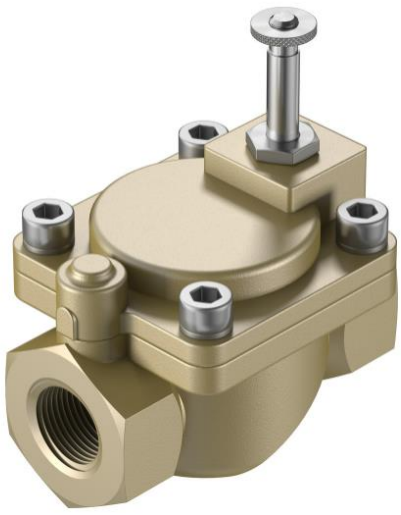

a) solenoid valve [81]

b) timing switch [82]

Fig. 43 Air-flow valve and timing switch.

3.2.4 Specimen loading

To enable a quick way of specimen loading into the apparatus, a metallic “T-joint” was attached to the ends of the firing barrels, see Fig. 44. Thanks to this addition, the air hose connecting the distribution tube and firing barrel did not have to be removed every time a specimen was to be loaded. The hose was connected to the bottom opening of the joint, while a cap prevented the air from escaping during testing.

Fig. 44 “T-joint” for loading.

This solution however had some complications. As the inner diameters of all the parts were different, as can be seen in the cross-section rendering in Fig. 45, loading the specimen proved to be complicated, as it sometimes got stuck on one of the edges and other times the specimen fell down into the air inlet.

Fig. 45 Firing barrel connections.

To circumvent this issue a simple loading tool was designed and 3D printed. To load the specimen, it is first inserted into this tool, which is next pushed into the “T-joint” up to the last edge. Then, the specimen is pushed out of the tool into position at a set distance in the firing barrel, as can be seen in Fig. 46.

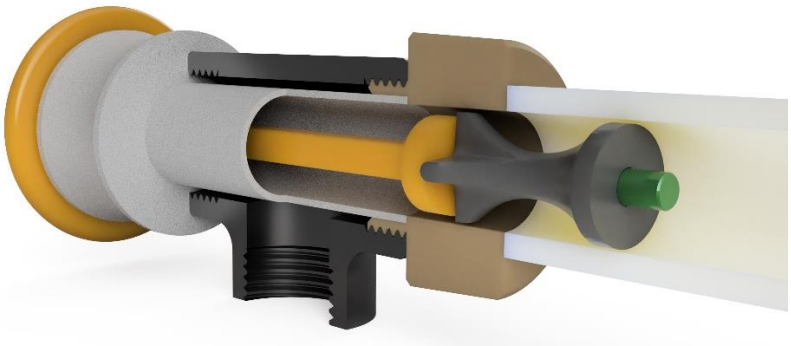

Fig. 46 Specimen loaded using insertion tool.

3.3 Initial testing and results

After a complete assembly of the apparatus, initial tests were performed. Firstly, all connections were checked for air leaks after connecting the compressor to the solenoid valve. Next, the timing switch capabilities were tested alongside the functionality of the valve by performing two blank tests, meaning no specimen was loaded. These tests were successful and all devices worked as expected, therefore, the next phase of testing was initiated.

In the next step, a randomly selected material was used to test the capability of the device. Aluminum samples were used, however, the exact material properties and the material categorical name are unspecified, as this was meant to serve only for experimentation.

All the samples had the same dimensions, a diameter of 5 mm, and 25 mm in length. They were inserted into the 3D-printed carriages and loaded into the firing barrels using the insertion tool. Next, the compressor was pressurized to 6 bar. The timing switch was set to impulse load mode. In this mode, the device works as a timer, allowing the user to select a time duration, upon which the switch closes the circuit, thus opening the valve, for a duration of 0,5 seconds. For safety reasons, two minutes were selected as the duration, which allowed everyone present during testing to exit the laboratory into a hall.

After firing, the power source for valves was switched off to prevent misfires. Next, the samples were retrieved and analyzed. A total amount of four tests were conducted during the initial testing, resulting in the following observations of the device's capabilities and problems:

- Structural problems – after the testing, the holders of the barrels were found to be cracked and bent. While this problem might have been present before the testing, after the device was under load, the problems became apparent.
- Fig. 47 shows a photo of one of the problematic holders. What needs to be noted is the crack in the bottom part, which is a result of tightening the top part of the holder, which pushed the barrels outwards. This created a sideways load on the walls of the bottom holder. It is apparent that the cracks propagate along the layer lines of the 3D printed part, where this phenomenon of parts being "weaker" in the direction perpendicular to layers is well known. Another problem can also be seen on the top holder, where overtightening caused the part to bend. Out of the ten holders installed, three had beginning cracks and four holders had fully cracked.

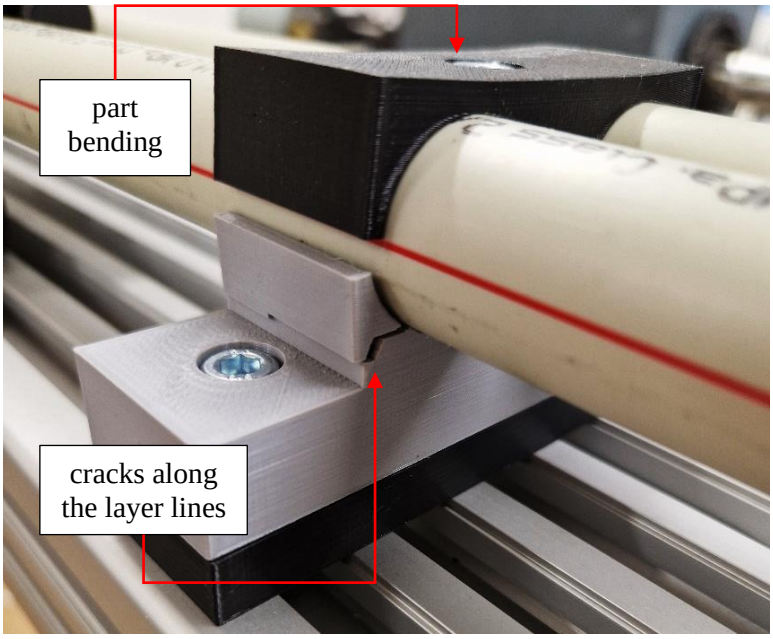

Fig. 47 Structural problems of barrel holders.

- Pressure loss – implementation of air distribution tubing to achieve symmetrical fire led to an increase in the volume of unpressurized areas. As the pressurized air was released by the valve, it first had to "travel" to the firing barrels. This caused a significant pressure decrease in the system, resulting in unsatisfactory deformation of the tested material. In Fig. 48 one of the tested samples is shown. The expected deformed part of the specimen is not visible to the eye, although when measured by micrometer the impacted face has shown an increase in diameter, from the original 5 mm to 5,05 mm. Similar results were found on all other tested samples. These results were not up to expectations.

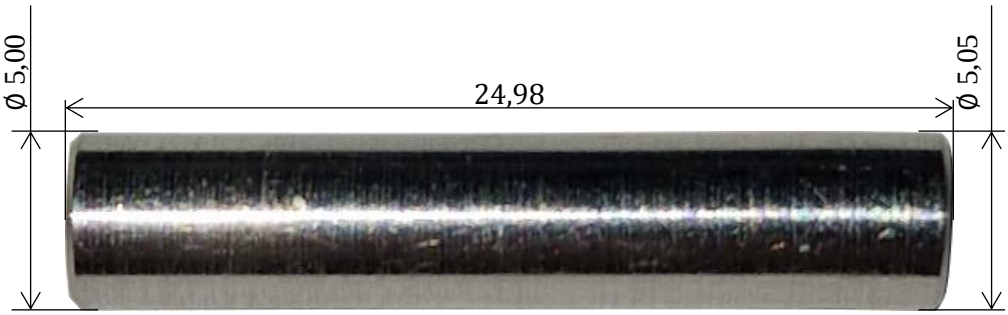

Fig. 48 Example of a tested specimen.

- Concentricity – was one of the main goals of this device development, however, none of the tested samples achieved a perfectly concentric impact of the faces. After the first test, an improvement was attempted by adding another set of barrel holders into the impact box itself, secured via holes meant to secure the box. This addition showed a slight increase in concentricity of the impact, but ideal conditions still were not satisfied. Fig. 49 shows a close-up shot of the impact face of one specimen. The ridge created by the impact of the second specimen onto this face was used as a reference to estimate the shift of the axis, which was determined to be in the range of 1,2 – 1,3 mm.

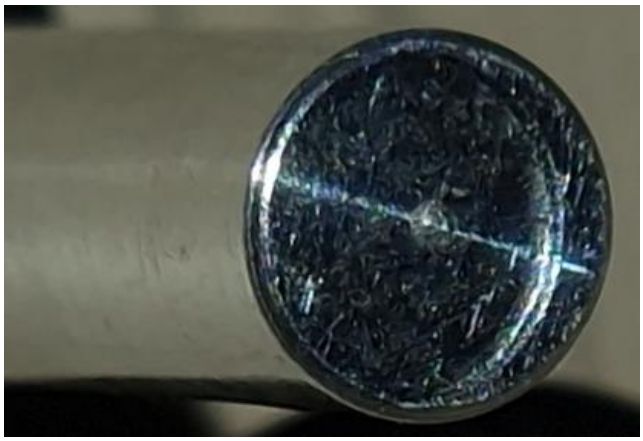

Fig. 49 Impacted face of a specimen.

- Symmetrical impact – throughout all tests, both specimens always remained in the impact chamber, which implies that they always impacted perfectly in the middle of the apparatus, as expected.

Based on the results and observations of the initial testing, improvements, and changes were implemented into the design of the apparatus. These will be covered in the next chapter of the thesis.

3.4 Improvements and their results

Based on results from initial tests, improvements were made to the testing apparatus to improve encountered issues, which have been described. The main goals were to lower the pressure loss during firing and to improve the concentricity of the impact. The following changes were made:

- Reconfiguration – improving the layout of the device to minimize pressure decrease. To do so, the air distribution tubes were shortened and moved to the underside of the main profile. Additionally, another solenoid valve was added, and now the two valves, both still electronically controlled via the timing switch, were positioned at the ends of the air distribution tubes, leaving a much less unpressurized area before the specimen. A schematic depiction of the reconfigured layout is shown in Fig. 50.

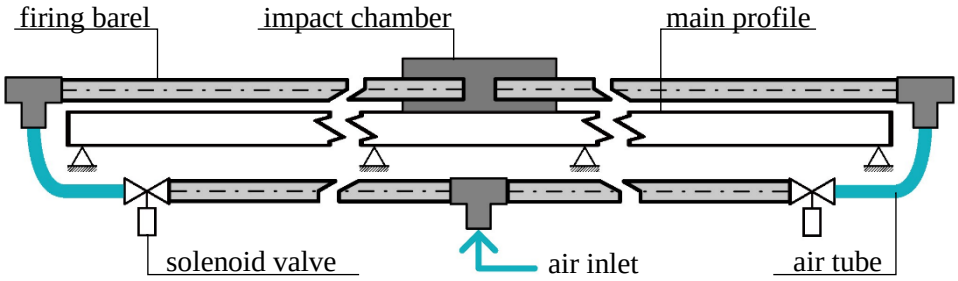

Fig. 50 Reconfigured layout.

- Barrel holders – outside changes of the device configuration, which now required only a single barrel to be held, development of the new holders also needed to address their structural rigidity. 3D printing was still used for their production, however, their shape and functionality have been updated, keeping in mind the direction, in which they will be printed. While the original holders relied on tightening of the central bolt to secure the barrel, updated ones do not. Their design incorporates a compliant mechanism, which is meant to be elastically bent to provide sufficient pressure on the barrel to secure it. Furthermore, a “clip” style latch is used to allow for a fast and easy release of the holder, which does not require any screw loosening. For easier release, a tab is printed on the outside of the clip. The holder in an open state is shown in Fig. 51. Thanks to the changes mentioned, any bending of parts due to overtightening now cannot occur.

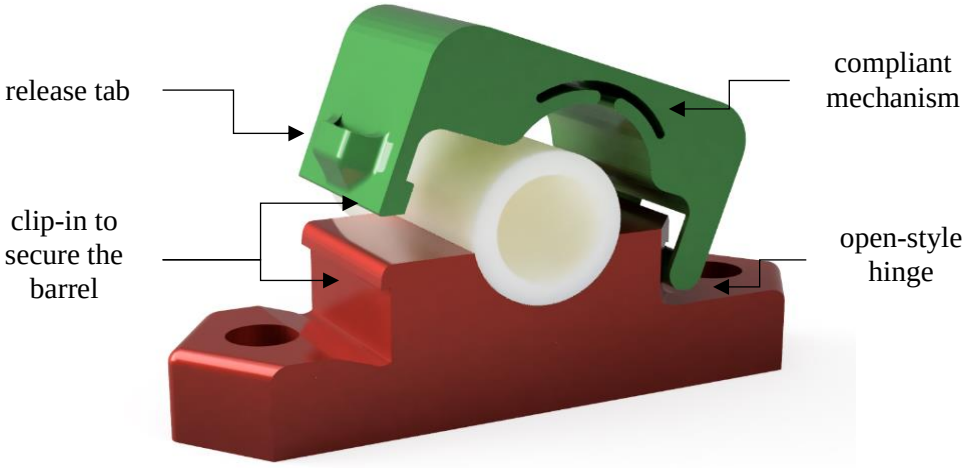

Fig. 51 Updated barrel holders.

All the changes were made in a way that allows both parts of the holder to be printed "lying down". Fig. 52 shows a comparison of print orientation for the original and new holder, where layer lines can be seen. A different way of printing provides the new holder with increased structural rigidity of both top and bottom parts, as the layer lines no longer create areas prone to breaking.

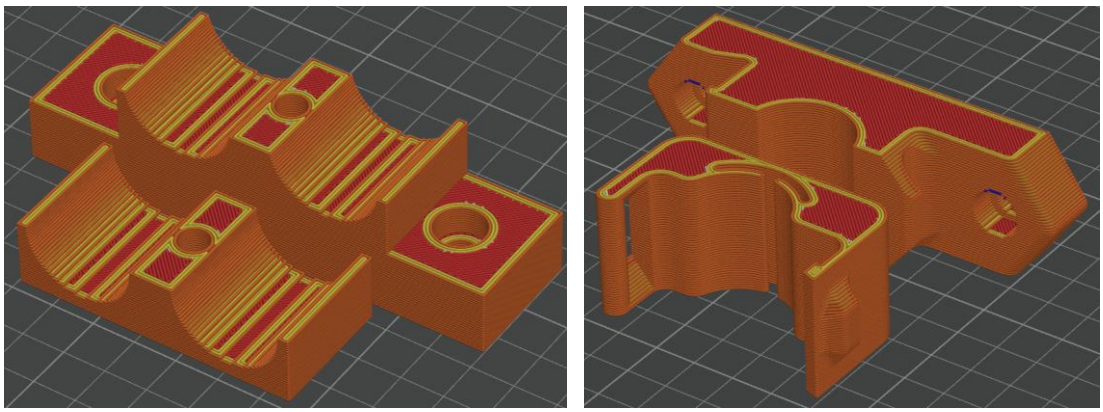

a) original holder b) new holder

Fig. 52 Print orientation.

- Carriage size – was found to also impact the concentricity of an impact. The carriages used for the classical Taylor test device, which were being reused, have bigger allowances on the diameter for easier insertion. While the inner barrel diameter is 17,6 mm, the outer diameter of the carriage is only 16,5 mm. This can, in extreme conditions when the carriages are positioned at the opposing edges, cause misalignment of the specimen axis by 1,1 mm, as is evident from Fig. 53. For this reason, the outer diameter of the carriages has been increased to 17,5 mm. Although an increase to 17,6 mm would be ideal, the inner diameter of the barrel and its roundness are not constant, which could possibly lead to jamming of the carriage.

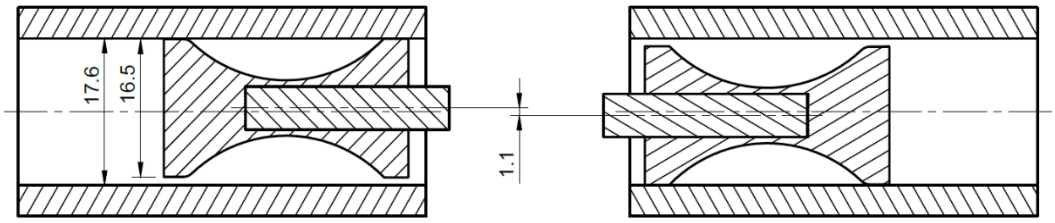

Fig. 53 Misalignment due to carriage size.

- Centering tube – was added to further increase the alignment of the firing barrel muzzles. As the misalignment of the axis from the initial testing specimen was estimated to be more than 1,1 mm, it was evident that the muzzles were not perfectly aligned. The tube has enough venting holes to allow air pushed by the specimen carriages to escape. It is fitted onto the ends of both barrels, as can be seen in Fig. 54. This means that due to size constraints of the impact box, one of the barrels needs to be released from the holders and moved back slightly to allow for specimen retrieval after every test.

- Tubing – previously used flexible metal hoses restricted airflow due to smaller inner diameter. For the updated design a heavy-duty garden hoses were therefore used, which are less restrictive. Although these hoses are not meant to be used with compressed air, in the proposed configuration they only serve as a connection between the valve and the inlet of the firing barrels, therefore the compressed air does not cause their swelling due

to pressure, as it only travels through for a short period of time. Their implementation can be seen in Fig. 55, which shows one end of the apparatus.

Fig. 54 Centering tube.

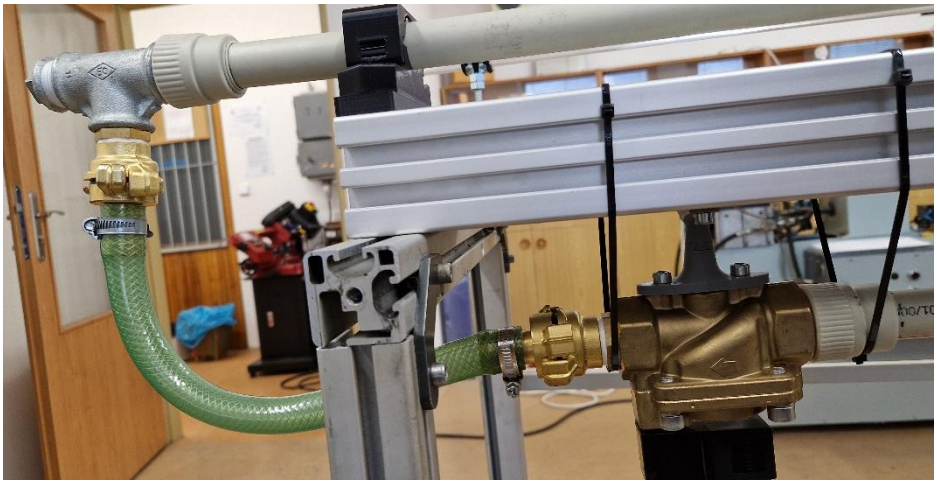

Fig. 55 One end of the connected air distribution.

After implementing all the mentioned improvements, the device was tested again. Tested samples were of the same material used during the initial testing. Results have shown a significant improvement, both in achieved concentricity of the impact and in the plastic deformation developed. Fig. 56 shows a selected deformed specimen, the diameter of the impacted face increased from the original 5 mm to 5,43 mm, while the concentricity of faces is within 0,1 mm. These results were deemed satisfactory and testing of selected material could begin.

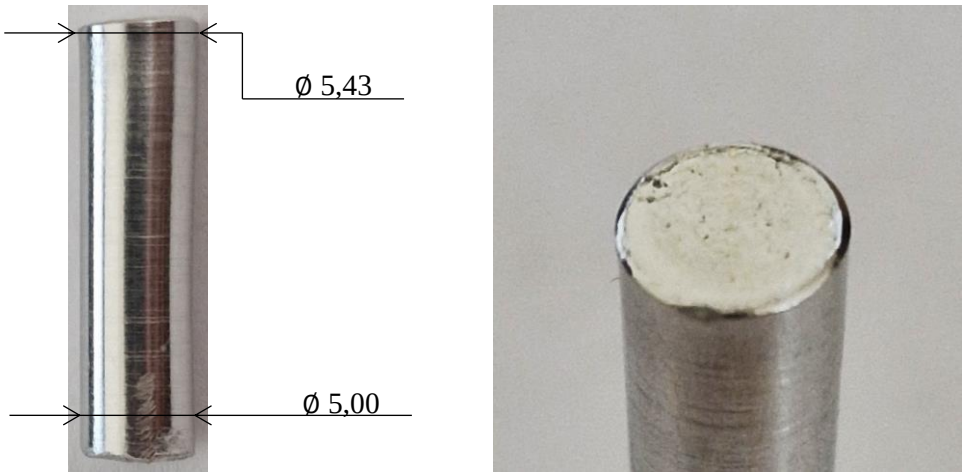

Fig. 56 Impacted specimen after improvements.

3.5 Speed measurement development

The speed of the specimen is one of the most important variables necessary for a correct evaluation of the experiment, as it correlates with the amount of kinetic energy entered into the system during a test.

A light-gate system was developed for the testing apparatus. There can either be one beam, where, as an object of a known length travels through, the time length of intersection is recorded, or two beams, where the time between two crossings is recorded. This provides enough information for speed calculation. Both principles are shown in Fig. 57.

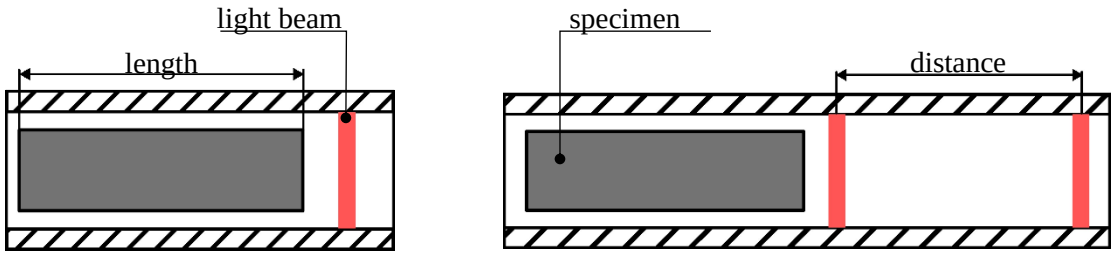

a) single beam b) dual beam

Fig. 57 Principle of speed measurement using light-gate.

The dual beam approach was selected, due to concerns regarding carriage shape, which could influence the measurement if a single beam had been used. Furthermore, the measurement of speed will only be implemented on one of the firing barrels, since during testing all sample impacts occurred in the middle of the device, therefore it can be estimated that their speed was the same.

The hardware used consisted of a microcontroller Raspberry Pi Pico H for operation and processing. Light beams were produced by two Keyes KY-008 5V laser modules with 650nm wavelength and two Broadcom HFBR-2521Z were repurposed to serve as light sensors. Other necessary equipment includes cables, capacitors, and a breadboard for testing.

All the modules and the Pico were first “wired” using the breadboard, the connected setup is shown in Fig. 58. Both laser modules are connected to a 5V power supply pin and individual GPIO pins to control them. The Broadcom sensors are connected to a distribution line, which supplies 3V power. To receive data, the sensors needed to be connected to ADC – analog to digital converter pins, which are capable of reading data transmitted from them. The Pico is connected to a computer via a USB cable.

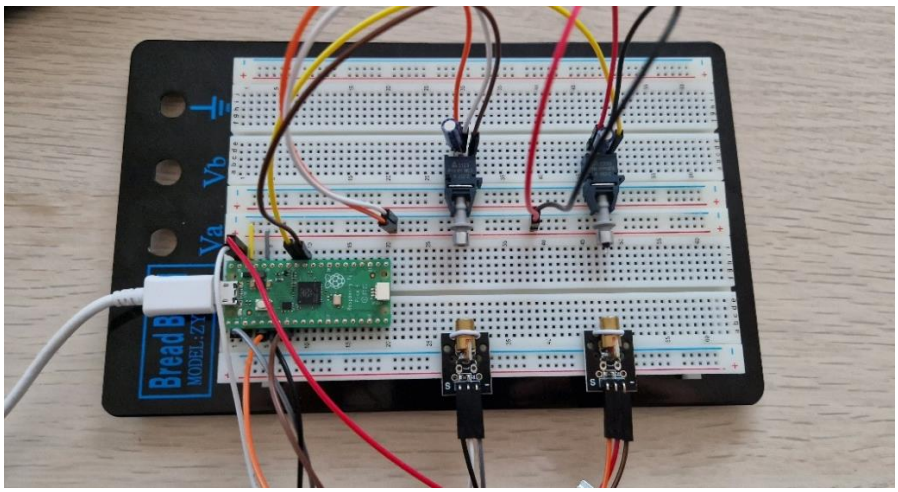

Fig. 58 Connected modules on a breadboard.

To control all the modules using the Pico, two programs were written in an integrated development environment Thonny, which can use a MicroPython programming language, an implementation of the Python 3 language that is optimized for use with microcontrollers:

- Value detection – this program serves to determine the baseline of values reported by the sensor. Upon starting the script, all modules are activated and maximum values reported by the sensors are displayed after a certain amount of time. During the first run, light beams are meant not to be crossed. After this, the script is run again, this time it is necessary to cross the beams. When the light beam is interrupted, the sensor reports an increased value, which differs from the baseline value of the first run and thus serves as a threshold for the second program.
- Speed measurement – is run after the two runs of the value detection script. Firstly, obtained threshold values are inserted into the script, and then it is started. In the beginning, all modules are activated again and the program enters into a loop, during which the reported value of the sensor is compared to the threshold value. As the reported value reaches over, a timer starts and lasts until the value of the second sensor exceeds the set threshold. Based on the imported distance between the sensors and measured time, the speed is calculated and displayed in meters per second.

After testing "by hand" on the breadboard, this setup was transferred to the apparatus to be tested. First, a holder was designed to hold optical cables, which led from the lasers to one side and from the other side connected to the sensor. Four-millimeter holes were drilled in the firing barrel spaced 50 mm apart, over which the holders were positioned, as shown in Fig. 59. Optic cables were held on both sides in connectors, supplied alongside the Broadcom sensors.

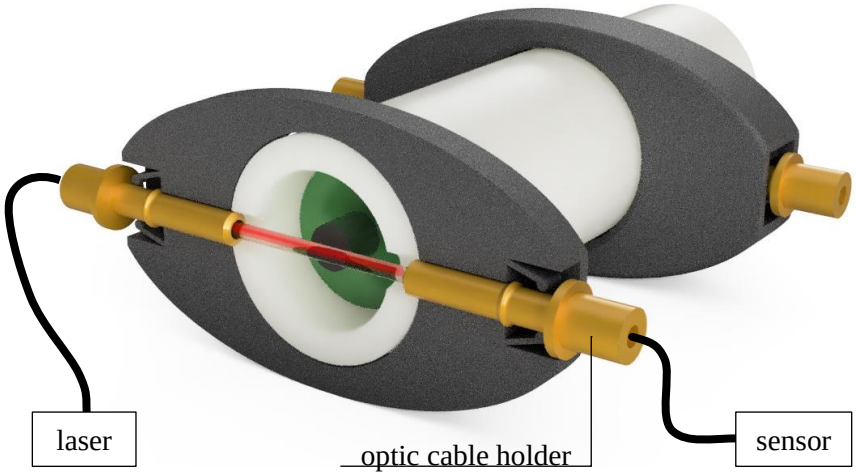

Fig. 59 Dual-beam light-gate rendering.

The setup in this configuration was tested on the apparatus, however, no material samples were used, only the carriages. These were fired at a continuously increasing pressure of the compressed air. In initial tests under low pressure, when the speed of the carriage was lower, the developed setup worked without problem, showing an increase in speed corresponding to pressure increase. However, after exceeding around 45 meters per second, the setup started to behave unexpectedly, and the displayed speeds did not correspond to expectations.

To figure out the issue, the speed measurement program was modified to store values reported by both sensors into a text file, which was then imported into MS Excel after a test. The data was converted into a graph (see Fig. 60) for better representation. For unexplained reasons, when firing the carriages at increased pressure, the sensors reported faulty values in reverse

order, meaning that the first spike in value was seen from the second in-row sensor, only after that did the first sensor see a spike. Furthermore, when the time between spikes was calculated, even though their order was reversed, the value was around 2,2 seconds, whereas the expected time was within a tenths of a second.

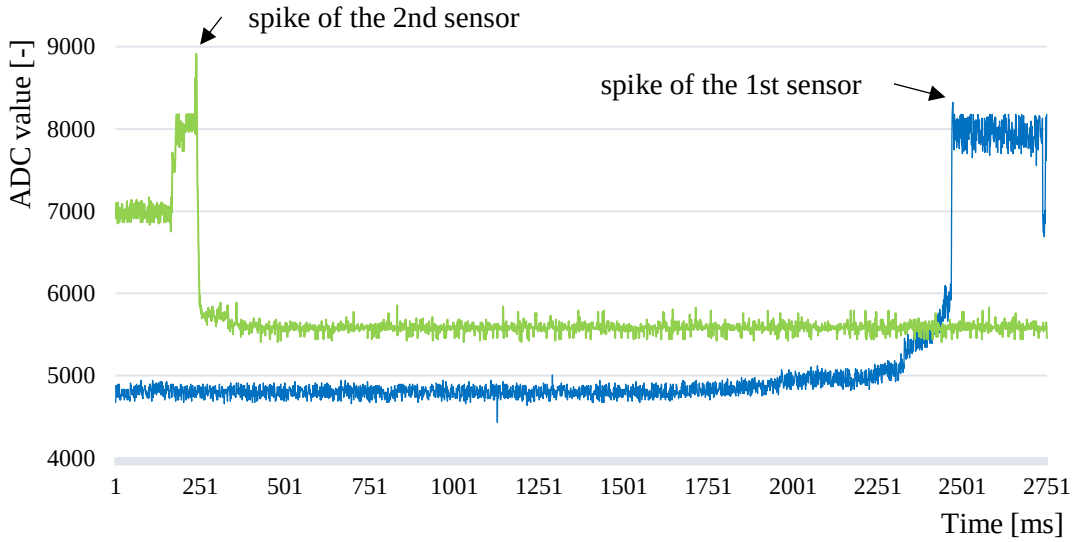

Fig. 60 Graphical representation of reported values.

Following this observation, an attempt was made to repair the developed system to reliably report speed, unfortunately, this was unsuccessful. As of yet, the reason for this unexpected behavior is unknown. The issue may lie in the internal clock speeds of the microprocessor, incompatibility of the sensor lens and the wavelength of light produced by the laser, or incorrect way of utilization.

An attempt at a different setup utilizing proximity sensors was made, which consisted of a set of infrared emitter-receiver YL-73 modules connected to a control board, which adjusted the sensitivity. This setup was also tested but failed at registering speeds exceeding 85 $m \cdot s^{-1}$.

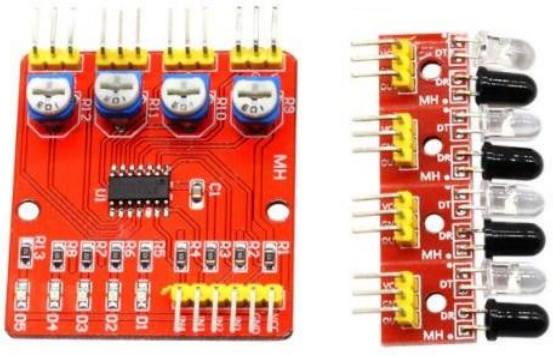

Fig. 61 Proximity sensor [83].

Analytical evaluation of the speed was discussed, however, known models take into consideration only a single barrel, which in this case would not provide accurate results. Furthermore, solving the speed according to the model would require numerical solving of a system of equations. [84; 85]

In the future, this issue will be addressed and resolved. The speeds of impact are therefore for now estimated based on the recorded pressure, at which the test was conducted.

3.6 Testing of a selected material

The capabilities of the device were tested on selected material, in this case, spruce wood. The spruce tree is one of the most commonly found species across Europe. As per the report on the state of Europe's forests in 2020, spruce trees accounted for 23% of the total forested area. Consequently, spruce wood is one of the most frequently used materials in the manufacturing of composite particleboards, OSB, and other similar products. [86]

This material was the subject of a study previously carried out in the laboratory of high-speed deformations. This creates an opportunity for comparison of results obtained by testing the material using the classical Taylor Anvil Test method and the developed symmetric Taylor test device. Furthermore, necessary tests for evaluation, such as deformation under quasistatic conditions and others have already been conducted and evaluated.

The raw material for the test was obtained from Norway spruce trees, aged between 25 and 30 years, harvested during their dormant period (February – March) to prevent loss of their natural moisture. From subsequent semi-finished products in the form of 10x10 millimeter rectangular bars several pieces were selected, which did not contain any natural or mechanical defects. These were then stored in a cooling device at a constant temperature of 2°C. The density of the bars ranged from 489 to 558 $kg \cdot m^{-3}$ and their moisture content ranged from 57 % to 62 %. All of the bars were cut in the longitudinal direction (see Fig. 62) of the wood grain.

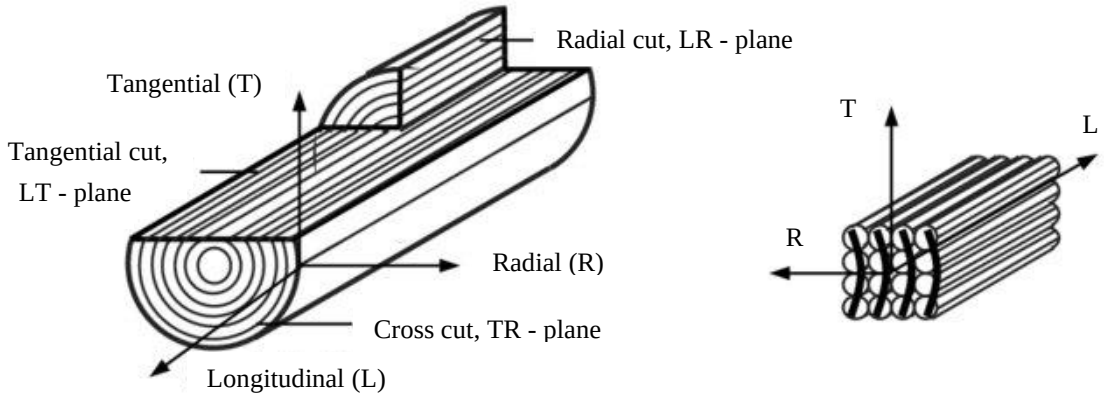

Fig. 62 Different cut directions of wood [87].

To produce samples for the test, the rectangular bars were firstly lathed to a cylindrical shape (see Fig. 63), with a diameter of 10 millimeters and a usable length of 25 millimeters. During the operation of lathing, some of the outside fibers of the wood splintered, which caused small variances in the diameter across the length. Next, the rest of the rectangular portion was cut off using a regular wood saw.

Fig. 63 Lathed spruce wood blank.

Following this, fourteen samples of 20-millimeter length, shown in Fig. 64, were cut from two bars. After sawing, the splayed edges of the samples were removed by a hand file. Next, the faces were ground using a fine sanding disk to ensure their perpendicularity to the axis

Fig. 64 Cut spruce samples.

After preparation, all the samples were categorized. Each pair consisted of an AX and BX sample, with X standing for the number of the pair. These marks were written on the opposite ends of the samples, as shown in Fig. 65.

Fig. 65 Markings on the samples.

Following this, the samples were measured using digital calipers SOMET, measuring their length and diameter. Weight was measured using a laboratory gram scale TSCALE NHB 150+. All the measurements were recorded in an MS Excel spreadsheet, example of this can be seen in Tab. 6 below. The full list of all the sample measurements is included in Attachment 1.

Tab. 6 Example of sample dimensions and weight.

Pair number 1			
Sample A1		Sample B1	
length	20,0 mm	length	20,1 mm
diameter	9,6 mm	diameter	9,6 mm
weight	7 g	weight	7g
Pair number 2			
Sample A2		Sample B2	
length	20,2 mm	length	20,3 mm
diameter	9,5 mm	diameter	9,5 mm
weight	7 g	weight	7g

After measuring, the marked samples were inserted into 3D-printed carriages, which were adjusted to accommodate a larger diameter of the sample. Due to changes in diameter, some of the samples did not sit tightly in the carriage as necessary. This issue was circumvented by rolling a thin strip of Xerox paper around the sample base, which ensured a tight fit.

Fig. 66 Sample in a carriage with paper.

Both samples of pair number 7 unfortunately cracked while being loaded into the carriage, as is shown in Fig. 67. This crack might have been present in the material induced by lathing and subsequent sawing. Nonetheless, this sample pair was also tested.

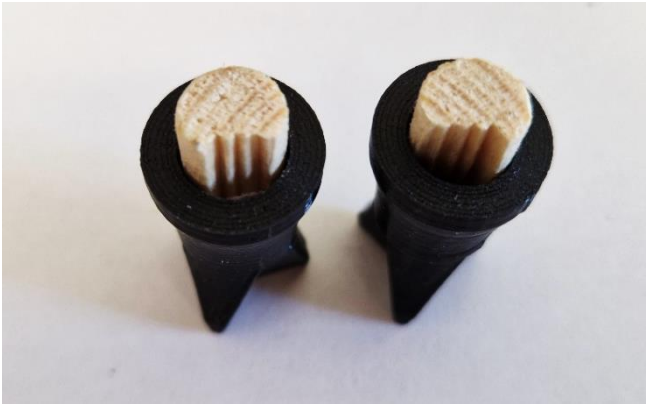

Fig. 67 Sample pair number 7.

3.6.1 Test results

After all the samples were prepared, they were tested on the newly developed canon. A total number of 7 experiments were carried out. Before the testing, the air compressor was started and the air tank was filled to 6 bar pressure. After that, each pair of samples was loaded into the device using the loading tool, and the t-joint flanges were tightened. Following this, the timer was set to 2 minutes and then the power supply was switched on. Everyone present exited the laboratory into the hall for safety. After the audible opening of the valves and consequent shot, samples were recovered from the impact chamber.

The speed of the impact for all experiments is estimated based on the recorded speeds of the classical TAT test device stationed in the laboratory. A graph presented in Fig. 68 shows the measured speed of the impact based on the compressor filling time. The presented graph is simplified, the full version can be seen in Attachment 2. During the filling time, the reported pressure in the air reservoir was recorded to allow an estimation of speed. These speeds are only orientational, the real speeds of the tests are likely to be of a slightly lower value due to the symmetric fire, which pushes the already present air in the barrels against the samples.

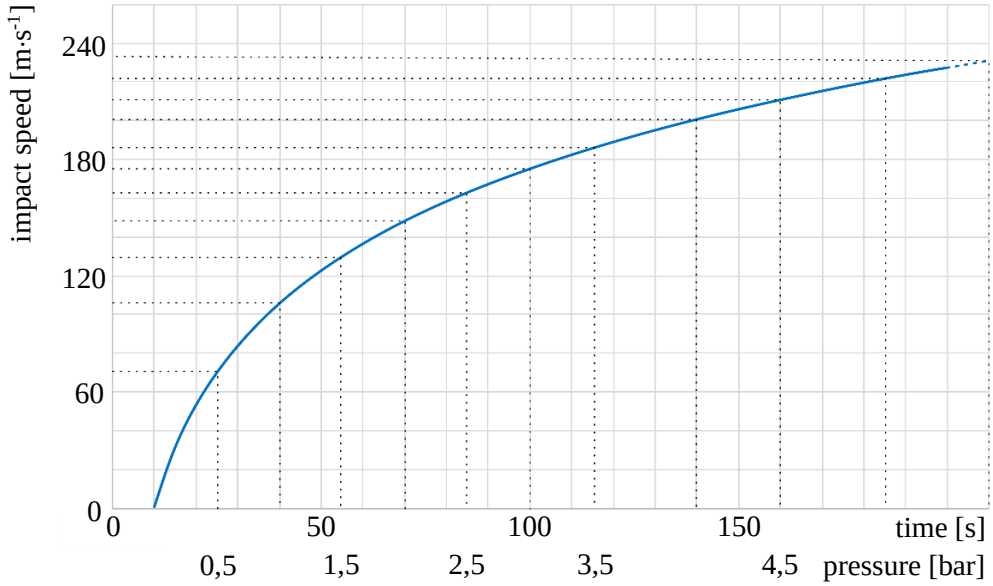

Fig. 68 Plot of impact speed dependent on filling time and pressure.

The pressure at which each experiment was conducted was recorded and is presented in Tab. 7, along with estimated speeds based on recorded speeds of the classical Taylor canon.

Tab. 7 Recorded pressure of each experiment.

Pair Number	6	5	4	3	2	1	7
Pressure [bar]	6	5,5	5	4,5	4	3,5	3
Impact speed [m·s^{-1}]	240+	235	220	210	200	185	175

At sample pair number 6 a missfire occurred. The samples did not hit each other properly. The cause of this occurrence is unknown, and the samples are left out of the validation.

The symmetric impact of the wooden specimen at high speeds caused them to “join” together, where the samples were unable to be separated by hand. Due to this, the measurement of the diameter increase is not possible, therefore, a comparison of initial to final length is provided.

Sample pair 5, Fig. 69, showed the most material splitting along the layers of the wooden structure, causing some splinters to fully separate. The overall length of the retrieved samples was measured to 35,74 mm, from which the crossing depth was evaluated to be 4,36 mm.

Fig. 69 Sample pair number 5.

No evident cracks or material failure was observed at sample pair 4 shown in Fig. 70. This pair showed quite a lot of splintering on the impact interface. The overall length of the retrieved samples was measured to 36,68 mm, the crossing depth was evaluated to 3,72 mm.

Fig. 70 Sample pair number 4.

The highest amount of cracks was observed at sample pair 3, with four cracks developing in sample A3 and three in sample B3. The overall length of the retrieved result was measured to 35,48 mm, the crossing depth was evaluated to 5,02 mm. This increase can be most likely attributed to material failure during impact, which manifested as cracks, the most prominent can be seen in Fig. 71.

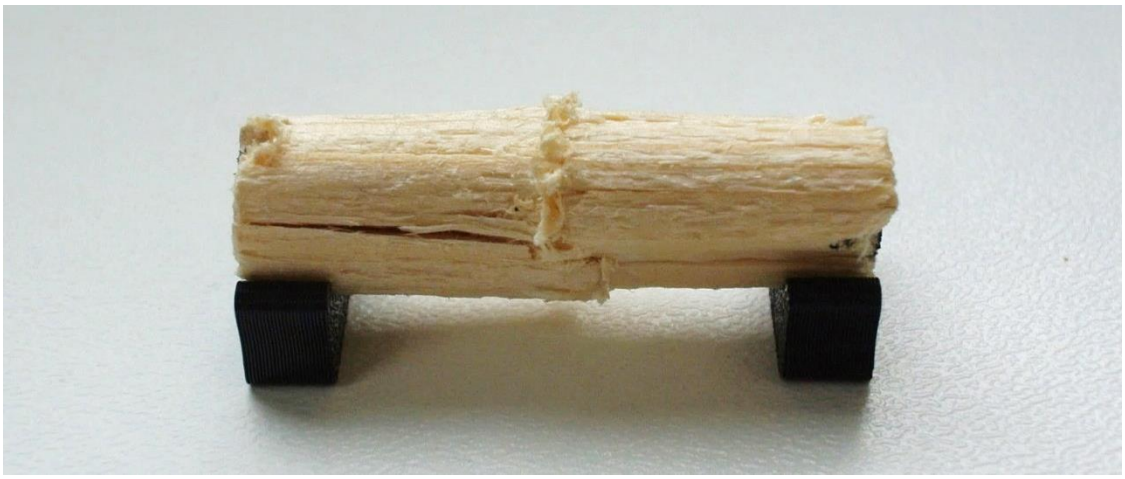

Fig. 71 Sample pair number 3.

Sample pair 2 showed the least amount of defects and the least splintering on the impact interface. The overall length of the retrieved samples was measured to 38,64 mm, the crossing depth was evaluated to 1,86 mm. What is evident, is that as the pressure, and thus speed, of the impact decreases, the depth of the interconnection decreases.

Fig. 72 Sample pair number 2.

More interesting results were obtained with samples fired at lower pressures and lower speeds. In this case, the samples did not stay joined together but separated after the impact. This allowed a closer look at the deformation developed within the different wooden layers. Sample pair 1 is one of such examples, depicted in Fig. 73. A more evident upsetting of the early wood, which is softer, can be observed, with the late, stronger wood, showing almost none. The samples were measured after the test, and their dimensions are stated in Tab. 8.

Tab. 8 Measurements of sample pair number 1.

Sample	Length after impact	Diameter of impacted face
A1	19,92 mm	9,89 mm
B1	19,55 mm	9,76 mm

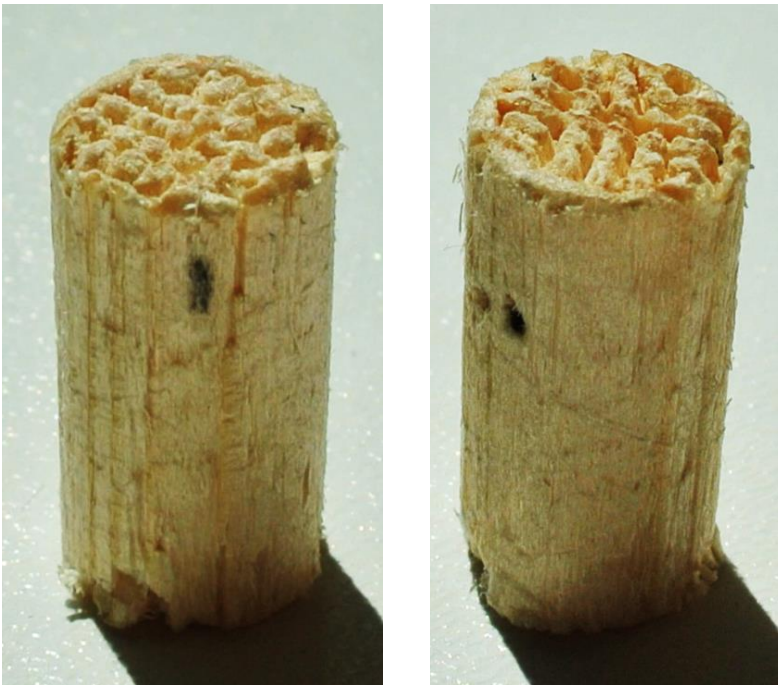

Fig. 73 Sample pair number 1.

This effect is even more evident upon a closer look at sample pair 7. In this case, thanks to previous damage to the wooden sample the upsetting of the early wood can be seen more clearly in Fig. 74. The late wood planes have a slight deformation on the face, but are undeformed deeper into the material, while the early wood is pushed inwards by approximately 0,98 mm.

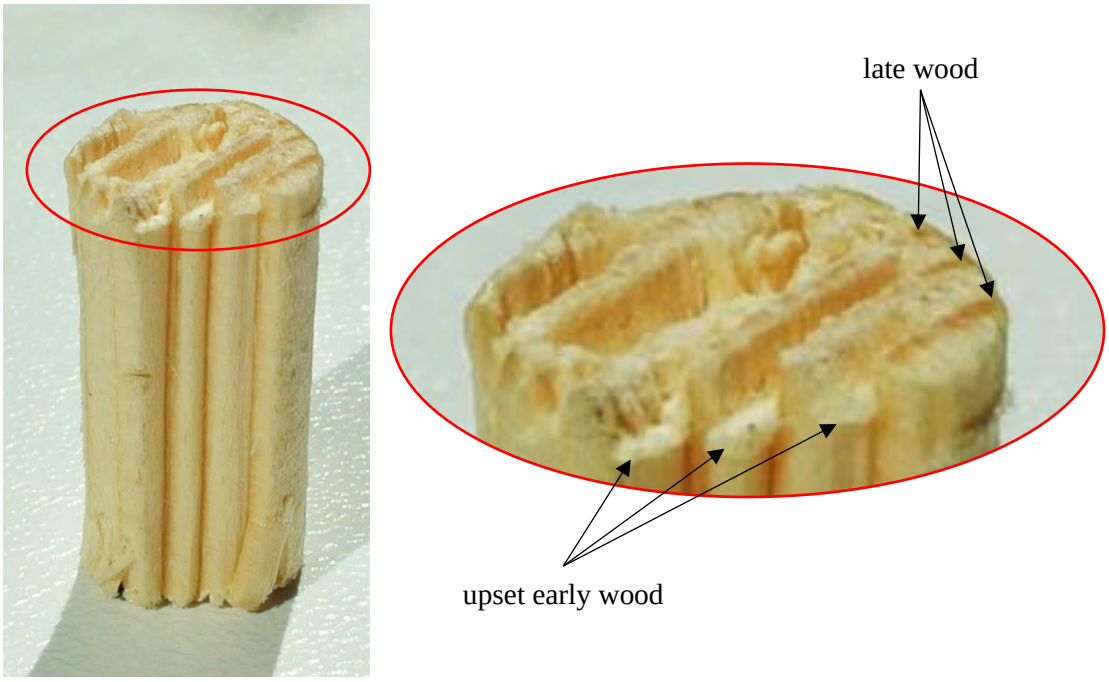

Fig. 74 Closeup of sample damaged pre-test.

Following these observations of results encountered with samples of moist wood, another sample pair was tested. This time the wood was not stored in a cooling device, nor in a sealed container, therefore the expected moisture content was within the range of 10 % to 15 %. This pair was fired at the pressure of 5 bar, corresponding roughly to 220 $m \cdot s^{-1}$. Compared to the more moist wood fired at such pressure, this pair did not stay joined. The results (see Fig. 75) showed an even more prominent upsetting of the early wood. The picture on the right shows the sample observed under a light microscope.

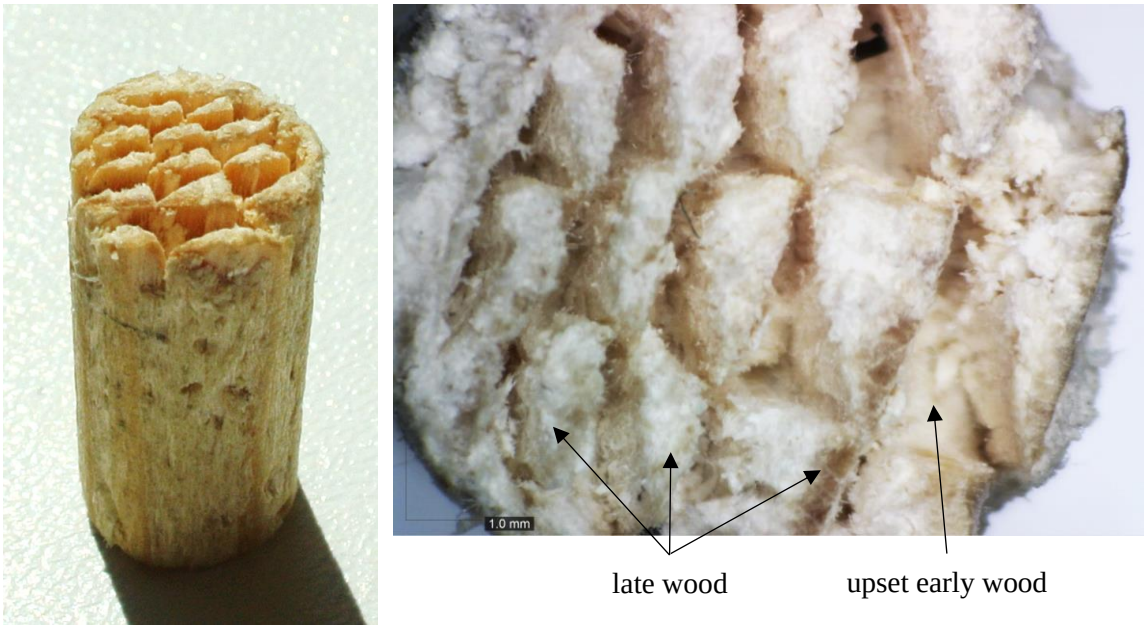

Fig. 75 Dried spruce wood sample.

The obtained results of the symmetrically impacted wooden samples differ substantially from the results of similar samples tested by the typical Taylor canon, impacting a rigid surface. Those results have shown wood fibers splaying outwards from the axis of symmetry, similar to the deformation of metal samples, while the symmetrically impacted samples have shown limited, or none of such deformation.

Fig. 76 Spruce sample from a typical TAT [86].

3.6.2 Simulations

The obtained results were evaluated by Finite Element Analysis, using the Ansys 2024 R1, Student version of the software. Firstly, the project was started through Workbench, which integrates all available tools under the same interface. Next, the appropriate solver was chosen, in this case, the Explicit Dynamics solver, which utilizes explicit time integration and thus is suitable for this case.

After the project was started, material data was needed to properly describe the material. Inserted values are described in Tab. 9. The models implemented were the Johnson Cook Strength and the Johnson Cook Failure.

Tab. 9 Spruce wood material properties [86].

Property name	Variable	Value	Unit
Isotropic Elasticity	Shear modulus	0,139	GPa
	Poisson's ratio	0,1	-
Johnson Cook Strength	Initial yield stress	10,95	MPa
	Hardening constant	30,59	MPa
	Hardening exponent	0,43	-
	Strain rate constant	0,017	-
Johnson Cook Failure	Damage constant D1	0,025	-
	Damage constant D2	0,197	-
	Damage constant D3	-0,084	-
	Damage constant D4	-0,015	-
Density	-	523,5	$kg \cdot m^{-3}$

Next, a 3-dimensional geometry was created using the integrated Design Modeler interface. First, a sketch of the two specimens with 20 mm lengths, distanced 4 mm apart was created and then revolved to create two cylinders. To speed up the simulation, the ¼ symmetry principle was utilized. To do so, two symmetry planes were created, one in the XY plane and the other in the YZ plane. The resulting geometry can be seen in Fig. 77.

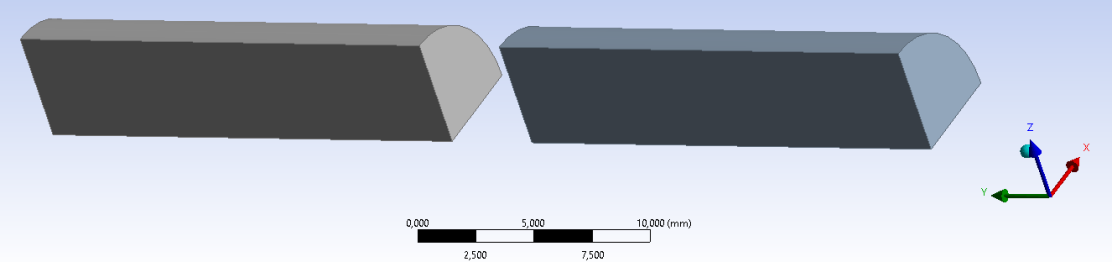

Fig. 77 Created geometry.

Following this, the Mechanical interface was used to adjust the necessary settings for the simulations. Firstly, both samples were assigned the defined spruce material, and then the connections were adjusted, where the solver utilizes a “Body Interactions” function, which was defined to be frictionless.

To define the mesh an Automatic method was used, along with sizing, which enables a selection of an element size. The chosen value was 0,20 millimeters for both samples, this choice was limited by the amount of elements available in the student version. The selected size yielded 108800 elements, and the limitation was at 128000. The created mesh is shown in Fig. 78. As initial conditions, only the speed of the impact was imported, which was the same for both samples. Orientation was defined by the Y-axis component. The simulations were done for speeds of the sample pair 5 – 235 $m \cdot s^{-1}$ and sample pair 1 – 185 $m \cdot s^{-1}$.

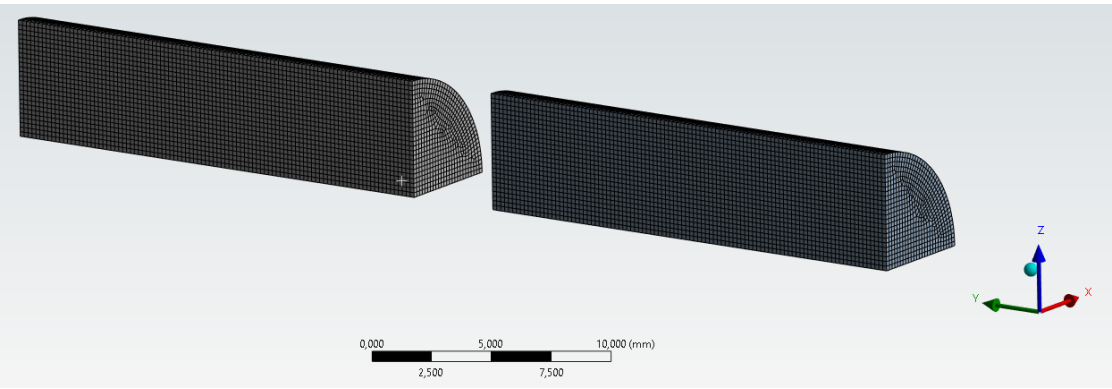

Fig. 78 Meshed samples.

The graphical results of both simulations did not correspond to the observed deformation developed during the experiments. This cause is linked to the nonhomogenous structures of the wooden samples, which would need to be modeled into the simulation software to produce relevant results.

Fig. 79 shows a screenshot of the animated simulation output for a specimen impact speed of 235 $m \cdot s^{-1}$. Unlike the results of practical experiments, here a lot of material is shown to have reached failure conditions specified within the Johnson Cook Failure model. This can be seen as element disintegration into red particles. Furthermore, the overall length of the impacted specimen is in disagreement with the observed practical results. The screenshot is obtained at 8,5485 e^{-005} seconds after the simulation starts. The maximal equivalent elastic strain reached 0,24641, and while it is not visible, it occurred on the impact faces at the time of impact.

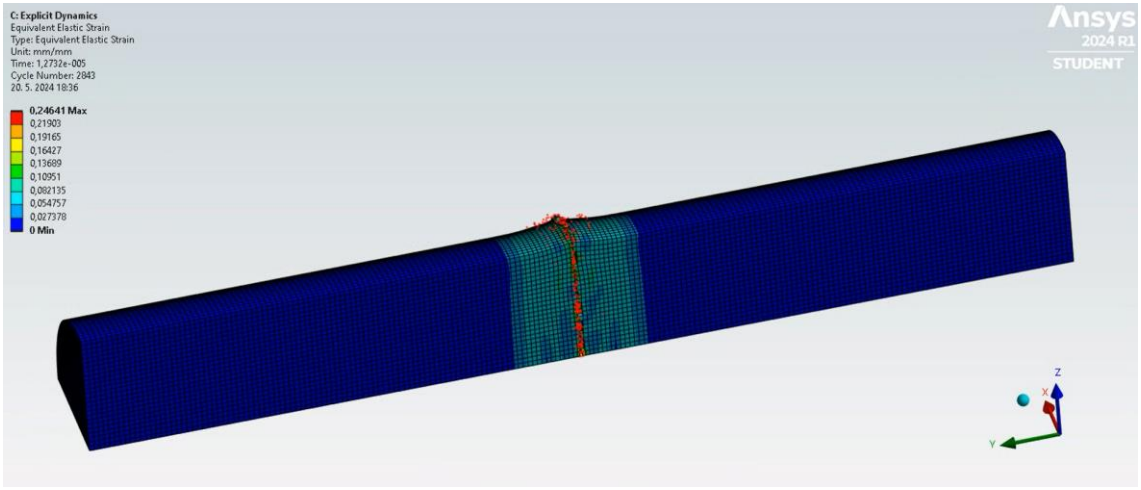

a) impact start

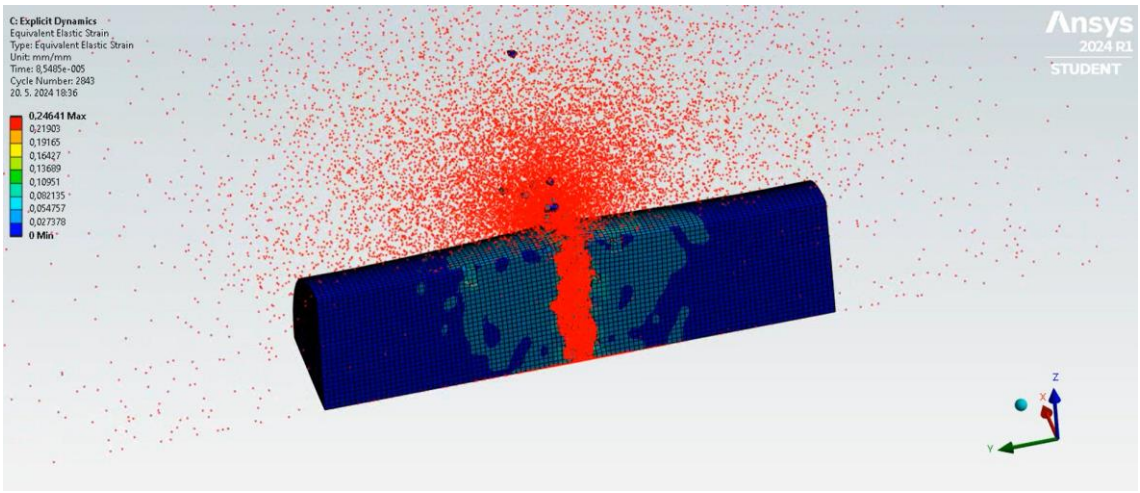

b) impact end

Fig. 79 Equivalent elastic strain at 235 $m \cdot s^{-1}$.

After the impact, the samples did not stay joined together but split apart. To achieve an outcome similar to the practical experiment, the model would need to account for different structures within wooden samples. This would require further testing of the separate layers, which due to time limitations was not attempted.

Simulation of samples impacted at 185 m·s^{-1} produced more relevant results, although still not capturing the shape of the specimen face obtained through practical experiments. Upon impact, separate elements on the impacting faces started to disintegrate, following the failure model. This continued until the sample speeds reached zero. The maximal equivalent elastic strain achieved reached 0,19704. Screenshots from the simulation are shown in Fig. 80 below.

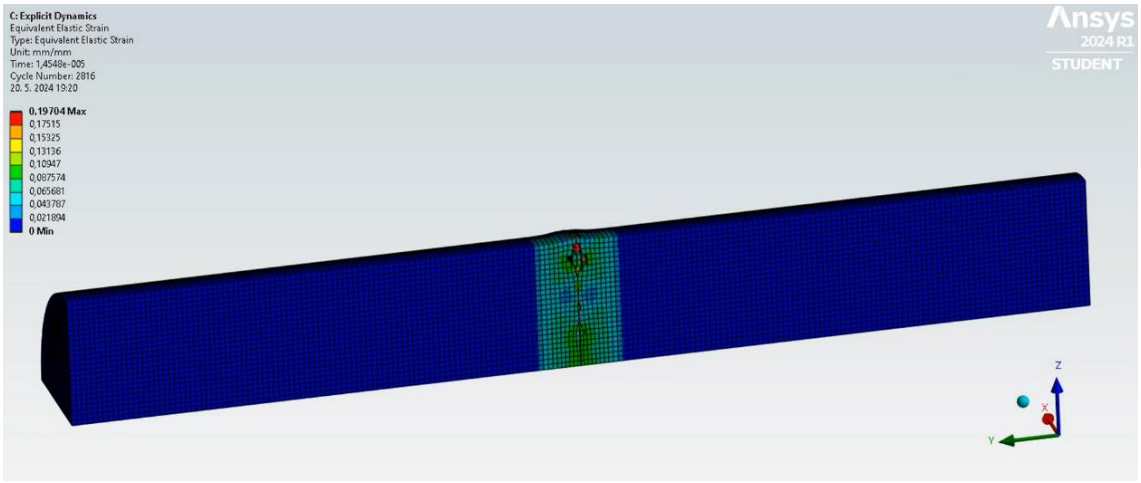

a) impact start

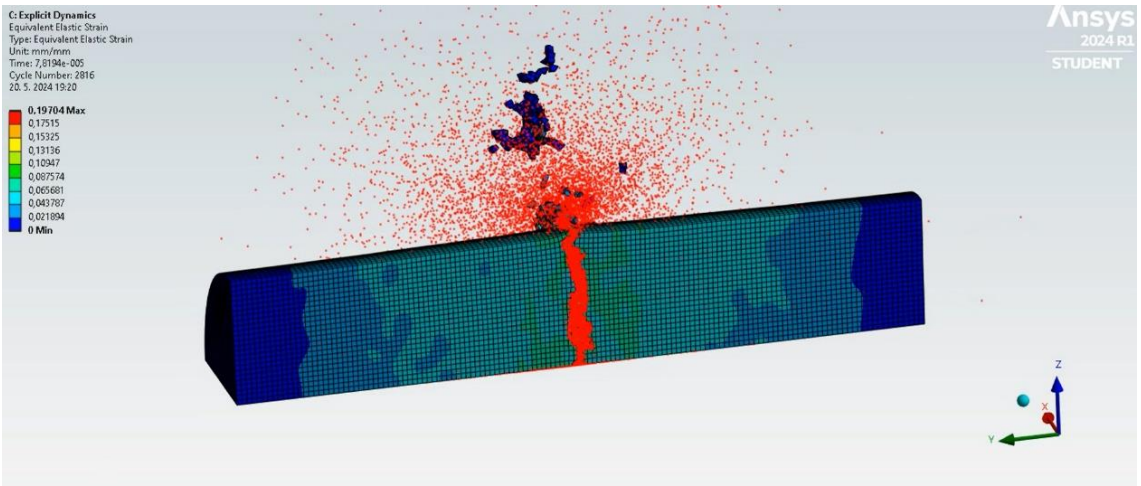

b) impact end

Fig. 80 Equivalent elastic strain at 185 m·s^{-1}.

An interesting occurrence at lower speeds is the separation of some parts of the specimen, which would fly away from the impact zone. This did not occur at higher speeds and was more pronounced at speeds even lower than 185 m·s^{-1}.

As mentioned before, the results of the simulations do not reflect results obtained by practical experiments and therefore a lot less focus is given to them. Further adjustments to the material definition are required and will be the aim of future works.

CONCLUSION

The main aim of the presented thesis was the development of an innovative testing apparatus based on the working principles of the Taylor Anvil Test, which is used to investigate material behavior under dynamic conditions of loading. For this reason, the research part of the thesis describes used techniques and devices for the evaluation of this behavior. More attention is given to various configurations of the Taylor Anvil Test device, where the advantages of each different type are described, along with the schematics and inner constructions. To make use of the data obtained during tests, evaluation principles, and constitutive models are also described, focusing on the different approaches.

The manufacturing of the developed apparatus is described in detail in the practical part of this thesis. Each step of the process is commented on, along with presented figures, describing crucial decisions impacting the outcome of the development. A fully constructed apparatus was tested using Aluminum samples of a 5 mm diameter. The results showed some significant problems, one of which was the concentricity of impact. This was estimated based on an investigation of the sample impact faces to be within the range of 1,2 – 1,3 mm. Another issue was pressure loss resulting in minimal deformation, measured at 5,05 mm. Based on the observed problems the whole device was reassembled.

Second testing showed a sizable improvement in addressed points of interest. The concentricity of the impact was within 0,1 mm. Plastic deformation development also improved significantly, with tested samples deformed to a diameter of 5,43 mm measured on the impact face.

For actual material testing, spruce wood samples with natural moisture levels were chosen, prepared, and measured. The results were compared to the previous investigation of this material conducted via the classic Taylor canon. The obtained results have shown unexpected deformation patterns within the samples, where the nonhomogenous texture of the wood reacted differently for the symmetric impact. Presented samples show a significant upsetting of the early wooden parts of the structure, while the layers of late wood have shown very few deformation signs. For a test, another sample pair of dried wood was tested, where the developed texture is even more evident.

These results were compared to simulations conducted through the Ansys simulation software. The simulations however did not represent the observed samples fully. The issue was linked to the inner structure of the wooden samples, which would need to be implemented into the material model for simulation.

Overall the developed device proved to be functional and capable of producing results with enough reproducibility. The innovative approach can be beneficial for the investigation of mutual interaction of organic materials and will be used in future studies.

LIST OF SOURCES

1. FOREJT, Milan; KREJČÍ, Jan a BUCHAR, Jaroslav. *High Strain Rate Phenomena in Metal Forming: New courses in Engineers Education*. In: ROSSMANITH, H.P. Teaching and Education in Fracture and Fatigue. Great Britain: TJ press, 1996, s. 309-318. ISBN 0-419-20700-7.
2. CHEN, D.Y.; XU, Y.; ZHANG, S.H.; MA, Y.; EL-ATY, A.A.; POKROVSKY, A.I.; BAKINOVSKAYA, A.A. *A novel method to evaluate the high strain rate formability of sheet metals under impact hydroforming*. J. Mater. Process. Technol. 2021, 287, 116553.
3. SIMUNOVIC, Srdan; NUKALA, Phani Kumar V. V; FEKETE, James; MEULEMAN, David a MILITITSKY, Marcio. *Modeling of Strain Rate Effects in Automotive Impact*. 2003. ISSN 0148-7191. Dostupné z: https://doi.org/10.4271/2003-01-1383.
4. EKABOTE, Nagaraj; KODANCHA, Krishnaraja G.; YUNUS KHAN, T.M. a BADRUDDIN, Irfan Anjum. Effect of Strain Rate and Temperature on Tensile and Fracture Performance of AA2050-T84 Alloy. Online. *Materials*. 2022, roč. 15, č. 4, s. 1590. ISSN 1996-1944. Dostupné z: https://doi.org/10.3390/ma15041590.
5. WANG, Wei; MA, Yan; YANG, Muxin; JIANG, Ping; YUAN, Fuping et al. *Strain rate effect on tensile behavior for a high specific strength steel: From quasi-static to intermediate strain rates*. Online. Metals (Basel). 2018, roč. 8, č. 1, s. 11. ISSN 2075-4701. Dostupné z: https://doi.org/10.3390/met8010011.
6. HATEBUR. Online. Available at: https://www.hatebur.com/en/. [cit. 2023-10-08].
7. The Federal Group USA. Online. Dostupné z: https://www.tfgusa.com/about-us/.
8. Miravag Cold Forming Technology LTD. Online. Dostupné z: https://mivrag.co.il/en/. [cit. 2024-03-09].
9. ROSENBERG, Zvi a DEKEL, Erez. Material Models for Numerical Simulations. Online. *Terminal Ballistics*. 2020, s. 27-48. Dostupné z: https://doi.org/10.1007/978-3-030-46612-1_2. [cit. 2024-03-09].
10. GRZNÁR, Patrik; GREGOR, Milan; KRAJČOVIČ, Martin; MOZOL, Štefan; SCHICKERLE, Marek et al. Modeling and simulation of processes in a factory of the future. Online. *Applied sciences*. 2020, roč. 10, č. 13, s. 4503. ISSN 2076-3417. Dostupné z: https://doi.org/10.3390/app10134503. [cit. 2024-03-09].
11. FOREJT, Milan. *Konstitutivní vztahy pro rychlosti deformace v technologiích tváření*. 2. mezinárodní konference FORM 95. 1998, s. 77-82.
12. MIELNIK, E.M. *Metalworking Science and Engineering*. McGraw-Hill Companies, 1991. ISBN 9780070419056.
13. MEYERS, Marc A. *Dynamic Behavior of Materials*. New York: John Wiley, 1994. ISBN 9780471582625.
14. VOLKOV, Grigori; BORODIN, Elijah a BRATOV, Vladimir. Numerical simulations of Taylor anvil-on-rod impact tests using classical and new approaches. Online. In: *Procedia Structural Integrity*. Elsevier B.V, 2017, s. 330-335. ISSN 2452-3216. Dostupné z: https://doi.org/10.1016/j.prostr.2017.11.050. [cit. 2024-03-16]
15. JOPEK, Miroslav. *Modelování mechanického chování ocelí za vyšších rychlostí deformace*. PhD thesis. Vysoké učení technické v Brně. Fakulta strojního inženýrství, Brno, 2003. ISBN 80-214-2437-0.
16. BAI, Y. L. a DODD, B. *Adiabatic Shear Localization: Occurrence, Theories and Applications*. Oxford: Pergamon Press Great Britain, 1992.

17. DAVISON, Lee; GRADY, Dennis E. a SHAHINPOOR, Mohsen (ed.). *High-Pressure Shock Compression of Solids II*. Online. New York, NY: Springer New York, 1996. ISBN 978-1-4612-7501-5. Dostupné z: https://doi.org/10.1007/978-1-4612-2320-7.
18. WRIGHT, Roger N. Mechanical Properties of Wire and Related Testing. Online. In: *Wire Technology*. Elsevier, 2016, s. 129-157. ISBN 9780128026502. Dostupné z: https://doi.org/10.1016/B978-0-12-802650-2.00011-X. [cit. 2024-04-26].
19. SVOBODA, Petr; JOPEK, Miroslav; SVOBODA, Ondrej a HARANT, Martin. Determination of dynamic properties of 3D printed G3SI1 steel. Online. *MM Science Journal*. 2024, roč. 2024, č. 2. ISSN 18031269. Dostupné z: https://doi.org/10.17973/MMSJ.2024_03_2021183.
20. GILLIS P. P., GROSS T. S.: *Effect of Strain Rate on Flow Properties*. Metals handbook, Ninth Edition, Volume 8 – Mechanical Testing. American Society for Metals, Ohio, 1985.
21. HOPKINSON, John. *On the Rupture of Iron Wire by a Blow*. Proceedings of the Manchester Literary and Philosophical Society. 1872, s. 40-45.
22. MIYAMBO, Mangalani Edward; VON KALLON, Daramy Vandi; PANDELANI, Thanyani a REINECKE, John David. Review of the development of the split Hopkinson pressure bar. Online. *Procedia CIRP*. 2023, roč. 119, s. 800-808. ISSN 2212-8271. Dostupné z: https://doi.org/10.1016/j.procir.2023.04.010. [cit. 2024-04-27].
23. DAVIES, R. M. *A critical study of the Hopkinson pressure bar*. Philosophical Transactions of the Royal Society of London.Series A, Mathematical and Physical Sciences. 1948, roč. 240, s. 375-457.
24. KOLSKY, H. An Investigation of the Mechanical Properties of Materials at very High Rates of Loading. Online. *Proceedings of the Physical Society*. Section B. 1949, roč. 62, č. 11, s. 676-700. ISSN 0370-1301. Dostupné z: https://doi.org/10.1088/0370-1301/62/11/302. [cit. 2024-04-27].
25. BUDIWANTORO, Bagus; FAIZAH, Iffah; PRABOWO, Dini A.; FEBRINAWARTA, Burhan a KARIEM, Muhammad A. Results comparison for hat-shaped, double-notch and punch testing of split Hopkinson shear bar technique. Online. *Journal of Engineering and Technological Sciences*. 2019, roč. 51, č. 6, s. 805-823. ISSN 2337-5779. Dostupné z: https://doi.org/10.5614/j.eng.technol.sci.2019.51.6.5. [cit. 2024-04-27].
26. MEYER, Lothar W. *Material Behaviour at High Strain Rates*. Online. 2004. Dostupné z: https://doi.org/10.17877/DE290R-12976. [cit. 2024-04-27].
27. BREPTA, Rudolf a PROKOPEC, Miroslav. *Šíření napěťových vln a rázy v tělesech*. Praha: Academia, 1972.
28. CHEN, Y.; CLAUSEN, A.H.; HOPPERSTAD, O.S. a LANGSETH, M. Application of a split-Hopkinson tension bar in a mutual assessment of experimental tests and numerical predictions. Online. *International journal of impact engineering*. 2011, roč. 38, č. 10, s. 824-836. ISSN 0734-743X. Available at: https://doi.org/10.1016/j.ijimpeng.2011.05.002. [cit. 2023-10-16].
29. K., Ravi-Chandar a (ed.). Dynamic Loading and Crack Arrest. In: *Comprehensive Structural Integrity*. Volume 7.09. Elsevier Science, 2003, s. 347-426. ISBN 978-0-08-043749-1.
30. YU, Tongxi a XUE, Pu. Introduction to dynamic plasticity. Online. In: *Introduction to Engineering Plasticity*. Elsevier, 2022, s. 327-371. ISBN 9780323989817. Dostupné z: https://doi.org/10.1016/B978-0-323-98981-7.00012-9. [cit. 2024-04-27].

31. EL-ATY, Ali Abd; XU, Yong; ZHANG, Shihong; MA, Yan a CHEN, Dayong. Experimental investigation of tensile properties and anisotropy of 1420, 8090 and 2060 Al-Li alloys sheet undergoing different strain rates and fibre orientation: a comparative study. Online. *Procedia Engineering*. 2017, roč. 207, s. 13-18. ISSN 1877-7058. Available at: https://doi.org/10.1016/j.proeng.2017.10.730. [cit. 2023-10-16].
32. ŠLAIS, Miroslav. *Studium vlivu rychlostních a teplotních parametrů na tvařitelnost Ti slitin*, PhD thesis Vysoké učení technické v Brně. Fakulta strojního inženýrství, Brno, 2012.
33. TAYLOR, Geoffrey Ingram. The testing of materials at high rates of loading. Online. *Journal of the Institution of Civil Engineers*. 1946, s. 486-519. Dostupné z: https://doi.org/10.1680/ijoti.1946.13699. [cit. 2024-04-28].
34. TAYLOR, Geoffrey Ingram. *The use of flat-ended projectiles for determining dynamic yield stress I. Theoretical considerations*. Proceedings of the Royal Society of London: Series A, Mathematical and Physical Sciences. 1948, roč. 194, č. 1038, s. 289–299.
35. WHIFFIN, A. C. The use of flat-ended projectiles for determining dynamic yield stress - II. Tests on various metallic materials. Online. *Proceedings of the Royal Society of London*. Series A. Mathematical and Physical Sciences. 1948, s. 300-322. Dostupné z: https://doi.org/https://api.semanticscholar.org/CorpusID:136832479. [cit. 2024-04-28].
36. KUNČICKÁ, Lenka; JOPEK, Miroslav; KOCICH, Radim a DVOŘÁK, Karel. Determining johnson-cook constitutive equation for low-carbon steel via taylor anvil test. Online. *Materials*. 2021, roč. 14, č. 17, s. 4821. ISSN 1996-1944. Dostupné z: https://doi.org/10.3390/ma14174821. [cit. 2024-03-10].
37. EAKINS, D. E. a THADHANI, N. N. Instrumented Taylor anvil-on-rod impact tests for validating applicability of standard strength models to transient deformation states. Online. *Journal of applied physics*. 2006, roč. 100, č. 7, s. 073503-073503-8. ISSN 0021-8979. Dostupné z: https://doi.org/10.1063/1.2354326. [cit. 2024-03-16].
38. MÜLLER, Samuel. *Vývoj impaktoru pro Taylorův test*. Vysoké učení technické v Brně. Fakulta strojního inženýrství, 2022.
39. LIU, Jiancheng; PI, Aiguo; WU, Haijun a HUANG, Fenglei. Dynamic response of reverse Taylor impact based on DIC technology. Online. In: *EPJ Web of Conferences*. Les Ulis: EDP Sciences, 2015, s. 1074. ISBN 2759818179. ISSN 2101-6275. Dostupné z: https://doi.org/10.1051/epjconf/20159401074. [cit. 2024-04-10].
40. GUST, W. H. High impact deformation of metal cylinders at elevated temperatures. Online. *Journal of Applied Physics*. 1982, roč. 53, č. 5, s. 3566-3575. ISSN 0021-8979. Dostupné z: https://doi.org/10.1063/1.331136. [cit. 2024-04-28].
41. SCOTT, Nicholas R.; NELMS, Matthew D. a BARTON, Nathan R. Assessment of reverse gun taylor cylinder experimental configuration. Online. *International Journal of Impact Engineering*. 2021, roč. 149. ISSN 0734743X. Dostupné z: https://doi.org/10.1016/ j.ijimpeng.2020.103772. [cit. 2024-04-28].
42. EAKINS, D. a THADHANI, N.N. Analysis of dynamic mechanical behavior in reverse Taylor anvil-on-rod impact tests. Online. *International journal of impact engineering*. 2007, roč. 34, č. 11, s. 1821-1834. ISSN 0734-743X. Dostupné z: https://doi.org/10.1016/j.ijimpeng.2006.11.001. [cit. 2024-04-10].
43. THORINGTON-JONES, B.; WHITEMAN, G.; SMITH, L. C.; CHAPMAN, D. J. a EAKINS, D. E. Assessment of heated reverse Taylor cylinder experiments for the calibration of tantalum strength models. Online. In: *AIP Conference Proceedings*. Melville: American Institute of Physics, 2023. ISSN 0094-243X. Dostupné z: https://doi.org/10.1063/12.0020430. [cit. 2024-04-11].

44. STRAND, O T; GOOSMAN, D R; MARTINEZ, C; WHITWORTH, T L a KUHLOW, W W. Compact system for high-speed velocimetry using heterodyne techniques. Online. *Review of scientific instruments*. 2006, roč. 77, č. 8, s. 083108-083108-8. ISSN 0034-6748. Dostupné z: https://doi.org/10.1063/1.2336749. [cit. 2024-04-13].
45. ERLICH, D. C.; SHOCKEY, D. A. a SEAMAN, L. Symmetric rod impact technique for dynamic yield determination. Online. In: *AIP Conference Proceeding Volume 78*. AIP, 1982, s. 402-406. Dostupné z: https://doi.org/10.1063/1.33348. [cit. 2024-04-14].
46. FORDE, L.C; PROUD, W.G a WALLEY, S.M. Symmetrical Taylor impact studies of copper. Online. *Proceedings of the Royal Society A: Mathematical, Physical and Engineering Sciences*. 2009, roč. 465, č. 2103, s. 769-790. ISSN 1364-5021. Dostupné z: https://doi.org/10.1098/rspa.2008.0205. [cit. 2024-04-14].
47. MOĆKO, W.; JANISZEWSKI, J.; RADZIEJEWSKA, J. a GRĄZKA, M. Analysis of deformation history and damage initiation for 6082-T6 aluminium alloy loaded at classic and symmetric Taylor impact test conditions. Online. *International journal of impact engineering*. 2015, roč. 75, s. 203-213. ISSN 0734-743X. Dostupné z: https://doi.org/10.1016/j.ijimpeng.2014.08.015. [cit. 2024-04-14].
48. COUQUE, H. Symmetric Taylor testing procedures for material strength ranging from 400 to 2000 MPa. Online. *Le Journal de Physique IV*. 2000, roč. 10, č. PR9, s. Pr9-179-Pr9-184. ISSN 1155-4339. Dostupné z: https://doi.org/10.1051/jp4:2000930.
49. COUQUE, Hervé. Experimental and numerical analyses of the dynamic failure processes of symmetric Taylor impact specimens. Online. In: *EPJ Web of Conferences*. Les Ulis: EDP Sciences, 2018, s. 1043. ISBN 2759890538. ISSN 2101-6275. Dostupné z: https://doi.org/10.1051/epjconf/201818301043. [cit. 2024-04-14].
50. WALLEY, S. M.; TAYLOR, N. E.; WILLIAMSON, D. M. a JARDINE, A. P. A novel technique for performing symmetric Taylor impact. Online. In: *EPJ Web of Conferences*. Les Ulis: EDP Sciences, 2015, s. 1029. ISBN 2759818179. ISSN 2101-6275. Dostupné z: https://doi.org/10.1051/epjconf/20159401029. [cit. 2024-04-14].
51. JANNOTTI, Phillip; LORENZO, Nicholas a MEREDITH, Chris. Time-Resolved Characterization of Taylor Impact Testing. Online. In: SILBERSTEIN, Meredith a AMIRKHIZI, Alireza (ed.). *Challenges in Mechanics of Time Dependent Materials*, Volume 2. Conference Proceedings of the Society for Experimental Mechanics Series. Cham: Springer International Publishing, 2021, s. 63-68. ISBN 978-3-030-59541-8. Dostupné z: https://doi.org/10.1007/978-3-030-59542-5_11. [cit. 2024-04-28].
52. NUSSBAUM, Julien a FADERL, Norbert. Evaluation of strength model parameters from Taylor impact tests. Online. *Procedia Engineering*. 2011, roč. 10, s. 3453-3458. ISSN 1877-7058. Dostupné z: https://doi.org/10.1016/j.proeng.2011.04.569. [cit. 2024-01-21].
53. BANABIC, D. *Formability of metallic materials: plastic anisotropy, formability testing, forming limits*. Berlin: Springer, 2000. ISBN 3-540-67906-5.
54. HERNANDEZ, C.; MARANON, A.; ASHCROFT, I.A. a CASAS-RODRIGUEZ, J.P. A computational determination of the Cowper–Symonds parameters from a single Taylor test. Online. *Applied mathematical modelling*. 2013, roč. 37, č. 7, s. 4698-4708. ISSN 0307-904X. Dostupné z: https://doi.org/10.1016/j.apm.2012.10.010. [cit. 2024-04-13].
55. HOSFORD, William F. *Mechanical Behavior of Materials*. 9780521846707. 1. Cambridge: Cambridge University Press, 2005. ISBN 9780521846707. Dostupné z: https://doi.org/10.1017/CBO9780511810930.
56. U.S. Department of Energy, Material Science. *DOE Fundamentals Handbook*, Volume 1 and 2. January 1993.

57. LI, Tao; ZHENG, Jinyang a CHEN, Zhiwei. Description of full-range strain hardening behavior of steels. Online. *SpringerPlus*. 2016, roč. 5, č. 1, s. 1316-1316. ISSN 2193-1801. Dostupné z: https://doi.org/10.1186/s40064-016-2998-3. [cit. 2024-01-28].
58. ZHAO, Shixiang; PETROV, Yu. V.; ZHANG, Yuyi; VOLKOV, G.A.; XU, Zejian et al. Modeling of the thermal softening of metals under impact loads and their temperature–time correspondence. Online. *International journal of engineering science*. 2024, roč. 194, s. 103969. ISSN 0020-7225. Dostupné z: https://doi.org/10.1016/j.ijengsci.2023.103969. [cit. 2024-01-28].
59. CHAPMAN, D.J.; RADFORD, D.D. a WALLEY, S.M. *A History of the Taylor Test and Its Present Use in the Study of Lightweight Materials*. 2005.
60. WŁODARCZYK, E. a SARZYNSKI, M. *Strain energy method for determining dynamic yield stress in Taylor's test*. Engineering Transactions. 2017, roč. 65, s. 499-511.
61. HUTCHINGS, I.M. and O'BRIEN, T.J. Normal impact of metal projectiles against a rigid target at low velocities. Online. *International journal of mechanical sciences*. 1981, roč. 23, č. 5, s. 255-261. ISSN 0020-7403. Dostupné z: https://doi.org/10.1016/0020-7403(81)90029-1. [cit. 2024-04-20].
62. WILKINS, Mark L. a GUINAN, Michael W. Impact of cylinders on a rigid boundary. Online. *Journal of Applied Physics*. 1973, roč. 44, č. 3, s. 1200-1206. ISSN 0021-8979. Dostupné z: https://doi.org/10.1063/1.1662328. [cit. 2024-04-20].
63. HOLLOMON, John H. *Tensile deformation*. Aime Trans. 1945, roč. 12, č. 4, s. 1-22.
64. SUNG, Ji Hyun; KIM, Ji Hoon a WAGONER, R.H. A plastic constitutive equation incorporating strain, strain-rate, and temperature. Online. *International journal of plasticity*. 2010, roč. 26, č. 12, s. 1746-1771. ISSN 0749-6419. Dostupné z: https://doi.org/10.1016/j.ijplas.2010.02.005. [cit. 2024-04-18].
65. HOLMQUIST, T. J. a JOHNSON, G. R. Determination of constants and comparison of results for various constitutive models. Online. *Le Journal de Physique IV*. 1991, roč. 01, č. C3, s. C3-853-C3-860. ISSN 1155-4339. Dostupné z: https://doi.org/10.1051/jp4:19913119.
66. ZERILLI, Frank J. and ARMSTRONG, Ronald W. Dislocation-mechanics-based constitutive relations for material dynamics calculations. Online. *Journal of applied physics*. 1987, roč. 61, č. 5, s. 1816-1825. ISSN 0021-8979. Dostupné z: https://doi.org/10.1063/1.338024. [cit. 2024-04-20].
67. ZERILLI, Frank J. Dislocation mechanics-based constitutive equations. Online. *Metallurgical and Materials Transactions A*. 2004, roč. 35, č. 9, s. 2547-2555. ISSN 1073-5623. Dostupné z: https://doi.org/10.1007/s11661-004-0201-x.
68. MAJZOOBI, G. H.; KAZEMI, P. a PIPELZADEH, M. K. Determination of the Constants of Material Models Using Inverse Taylor Test. Online. *Experimental techniques*. 2016, roč. 40, č. 2, s. 609-620. ISSN 0732-8818. Dostupné z: https://doi.org/10.1007/s40799-016-0062-4. [cit. 2024-04-21].
69. JOHNSON, G. R. Dynamic Analysis of a Torsion Test Specimen Including Heat Conduction and Plastic Flow. Online. *Journal of Engineering Materials and Technology*. 1981, roč. 103, č. 3, s. 201-206. ISSN 0094-4289. Dostupné z: https://doi.org/10.1115/1.3225001. [cit. 2024-04-21].
70. JOHNSON, G. R. *Dynamic Analysis of a Torsion Test Specimen Including Heat Conduction and Plastic Flow*. Journal of Engineering Materials and Technology-transactions of The Asme. 1981, roč. 103, s. 201-206.

71. JOHNSON, G. R. a COOK, W. H. *A Constitutive Model and Data for Metals Subjected to Large Strains, High Strain Rates, and High Temperatures*. Proceedings 7th International Symposium on Ballistics, The Hague. 1983, s. 541-547.
72. ANDRADE U., MEYERS M. A., CHOKSHI A. H.: *Scripta Met. at Mat*. In press, 1993.
73. FOLLANSBEE, P. S.; REGAZZONI, G. a KOCKS, U. F. *Mechanical Properties of Materials at High Rates of Strain*. Institute of Physics, London. 1984.
74. LIU, G.R a QUEK, S. S. *Finite Element Method: A Practical Course*. 1. San Diego: Elsevier Science, 2003. ISBN 0080472761. Dostupné z: https://doi.org/10.1016/B978-0-7506-5866-9.X5000-2.
75. MOHAMMADI, Soheil. *Extended finite element method for fracture analysis of structures*. Oxford: Blackwell Publishing, 2008. ISBN 978-1-4051-7060-4.
76. UNIVERSITY OF VICTORIA. *Introduction to Finite Element Analysis*. Online. Dostupné z: https://www.engr.uvic.ca/~mech410/lectures/FEA_Theory.pdf.
77. ENTE©RFEA. *Enterfea - online courses*. Online. Dostupné z: https://enterfea.com/academy/online-courses/. [cit. 2024-05-04].
78. DASSAULT SYSTÈMES SIMULIA CORP. *Abaqus Documentation*. Online. Dostupné z: https://classes.engineering.wustl.edu/2009/spring/mase5513/abaqus/docs/v6.5/books/gsa/default.htm. [cit. 2024-05-04].
79. RK ROSE KRIEGER GMBH - VERBINDUNGS- UND POSITIONERSYSTEME. *BLOCAN® aluminium profile systems*. Online. Dostupné z: https://www.rk-rose-krieger.com/english/products/profile-system.
80. WEB-KLUB.CZ. *RPPK-115UH/230 - Pásová pila na kov ROXTA*. Online. AzVercajk.cz. Dostupné z: https://www.azvercajk.cz/rppk-115uh-230-pasova-pila-na-kov-roxta/d38373. [cit. 2024-05-19].
81. FESTO. *Air solenoid valve*. Online. Festo CA. Dostupné z: https://www.festo.com/ca/en/p/solenoid-valve-metric-id_VZWM/. [cit. 2024-05-19].
82. GM ELECTRONIC. *SELEC 600XU multifunkční časové relé*. Online. Elektronické součástky, komponenty - null. Dostupné z: https://www.gme.cz/v/1483782/selec-600xu-multifunkcni-casove-rele. [cit. 2024-05-19].
83. CZECHPROJECT SPOL. S R.O. *Senzor překážek*. Online. Dratek.cz. Dostupné z: https://dratek.cz/arduino/901-senzor-prekazek.html. [cit. 2024-05-19].
84. ROHRBACH, Z J; BURESH, T R a MADSEN, M J. The exit velocity of a compressed air cannon. Online. *ArXiv.org*. 2011. Dostupné z: https://doi.org/10.48550/arxiv.1106.2803. [cit. 2024-05-19].
85. DENNY, Mark. The Internal Ballistics of an Air Gun. Online. *The Physics Teacher*. 2011, roč. 49, č. 2, s. 81-83. ISSN 0031-921X. Dostupné z: https://doi.org/10.1119/1.3543577. [cit. 2024-05-19].
86. JOPEK, Miroslav; RIDKY, Radek; KRAL, Pavel; PIPISKA, Tomas; RAHEL, Jozef et al. Determining the dynamic properties of spruce wood using the Taylor anvil test. Online. *BioResources*. 2024, roč. 19, č. 2, s. 3725-3739. ISSN 19302126. Dostupné z: https://doi.org/10.15376/biores.19.2.3725-3739. [cit. 2024-05-19].
87. EHRHART, Thomas; STEIGER, René a FRANGI, Andrea. A non-contact method for the determination of fibre direction of European beech wood (Fagus sylvatica L.). Online. *European Journal of Wood and Wood Products*. 2018, roč. 76, č. 3, s. 925-935. ISSN 0018-3768. Dostupné z: https://doi.org/10.1007/s00107-017-1279-3.

LIST OF SYMBOLS AND ABBREVIATIONS

Symbols

Mark	Legend	Unit
B	Work hardening coefficient	MPa
b	Burgers vector size	a
C	Strain rate sensitivity coefficient	-
C_1	Relation of thermal and deformation rate effect constant	MPa
C_2	Constant related to grain size	MPa
C_3, C_4	Thermal activation effect constants	K^{-1}
C_5	Preexponential factor	MPa
d	Average grain diameter	mm
E	Modulus of elasticity	$N \cdot mm^{-2}$
F	Applied load	N
G_0	Height of the free energy barrier	$kJ \cdot mol^{-1}$
H(T)	Reducer function	-
I	Geometric moment of inertia of the profile	cm^4
K	Strength coefficient	-
k	Microstructural stress intensity	$MPa \cdot mm^{1/2}$
L	Length	mm
L_f	Overall length of a specimen after a test	mm
M	Schmidt factor	-
m	Thermal softening coefficient	-
n	Strain hardening coefficient	-
S	Dislocation activation area	b^2
T	Absolute temperature	K
T*	Homologous temperature constant	-
T_c	Temperature of critical phenomenon	K
T_m	Melting absolute temperature	K
T_0	Room absolute temperature	K
u(T)	Step function of temperature	-
v	Impact velocity	$m \cdot s^{-1}$
X	Length of undeformed portion	mm
β	Deformation and strain-rate dependent parameter	-
ε	Engineering strain	%
ρ	Density of material	$kg \cdot m^{-3}$
σ_y	Yield stress	MPa
σ_{dy}	Dynamic yield stress	MPa
σ_{def}	Flow stress prior to recrystallization	MPa
σ_{rec}	Flow stress after recrystallization	MPa
σ_0	Static yield strength	MPa
σ_p	True stress	MPa
φ	Strain	-
$\dot{\varphi}$	Strain rate	s^{-1}
$\dot{\varphi}_0$	Reference strain rate	s^{-1}

Abbreviations

Mark	Legend
BCC	Body Centered Cubic
FCC	Face Centered Cubic
PDV	Photon Doppler Velocimetry
SHPB	Split Hopkinson Pressure Bar
TAT	Taylor Anvil Test

LIST OF ATTACHMENTS

Attachment 1	List of sample dimensions and weights
Attachment 2	Graph of speed to filling time dependency

LIST OF DRAWINGS

Symmetric Taylor Anvil Canon	208561 – 01 / 03
Main Profile Assembly	208561 – 02 / 03
Support Frame Assembly	208561 – 03 / 03

Attachment 1

List of sample dimensions and weights

Sample pair 1	
Fire pressure = 3,5 bar	
A1	B1
L = 20,0 mm	L = 20,1 mm
Ø D = 9,6 mm	Ø D = 9,6 mm
m = 7 g	m = 7 g

Sample pair 2	
Fire pressure = 4 bar	
A2	B2
L = 20,2 mm	L = 20,3 mm
Ø D = 9,5 mm	Ø D = 9,5 mm
m = 7 g	m = 7 g

Sample pair 3	
Fire pressure = 4,5 bar	
A3	B3
L = 20,3 mm	L = 20,2 mm
Ø D = 9,9 mm	Ø D = 9,9 mm
m = 6 g	m = 6 g

Sample pair 4	
Fire pressure = 5 bar	
A4	B4
L = 20,2 mm	L = 20,2 mm
Ø D = 9,0 mm	Ø D = 9,0 mm
m = 6 g	m = 6 g

Sample pair 5	
Fire pressure = 5,5 bar	
A5	B5
L = 20,0 mm	L = 20,1 mm
Ø D = 9,1 mm	Ø D = 9,1 mm
m = 6 g	m = 6 g

Sample pair 6	
Fire pressure = 6 bar	
A6	B6
L = 20,0 mm	L = 20,1 mm
Ø D = 9,0 mm	Ø D = 9,0 mm
m = 6 g	m = 6 g

Sample pair 7	
Fire pressure = 3 bar	
A7	B7
L = 20,1 mm	L = 20,0 mm
Ø D = 9,4 mm	Ø D = 9,4 mm
m = 6 g	m = 6 g

Attachment 2

Graph of speed to filling time dependency